DETERMINING THE PARAMETERS OF CYLINDERS USING DIGITAL PHOTOGRAMMETRY FOR APPLICATION TO PIPE MEASUREMENT IN INDUSTRIAL PLANTS

Submitted to the University of Cape Town in fulfilment of the requirements for the Degree of Doctor of Philosophy

by

Malcolm Robert Dingle

Department of Geomatics

February 1998

This thesis is dedicated to

my mother for providing my foundations

Emma for growing with me

Ulrike for giving me the strength to try

Claudia for giving me the strength to succeed

ABSTRACT

The maintenance and expansion of piping systems of petro-chemical plants is a complex and costly process. These costs can be reduced by knowledge of the as-built dimensions and layout of the piping system. As-built Computer Aided Design (CAD) models of such piping systems, specifically the use of Plant Design System (PDS) software packages, allow for more efficient planning than paper plans. Conventional surveying and analogue photogrammetry have been methods that have traditionally been used to capture the necessary CAD information. More recently, the Department of Geomatics at the University of Cape Town has produced software which replicates the analogue photogrammetric approach using digital images (Cammidge, 1996).

The objective of this thesis is to develop a pipe measurement technique which can supplement those currently being used and overcome some of their shortcomings. A further objective is to present an overview of the pipe measurement techniques, photogrammetric principles, image processing techniques and programming considerations which would be required to develop a robust, fully functional, pipe measurement software package integrated with a PDS. The author hopes that this thesis will form the foundation for the development of such a software package for local and possibly international industry.

A digital photogrammetric technique related to line photogrammetry is developed. This technique makes use of lines in an image which represent the silhouette edges of the cylinder. The use of photogrammetry based on lines avoids some of the shortcomings of conventional point-based photogrammetry. It is not necessary to identify conjugate points in images, nor is it even necessary for overlapping images of the cylinder to be captured.

Furthermore, this thesis reports on a number of tests designed to gauge the developed techniques' accuracy and suitability for use in pipe metrology in an industrial plant.

The techniques were found to be capable of achieving results which deviated by, on average, 2-3mm in object position and 0.1° in direction from the likely true values of the cylinder axis. The radius could be determined to better than 1mm.

The techniques developed here proved to be suitably accurate for the purpose of determining the parameters of pipes in industrial plants. However, certain factors may reduce the accuracy and these are also discussed.

This thesis concludes that a novel digital photogrammetric technique for measuring pipes in an industrial plant was successfully developed. Recommendations are made as to how the technique might be improved to allow sub-millimetre accuracies to be obtained. Finally, a recommendation is made that the information contained within the thesis be used as the basis for designing a digital photogrammetric measurement module to be linked to a PDS.

ACKNOWLEDGEMENTS

I would like to thank my supervisor Professor Heinz Rüther for making it possible for me to undertake this research and for his advice and guidance throughout the duration of my studies.

I would also like to extend my thanks and appreciation to the staff of the Department of Geomatics, in particular Val Atkinson, Sue Binedell, Michael Haywood, Kari Laatikainen, Dr. Scott Mason and Sidney Smith who have assisted me in numerous ways with this project.

Many thanks to Mike Calitz, Mark Cammidge, Dirk Craigie, Simon Crone, Nathan Geffen, Justin Hill, Eric Kwabena-Forkuo, Nick van der Merwe, Siddique Motala, Julian Smit and as well as the other postgraduate students within the department with whom I have been fortunate enough to work with over the years. A special acknowledgement is due to Ulrike Brüssler, Pierre Hoffa and Henty Waker for the many hours of discussion, both work related and otherwise.

A special mention of appreciation is due to my mother for her belief that education opens doors and who selflessly supported my tertiary education to the fullest extent of her abilities. I would also like to thank my sister for her encouragement over the years.

Finally, I would like to acknowledge the financial support of the Foundation for Research Development (FRD) which made this project possible.

TABLE OF CONTENTS

LIST OF FIGURES

LIST OF TABLES

1 INTRODUCTION

In recent years the design and maintenance of industrial parts and their subsystems has moved away from paper based systems to one which is computer based and uses Computer Aided Design (CAD) packages. This has had the advantage of offering the potential to translate two dimensional plans into three dimensional graphic representations of the object being designed. It is now possible to plan and design an object not only as a set of two dimensional plans, but rather also as a three dimensional model. Designers are able to produce an initial design more rapidly than was previously possible and to better comprehend how modifications to the design will affect the final manufactured object as well as its interaction with other industrial parts.

Although many new industrial objects are being designed with the use of CAD, the information describing already existing objects is often still stored in the form of two dimensional paper plans. It is often desirable to describe these objects using a CAD model in order to take advantage of the benefits CAD offers. Reverse engineering, the process of measuring an object in order to produce a such a model, is currently a field of research of international interest.

Current metrology techniques which can be used to gather data for reverse engineering include the use of very accurate surface contact measurement machines. However, these machines are expensive and limited to measuring relatively small sized objects. In order to measure large objects, techniques making use of laser profiling machines or conventional surveying methods, which utilise angle and distance measurement observations, are often applied. Both these techniques have benefits, but also drawbacks, thereby limiting their practicality in certain situations.

Conventional analogue photogrammetry is another technique that has frequently been used to measure large objects (Ryan 1982 and Szczechowski, 1980). It offers the advantage of accurate measurement as well as providing an permanent record of the object, a benefit which few other techniques are capable of providing. A further advantage of photogrammetry, is that unlike some other techniques, most of the measurements and calculations can be performed off-site. This ensures that the "downtime" of the object, if required at all, is kept to a minimum.

Digital photogrammetry offers advantages over conventional analogue photogrammetry. The data is stored in a digital format which presents the possibility of automating a large part of the measurement process. It also provides a more stable format for archiving the original images and allows fully identical copies of the images to be made for redistribution purposes. In many situations, these features make digital photogrammetry an ideal tool for the reverse engineering of large objects.

All industrial plants can effectively be considered to consist of a network of interconnected pipes and related objects. Petro-chemical plant designers are aware of the advantages of three dimensional CAD modelling and have utilised three dimensional plant design systems (PDS) for some time. New plants and areas of existing plants which are being expanded are "designed" in three dimensions within the CAD system. However, construction knowledge relating to existing plants is often limited to the original design drawings stored in a two dimensional form on paper. These design drawing are often outdated not only because the plant may not have been built exactly according to specification, but also as a result of subsequent modifications to the plant.

The refurbishment of an existing petro-chemical plant represents a major undertaking for a company in terms of time and money. This generally entails installing additional pipes or replacing the existing pipes with new and possibly larger pipes. The cost of new pipes, as well as the loss of revenue due to plant downtime, means that the process of fitting the new pipes must be optimised as much as possible. Since the

design of the new pipes is often based on the original (paper) design plans, some deviation of the actual design from the original design specifications may exist. It is therefore likely that without correct current three dimensional information, additional on-site modifications to the new pipes will need to be made, thus increasing the installation cost.

A more cost-effective approach is that of using an as-built CAD model. This would allow for a more precise determination of the specifications and location in space of the pipes to be replaced and connected before on-site fitment is attempted. A further advantage of using a CAD model is that problem areas and potentially better solutions can be more easily identified with three dimensional visualisation than with two dimensional plans.

At present the photogrammetric and survey techniques utilised by local industry to produce as-built CAD models are relatively unsophisticated. Until recently such methods utilised conventional photogrammetric techniques. This involved the digitisation on analogue photographs of well defined individual points on the surface of pipes. More recently, the department of Geomatics (UCT) has replicated this process using digital imagery (Cammidge, 1996). As a result, the measurement of individual points can now be carried out entirely on a personal computer. However, this is still a relatively simplistic solution to the problem and does not fully exploit the capabilities of digital photogrammetry. There is a great deal of scope for more automated and flexible approaches which are not as reliant on manual identification of well defined individual points.

The primary objective of this thesis is to develop a pipe measurement technique which can supplement those currently being used and overcome some of their shortcomings. A further objective is to present an overview of the pipe measurement techniques, photogrammetric principles, image processing techniques and programming considerations which would be required to develop a robust, fully functional, plant measurement software package integrated with a PDS. The author hopes that this

thesis will form the foundation for the development of such a software package for the local industry.

1.1 Thesis Outline and Overview

This thesis is divided into a further eight chapters (excluding the appendices):

Chapter 2 provides a brief review of some literature covering areas relevant to this research.

Chapter 3 describes some of the basic theory of photogrammetry relevant to this research. It is especially targeted towards readers whose expertise lie outside the area of photogrammetry.

Chapter 4 describes some of the current point-based photogrammetric methods for determining cylinder parameters. The strengths and weaknesses of the methods are discussed. The concept of line photogrammetry, which differs fundamentally from point-based photogrammetry, is then introduced.

Chapter 5 presents a novel photogrammetric method, evolved from line photogrammetry, for determining the parameters of a cylinder. The technique is explained and variations of the method are presented.

Chapter 6 deals with the various edge detection and line extraction algorithms which were examined or developed in order to implement the concept described in Chapter 5.

Chapter 7 reports on a number of tests used to determine the accuracy of the methods developed in Chapter 5 and the consequent suitability of the methods for measuring pipes in industrial plants.

Chapter 8 describes an attempt at analysing the propagation of errors through one of the methods presented in Chapter 5.

Chapter 9 draws some conclusions regarding the suitability of the techniques developed for pipe measurement and makes some recommendations regarding the development of a pipe measurement software package.

The appendices describe additional information relevant to this thesis which were unsuitable for inclusion in the main body of the thesis. In particular, one section deals with some aspects of the research related to software programming as well as computer hardware. Other sections present additional tables of test results and a table of directional search matrices relating to line following.

2 LITERATURE REVIEW

Photogrammetry first gained wide acceptance as a means of producing maps using aerial imagery. Stereo images are oriented by mechanical means in large stereo plotters. The mechanical orientation of the images in the plotter effectively reproduces the relative position of the images at the instant of capture. This allows the operator to stereoscopically view a three dimensional model of the features in a stereo-pair of images. By means of placing a "floating mark" onto a point on the surface of the three dimensional model, the parallax between the two images at that point can be determined. This parallax reading allows the three dimensional co-ordinate of the point to be determined.

Great advances have been made since photogrammetry was first recognised as an effective mapping technique. These advances were made possible by continuous improvements in photogrammetric and related algorithms and especially by rapid increases in technology. These developments in photogrammetry led to the emergence of analytical photogrammetry.

Analytical photogrammetry is characterised by the replacement of previously mechanical tasks, such as relative and absolute orientation, with computational techniques, whilst still utilising conventional analogue images. Two influential algorithms which were developed during this time were that of the bundle adjustment (Brown, 1958) and the direct linear transformation (DLT) (Abdel-Aziz and Karara, 1971). Both of these techniques relate the object co-ordinates of points to the image co-ordinates of their projection onto an image. They may be used to determine the exterior orientation of captured images, the interior orientation the cameras used and the object co-ordinates of points of interest. Analytical photogrammetry not only increased the efficiency of stereo-based photogrammetry, but it also made possible the use of multi-station, close-range photogrammetry utilising convergent images.

More recently, advances in computer technology and numerical algorithms has made digital photogrammetry possible. Digital images may be produced from a number of sources including CCD video cameras, by scanning analogue images, and more recently through the use of still digital camera such as the Kodak DCS420 (Fraser and Shortis, 1994). Not only has the technology improved dramatically, but a great deal of research has been directed towards automating the measurement process. Further work in the area of such fundamental tools as the DLT (Dermanis, 1994) and the bundle adjustment (Hâdem, 1990) has been made to increase the flexibility of these tools. Techniques of automatically detecting control points in digital images have been investigated by, amongst others, Rubenstein (1990) and Fraser (1997).

A field that has received particular attention is that of industrial digital photogrammetry. Digital photogrammetry offers great benefits over alternative measurement systems in terms of cost efficiency, high accuracy and in the rapid rate at which results can be produced. Numerous examples exist of successful industrial applications of digital photogrammetry. Beyer (1991) successfully implemented a system measuring the deformation of car bodies in crash tests. Fraser and Shortis (1995) described the measurement of an assembly jig of an aircraft. Bruhn and Schneider (1990) as well as Smit *et al* (1997b) have studied the surfaces of automobiles for aerodynamic analysis.

An area of industrial measurement in which photogrammetry has enabled greater efficiency is that of mapping the piping layout of industrial plants. An early commercial analytical system was that of ICI's "Photometrology" package (MCP, 1986). The system used UMK metric cameras to produce analogue images. Control points were provided for the orientation of the images by targets placed in the scene prior to image capture. The object co-ordinates of the targets were determined by conventional surveying methods. The film negatives were placed into a stereo comparator and both the image co-ordinates of the control points as well as those of other points of interest were measured. Finally, these observations were input into dedicated software and three dimensional information calculated. Each type of feature (i.e. cylinder or nozzle) required that the operator measure a specific number of points

in specific positions on the feature. In the case of a cylinder, eight or more surface points on the cylinder, identifiable in at least two images, were measured.

The approach of determining cylinder parameters, based on a number of random surface points, was described and investigated by Chandler and Cooper (1991). They described a method using analytical photogrammetry by which they successfully measured a curved ceiling of a ballroom.

Krämer and Schöler (1980) made use of conventional analogue photogrammetry to determine the orientation and radius of pipes using various techniques. The techniques described require that the position of a number of points on the surface of the cylinder be known. One of these methods requires that these points lie on a visibly defined circumference line. Another of the techniques results in only the approximate position of the pipe being determined whilst the radius cannot be calculated at all.

The methods described by Krämer and Schöler, as well as that described by Chandler and Cooper, have a shortcoming in that they rely on identifying surface points which are clearly visible in at least two images. It is necessary to measure the image co-ordinates of each of these surface points in at least two images in order to determine their object co-ordinates by means of intersection calculations. It is often difficult to find points which are both suitable for the techniques as well as clearly visible in two or more images. Any cylinder parameter determination technique which requires that object co-ordinates of points on the cylinder's surface be first determined, will suffer from this shortcoming.

Further work has been carried out using analytical photogrammetry to produce spatial models which can be displayed in CAD packages. Littleworth, Stirling and Chandler (1992) described the successful use of analytical photogrammetry interfaced with a CAD system to create three dimensional computer models of various environments. Specifically, the models of industrial environments which they developed were of a

gantry crane in a power station and the layout of pipes and other vessels in a chemical plant. For both projects as well as others which they refer to, a UMK metric camera was used to capture the images.

Littleworth and Chandler (1995) again describe their use of analytical photogrammetry linked to a CAD system. Once again, analogue UMK images were used. They discuss a project which was undertaken to produce an "as built" CAD model of an oil refinery in Scotland. The purpose of the model was to assist in the planning process of the refurbishment of the refinery. In particular they discuss some of the problems encountered in capturing the required 56 images. The method used to determine the orientation and radii of the pipes was the same surface fitting approach described by Chandler *et al* in the earlier 1991 paper. The resultant information about the pipes was imported into an Intergraph PDS, a CAD program specifically developed to assist in the design, layout and mapping of industrial plants.

Whilst much success is being achieved using analytical photogrammetry assisted by CAD packages, progress has also been made in the use of digital photogrammetry for the mapping of industrial plants. Chapman, Deacon and Hamid (1992) describe the role digital photogrammetry plays in a system (HAZMAP) designed to generate CAD models in hazardous environments, specifically in a nuclear power plant. They describe the difficult conditions under which the system is expected to operate and highlight some of the limitations this imposed on their choice of hardware. A purpose-built robotic imaging system was used to capture the digital images. The HAZMAP system relies on the tight integration of the photogrammetric module with a PDS developed by CADcentre Cambridge. This PDS is a highly sophisticated package which includes models of numerous features likely to be found in a nuclear power plant . An advantage of using the PDS is that, since it also models the functionality of items, minor adjustments can automatically be made to the position of items determined by the photogrammetric module in order to ensure that a realistic working model of the plant can be developed. Furthermore, by linking the PDS to the photogrammetric system, facilities exist for "injecting" geometric primitives into images, thereby allowing for the manual determination of best fitting objects by the

operator. The photogrammetry system defines the position of pipes by means of two points on the central axis of the pipe. These central points are calculated by measuring points on clearly defined visible circumference lines.

Other digital photogrammetric systems which have been developed to measure features in industrial plants include a commercial system described by Hamit (1995) which utilises scanned images. The images were scanned at resolutions of between 3400 and 6000 dpi. This high resolution overcomes the limitations imposed by using digital cameras which typically have a lower resolution. The system relies on an Intergraph PDS in which newly calculated features as well as pre-existing information is stored.

Another system, with less features than those described by Hamit or Chapman *et al*, was developed by Cammidge (1996). This system determines the orientation and radius of a pipe by measuring points on a well defined visible circumference line of the pipe. The defining parameters of the pipe can then be input into a CAD system of the users choice.

Little mention could be found of methods for determining the parameters of a cylinder which do not require that the object co-ordinates of points on the cylinder surface be calculated. This may be because object point based techniques suffice in most situations. However, development of techniques capable of determining cylinder parameters by other methods would clearly be valuable, since at times it is simply not possible to find suitable points on the surface of the cylinder.

As a consequence of the search for a cylinder parameter determination technique which is not based on object points, line photogrammetry was investigated. Line photogrammetry differs from point-based photogrammetry in that lines in object space and their depiction in an image, rather than discrete points in object and image space, form the basis of the measurement process. Mulawa and Mikhail (1988)

developed a theory directly relating image and object features by way of the coplanarity condition. They went on to develop the theory so that it could be used for general features such as circles and splines. Petsa and Patias (1994b) present both the basic equations of line photogrammetry as well as other equations which can be used for relative orientation, space intersection and absolute orientation. Zielinski (1993) describes the fundamentals of line photogrammetry and refers to earlier work in this field. He investigates the effect of applying geometric constraints to line photogrammetric adjustment algorithms, using both single, as well as combinations of three dimensional lines. In order to test these geometrically constrained algorithms he measured two buildings using both analogue and scanned aerial images. Zielinski concluded that line photogrammetry is capable of achieving similar or higher accuracies than those achievable using stereo photogrammetry.

Edge detection within an image is often a prerequisite of line extraction. Numerous papers have been written on methods of edge detection including those by Canny (1986), Matthews (1994) and Heipke *et al* (1994) who all describe methods of determining the location of edges to single pixel accuracy. Tabatabai and Mitchell (1984) describe a method of determining an edge location to sub-pixel accuracy.

Many methods of extracting lines and curves from an image, once edge detection has been performed, are mentioned in the literature. Ballard (1981) describes the Hough Transform which may be used to extract straight lines from an image. Van der Merwe (1995) describes a method of tracking around the boundary of a feature. Haralick and Shapiro (1986) also describe methods of connecting points on an image to form the boundary of a feature. Heipke *et al* (1994) describes a technique of tracking the edges of a road on an aerial image.

This thesis draws on some of the findings and experiences reported in the literature discussed above in order to develop a technique which can be used to determine the parameters of a cylinder without need to calculate the object co-ordinates of points on its surface.

3 INTRODUCTION TO PHOTOGRAMMETRY FOR NON-PHOTOGRAMMETRISTS

The purpose of this chapter is to present an overview of some of the digital photogrammetric concepts upon which later chapters in this thesis depend. The information provided here may be known to digital photogrammetrists, however, it is included for the benefit of non-photogrammetrists who may wish to implement the algorithms presented later in Chapters 4, 5 and 6.

3.1 Defining The Relationship Between Image and Object Space: The Collinearity Equations

The fundamental concept upon which photogrammetry is based is the ability to define a relationship between the co-ordinates of features in three dimensional object space and the two dimensional image co-ordinates of the projection of those points onto an imaging medium.

Figure 1 shows the geometrical relationship between the two dimensional image co-ordinate system (image space) and the three dimensional object co-ordinate system (object space).

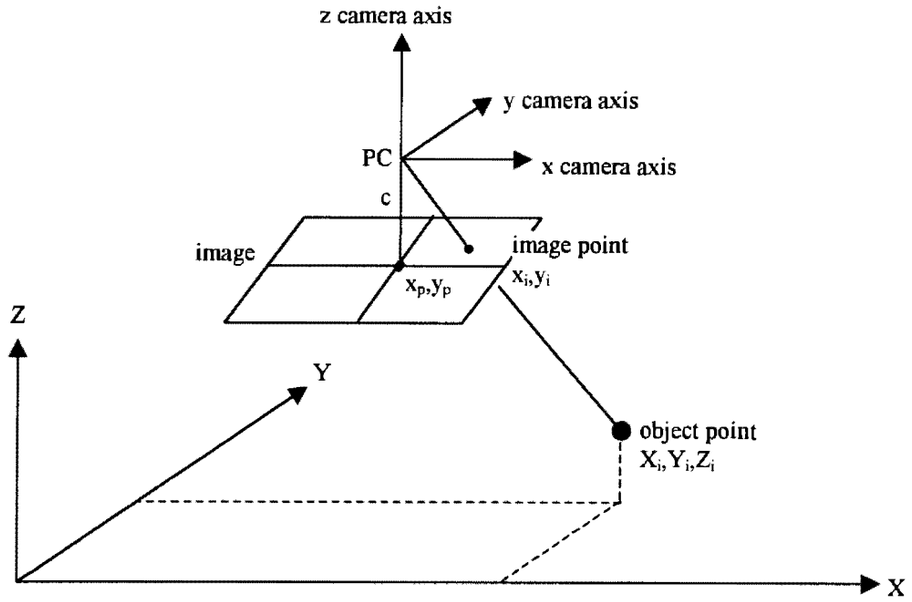

Figure 1 The projection of an object point onto an image

The centre of the camera lens, termed the perspective centre (*PC*), has the object space co-ordinates (X_C, Y_C, Z_C). It is through this point that the light ray from the object point (X_i, Y_i, Z_i) passes in order to be projected onto the image. In order to simplify the understanding of the relationship between the image and object co-ordinate systems, the image in Figure 1 is shown as a positive image in front of the PC. However, the lens and therefore the PC, naturally lie between the object and the imaging medium when the image is originally captured. It is only for the sake of mathematical convenience that the relationship between the PC, the image plane and object space are arranged in the manner shown in Figure 1. The image co-ordinate system has its origin at the principal point (x_p,y_p). The principal point can be defined as the point on the image at which a ray orthogonal to the image plane and passing through the PC intersects the image plane. In practice this point will not be in the exact physical centre (0,0) of the image. As a result, (x_p,y_p) typically has small non-zero values. The distance between the PC and the principal point is termed the principal distance (c).

Mathematically the relationship between the PC, image points and object points, can be expressed by the collinearity equations (Equation 1 and Equation 2) which transform the co-ordinates of a point in object space to co-ordinates in image space.

$$x_i - x_p + dx_i = c\frac{m_{11}(X_i - X_C) + m_{12}(Y_i - Y_C) + m_{13}(Z_i - Z_C)}{m_{31}(X_i - X_C) + m_{32}(Y_i - Y_C) + m_{33}(Z_i - Z_C)}$$

Equation 1

$$y_i - y_p + dy_i = c\frac{m_{21}(X_i - X_C) + m_{22}(Y_i - Y_C) + m_{23}(Z_i - Z_C)}{m_{31}(X_i - X_C) + m_{32}(Y_i - Y_C) + m_{33}(Z_i - Z_C)}$$

Equation 2

in which

$$\begin{aligned}
m_{11} &= \cos\phi\cos\kappa \\
m_{21} &= \cos\omega\sin\kappa + \sin\omega\sin\phi\cos\kappa \\
m_{31} &= \sin\omega\sin\kappa - \cos\omega\sin\phi\cos\kappa \\
m_{12} &= -\cos\phi\sin\kappa \\
m_{22} &= \cos\omega\cos\kappa - \sin\omega\sin\phi\sin\kappa \\
m_{32} &= \sin\omega\cos\kappa + \cos\omega\sin\phi\sin\kappa \\
m_{13} &= \sin\phi \\
m_{23} &= -\sin\omega\cos\phi \\
m_{33} &= \cos\omega\cos\phi
\end{aligned}$$

Equation 3

where:

x_i, y_i	are the image co-ordinates of the projected point
x_p, y_p	are the co-ordinates of the principal point
dx_i, dy_i	are distortion corrections applied to the x and y image co-ordinates of the image point
c	is the principal distance

X_C, Y_C, Z_C are the co-ordinates of the perspective centre

X_i, Y_i, Z_i are the object co-ordinates of the point to be projected

m_{ij} are elements of a 3x3 dimensional orthogonal rotation matrix

ω, ϕ, κ are rotations about the x,y,z camera axis respectively and are positive in the counter clockwise direction. The camera axes are fixed in a right handed co-ordinate system.

The elements (m_{ij}) of the final rotation matrix used in the equations above are formed by a sequence of three individual rotations (ω, κ, ϕ), each one about a separate axis of the camera (x,y,z). Each individual rotation produces a single rotation matrix; $R_x(\omega)$, $R_y(\phi)$ or $R_z(\kappa)$ about the x, y, or z axes respectively. The final rotation matrix is the product, in the sequence that the rotations were applied, of all three individual rotation matrices (i.e. $R_{(\omega,\phi,\kappa)}=R_z(\kappa)R_y(\phi)R_x(\omega)$). Any of the six permutations of rotations about the co-ordinate system axis may be used (i.e. $R_zR_yR_x$, $R_zR_xR_y$ etc) provided the same rotation sequence is consistently used for all future calculations. Different sequences of rotations will result in final rotation matrices with different values of their individual elements. However, the effect of applying the full rotation matrices to a co-ordinate will be unchanged.

The elements of the final rotation matrix shown in Equation 3 were formed by rotating about first the x, secondly the y and finally the z-axis of the camera. Mathematically this is indicated by $R_{(\omega,\phi,\kappa)}=R_z(\kappa)R_y(\phi)R_x(\omega)$.

Manufacturing inaccuracies result in the lens deviating from its intended design. As a result, light is not always projected through the lens from a point in object space to a point in image space in the intended manner. This results in imperfect collinearity between the PC, the image point and the object point. The distortion corrections (dx_i and dy_i) which are applied to each image co-ordinate in the equations above, are intended to compensate for the imperfections of the measurement system. Principle among these are the effects of radial and decentring lens distortion.

3.1.1 Radial and Decentring Lens Distortions

Radial lens distortion is a phenomena apparent in all lenses. While radial distortion may be slightly asymmetric it is conventionally shown as being symmetric about a "principal point of best symmetry" which does not necessarily coincide with the principal point. This point is the intersection of the optical axis of the lens with the sensor surface (van der Vlugt, 1995). In most models used in photogrammetry the principal point and the "principal point of best symmetry" are assumed to be identical. Distortions may be either positive or negative. Figure 2 shows the effect both positive and negative symmetrical radial lens distortion have on straight lines projected into different regions of an image.

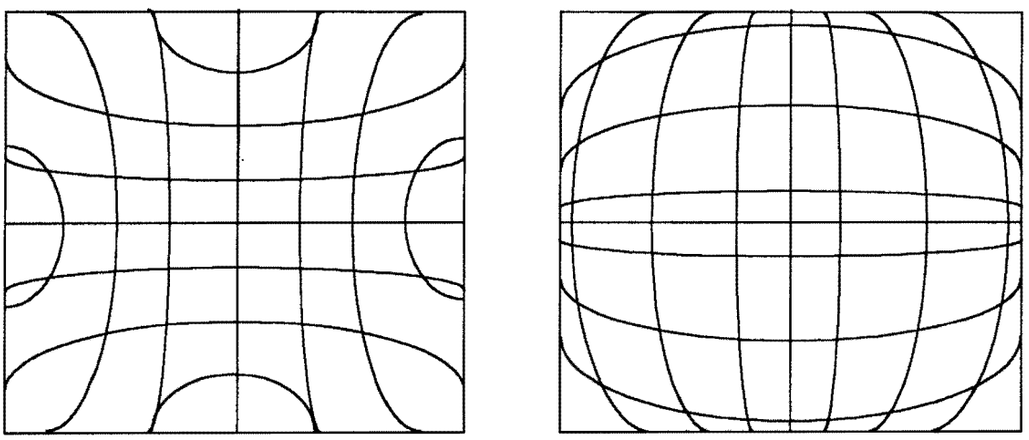

Positive radial distortion **Negative radial distortion**

Figure 2 The effects of radial distortion on lines projected onto an image

The effect of radial lens distortion may be approximated by Brown's model (van der Vlugt, 1995) using the following equations:

$$dx_r = \bar{x}(k_1 r^2 + k_2 r^4 + k_3 r^6)$$
$$dy_r = \bar{y}(k_1 r^2 + k_2 r^4 + k_3 r^6)$$

Equation 4

where:

k_1,k_2,k_3 are the symmetrical radial lens distortion parameters

and

$$\bar{x} = x_i - x_p$$
$$\bar{y} = y_i - y_p$$
$$r^2 = \bar{x}^2 - \bar{y}^2$$

Equation 5

In an ideal lens system the centres of curvature of all the spherical surfaces are collinear with the optical axis (van der Vlugt, 1995). However, in reality misalignment of the lens components causes distortion known as lens decentring distortion. This distortion has both a tangential and a radial component. The combined effect of these components can be determined from the following equations (Brown, 1958).

$$dx_d = P_1(r^2 + 2\bar{x}^2) + 2P_2\bar{x}\bar{y}$$
$$dy_d = 2P_1\bar{x}\bar{y} + P_2(r^2 + 2\bar{y}^2)$$

Equation 6

where:

P_1,P_2 are the lens decentring distortion parameters

and where the other terms are as indicated in Equation 5

Smit (1997a) states that although it is not obvious from Equation 6, P_1 and P_2 exhibit a high degree of projective correlation with the principal point. As a result the effect of decentring distortion may to a large extent be accommodated in the calculated value of the principal point. As a result, calibration may imply that a lens is free from decentring distortion.

Additional distortions may also occur in the measurement system. These distortions are less common in modern digital cameras than they were in both earlier models of digital and analogue cameras. Van der Vlugt recommends applying a scale factor correction (S_x) along the x-axis of the image and a shear factor (a) for deviations in the pixel array from rectangularity. These can be determined from Equation 7 in which once again the elements are as given in Equation 5.

$$dx_f = \bar{x}S_x + \bar{y}a$$
$$dy_f = \bar{x}a$$

Equation 7

The full distortion model used in this thesis defining dx and dy_i as used in Equation 1 and Equation 2 is given by:

$$dx_i = \bar{x}(k_1r^2 + k_2r^4 + k_3r^6) + P_1(r^2 + 2\bar{x}^2) + 2P_2\bar{x}\bar{y} + \bar{x}S_x + \bar{y}a$$
$$dy_i = \bar{y}(k_1r^2 + k_2r^4 + k_3r^6) + 2P_1\bar{x}\bar{y} + P_2(r^2 + 2\bar{y}^2) + \bar{x}a$$

Equation 8

x_p, y_p, c, dx_i and dy_i presented in the collinearity equations (Equation 1 and Equation 2) represent the interior orientation of the camera. Provided the principal distance of the camera is not subsequently altered by changing the focal length setting and the

camera is not subjected to external forces, the interior orientation of a camera will remain constant between successive images. The parameters X_C, Y_C, Z_C, ω, ϕ and κ, as used in the collinearity equations, represent the exterior orientation of an individual image. As a results of moving the camera, the exterior orientation differs for every camera position.

3.2 Recovering Interior and Exterior Orientation

In order to perform photogrammetric calculations such as those described later in this thesis, both the interior orientation of the camera, as well as the exterior orientation for each image, needs to be known.

The process of calculating the interior and exterior orientation throughout this thesis was accomplished in either of the two ways described below as well as indicated in Figure 3:

1. A highly accurate determination of the interior orientation parameters of the camera can be found using one set of images of a control frame. A second set of images, this time of the object to be measured, can then be captured and the predetermined interior orientation parameters used to determine the exterior orientation of these images.
2. Both the camera interior orientation and the exterior orientation of images of the object to be measured can be calculated in a single step using only one set of images. However, this may result in orientations of slightly lower accuracy.

Only one of the two processes described above are required. The details of these processes are described more fully in the text following the chart.

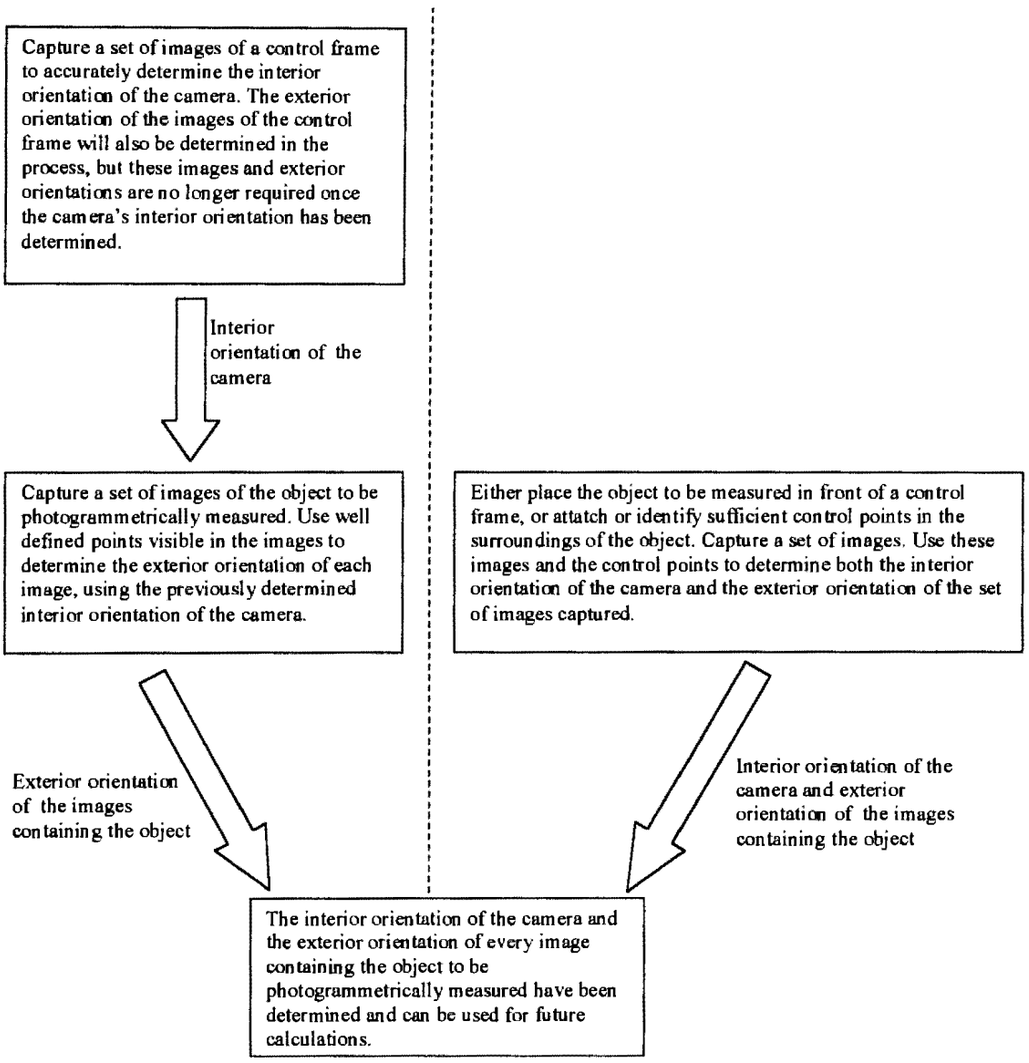

Figure 3 Chart showing two approaches to determining the necessary interior and exterior orientation parameters

If the procedure on the left hand side of Figure 3 is followed, the interior orientation can be determined using a set of images captured solely for this purpose. The process of determining the interior orientation of a camera is known as camera calibration. The camera calibration process consists of photographing a number of features, typically clearly defined points, whose object co-ordinates are known. Image co-ordinates of these features can then be measured. Using the relationship between image and object space co-ordinates as expressed in the collinearity equations, the interior orientation parameters can be determined.

In order to determine the interior orientation of a camera, the exterior orientation of each image used for camera calibration needs to be either predetermined or solved for simultaneously with the interior orientation. Either of two well known techniques may be used to determine both interior and exterior orientation. Both the direct linear transformation (DLT) and the bundle adjustment combine the determination of the interior and exterior orientation relating to an image, or a number of images, into one process. The DLT and the bundle adjustment are explained in some detail later in this chapter.

As was previously mentioned, images of a number of well defined features whose object co-ordinates are known must be captured and can be used for both interior as well as exterior orientation determination. The centre points of circular retro-reflective targets are such convenient features and were used for this thesis. These targets can be attached to the surface of an object to be measured or to a control frame.

For the purpose of determining the interior orientation of a camera to as great a degree of accuracy as possible, a control frame can be used (Figure 4). Such a control frame allows a large number of targets (90 in the case of that shown in Figure 4) at varying depths, to be viewed from a variety of camera positions.

Figure 4 Example of a control frame

To determine the interior orientation with the highest degree of reliability and accuracy, the relative positions of the targets may be determined using one of a variety of conventional surveying techniques before camera calibration is performed. The reader should note however, that it is well documented in photogrammetric literature that the bundle adjustment is able to determine interior orientation parameters such as lens distortions even when the initial co-ordinates of the targets have not been accurately surveyed (Atkinson, 1996 and Karara, 1989). This is only possible however, if convergent sets of images are used and if particular care is taken to ensure that the geometry of the camera positions, relative to each other and the targets, is strong. Although this use of the bundle adjustment is mentioned in the explanation of the bundle adjustment later in this chapter, it was not the approach followed in this thesis. Throughout the thesis the method of using control points which had been accurately surveyed *a priori* was used.

The large number of control points ensure that many are visible from each camera position. This provides redundant observations for the determination of the interior

orientation determination provided the object can be placed in front of the frame in such as way as to ensure that not too many targets are occluded. However, if this is impractical for any reason, it is necessary to attached control targets on or around the object to be measured. The co-ordinates of these control points may be determined using similar techniques to that which the control points of the control frame were determined. The image co-ordinates of these control points can be measured in the images. Provided the focal setting of the camera is not adjusted from the previous set of camera calibration images, a bundle adjustment can then be performed, holding the predetermined interior orientation parameters of the camera fixed, so as to determine the exterior orientation of each image of the object.

On completion of the two steps shown on the left hand side of Figure 3, the exterior orientation of every image that will later be used to measure the object, as well interior orientation of the camera, will be known.

As the right hand side of Figure 3 shows, it is possible to determine the camera interior orientation in the same step as determining the exterior orientation of the images to be used to measure the object. It was previously mentioned that both the DLT and bundle adjustment methods are capable of determining both interior and exterior orientations simultaneously. Provided the control points are sufficiently accurate and sufficient are visible, it is often more convenient to follow this approach. However, in circumstances where the number of control points are limited and/or where they do not sufficiently cover the whole image, greater accuracies are likely to be achieved by first predetermining the camera interior orientation in a two step process.

In order to calculate the interior orientation and exterior orientation using either the DLT or the bundle adjustment method, the image co-ordinates of the control points in each image need to be measured. It is possible to manually identify the approximate centre of each control point. However, if digital images are used it is simpler to apply a semi-automatic method to extract and identify target centres. Because the targets are

retro-reflective they are represented by bright, nearly white, circles or ellipses in a digital image. It is simple to threshold the image until only those pixels with a high grey level value are shown. This results in only the targets and a few other features with high grey values being displayed in the thresholded image. An example of how a target is represented in a digital image is given in Figure 6 where a grey level scale from 0 to 255 is used; 255 represents white and 0 represents black.

80	80	80	81	88	84	83	81	80	80	80
80	80	81	85	95	108	116	110	98	80	80
80	81	87	110	151	187	202	189	150	106	85
80	85	111	149	228	250	253	251	223	151	97
81	96	131	228	254	255	255	255	251	193	112
98	111	155	255	255	255	255	255	252	190	112
85	99	142	251	255	255	255	255	249	189	109
84	89	133	230	255	255	255	255	223	147	89
84	86	90	150	200	250	254	249	220	111	84
80	83	85	101	118	150	150	122	101	89	82
80	83	84	96	101	121	130	126	111	86	83
81	83	83	83	84	84	84	83	83	83	83

Figure 6 Digital representation of a retro-reflective target

The co-ordinate (x_0,y_0) of the centre of each target can then be found to sub-pixel accuracy using a weighted centre of gravity method as described by Smit (1997a) and van der Vlugt (1995) using Equation 9. It should be noted that the centre of a pixel is an integer (x,y) and that its top left corner is (x-0.5,y-0.5).

$$x_0 = \frac{\sum_{i=1}^{n}\sum_{j=1}^{m} g_{ij} x_i}{\sum_{i=1}^{n}\sum_{j=1}^{m} g_{ij}}$$

$$y_0 = \frac{\sum_{i=1}^{n}\sum_{j=1}^{m} g_{ij} y_j}{\sum_{i=1}^{n}\sum_{j=1}^{m} g_{ij}}$$

Equation 9

where:

n and m	are the row and column dimensions respectively of a window around the target in which the centre of gravity is to be determined
x_i and y_j	are the row and column position of a pixel within the window around the target
g_{ij}	is the grey level value of the pixel at (x_i,y_i)

It is still necessary to identify the targets extracted from the image and relate them to object co-ordinates of the control points. Smit (1997a) describes a process whereby the user manually names eight targets with the corresponding names of targets in a control file. This provides sufficient information to perform a DLT using the eight points. Once the approximate orientation of the image is known, an automated back projection process associates the remaining targets in the image with points in the control file.

An important difference between analytical and digital photogrammetry is the image co-ordinate system which is the conventional mathematical system in the former case, while being imposed by the electronic characteristics of the imaging chip in the latter. The co-ordinate system difference can be seen in Figure 7. Conventional photogrammetric mathematical formulations assume a metric co-ordinate system

based on an analogue image. The origin of the metric co-ordinate system is the centre of the image and image co-ordinates are commonly given in millimetres. Digital images on the other hand are comprised of pixels. The origin of a pixel co-ordinate system is the top left pixel of the image and measurements on the image are made in terms of pixels and fractions thereof.

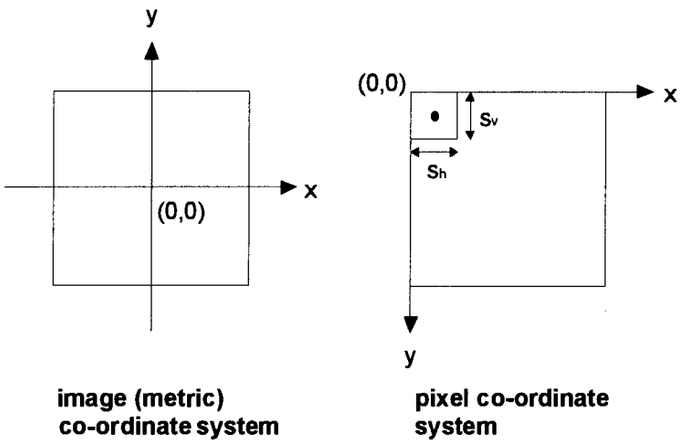

Figure 7 The image (metric) and pixel co-ordinate systems

It is necessary to transform measurements made on a digital image, in terms of pixels, to measurements in terms of metric units. Equation 10 gives the transformation from pixel to image co-ordinates.

$$x_{mm} = S_h\left(x_{pix} - \frac{h-1}{2}\right)$$

$$y_{mm} = S_v\left(\frac{v-1}{2} - y_{pix}\right)$$

Equation 10

where:

x_{mm}, y_{mm} are the image (metric) co-ordinates of the point

x_{pix}, y_{pix} are the pixel co-ordinates of the point

h	is the number of horizontal pixels in the image
v	is the number of vertical pixels in the image
S_h, S_v	are the sizes of the pixel in the horizontal and vertical directions

3.2.1 The Bundle Adjustment

As was previously mentioned, a number of image co-ordinate measurements need to be made on the images in order to determine the unknown interior and exterior orientation parameters of those images. Mathematical models are required to solve for the unknowns. The bundle adjustment is one such model.

The bundle adjustment is based on the collinearity equations given in Equation 1 and Equation 2. For every image observation, whether of a control point or of a point whose object co-ordinates are required, one set of collinearity equations can be formulated (i.e. two equations). If sufficient image observations are made, then the unknown values within the collinearity equations can be solved for in a single least squares adjustment.

The collinearity equations may be used to determine the camera orientation parameters, provided the image co-ordinates of sufficient control points are measured. Furthermore, the collinearity equations allow for the determination of the distortion parameters. On the other hand, if the interior and exterior orientations of two or more images are already known, then the collinearity equations can be used instead to determine the co-ordinates of a point in object space, provided the image co-ordinates of that point on at least two images are known. As Figure 8 shows, a ray can be formed from the PC of each camera which passes through the representation of each object point on each image. Rays corresponding to the same object point will intersect at the object point in object space.

orientation, allowing a high degree of accuracy to be attained. Furthermore, the use of a control frame in a controlled environment allows for near optimum positioning of the camera. The most accurate results are likely to be obtained by using sets of images which are convergent on the control frame and which have good geometry between the various camera positions. In the test cases presented later in this thesis, the interior orientation of the camera was most often determined from a set of nine images captured from nine camera positions. As the figure below shows, these images where divided up into three sets of images captured from a top, middle and bottom level relative to the control frame. Each set of images was composed of an image captured from the left, middle and right of the control frame.

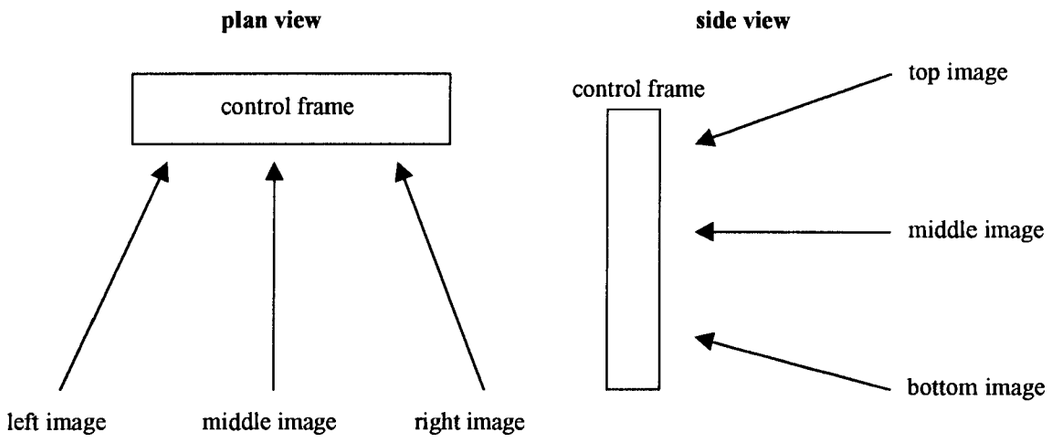

Figure 5 The camera positions in the set of nine images used to determine the interior orientation of the camera

This arrangement of camera positions ensures that the spread of control targets covers the full extent of each image and that sufficient images from various camera positions relative to the frame can be captured. This in turn ensures that the effects of distortions in all parts of the image are modelled by the resultant interior orientation parameters.

Once the interior orientation of a camera is known it is then necessary to determine the exterior orientation of any images which will be used for the photogrammetric measurements of the desired object. A control frame may also be used for the exterior

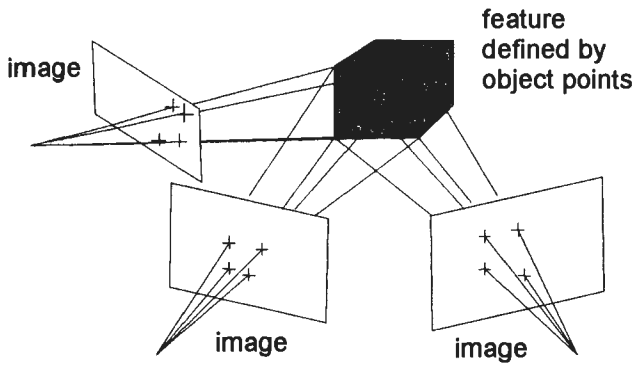

Figure 8 The co-ordinates of object points can be determined by intersection from two or more images

The bundle adjustment combines the process of determining image orientation with that of determining object co-ordinates. It solves simultaneously for both the orientation parameters of images as well as the co-ordinates of unknown object points measured in the images. In order for the technique to be able to solve for the unknowns, the co-ordinates of a number points on a number of images must be measured. Furthermore, good approximate initial values for both the orientations and the object co-ordinates must be known.

A feature of the bundle adjustment is that it uses *a priori* co-ordinates of object points designated as control points in order to determine interior and exterior orientations, as well as the co-ordinates of any unknown points whose initial co-ordinates were not held fixed in the adjustment. This is an iterative process in which the interior and exterior orientations as well as the co-ordinates of any unknown points may be repeatedly updated and refined.

This feature has an important consequence. Provided the approximate co-ordinates are sufficiently accurate and sufficient images are used from camera stations providing good convergent geometry, it is possible to perform a bundle adjustment which achieves accurate results without previously accurately surveying the points used as control points. The points designated as control points need only be points which are clearly defined in the images in which they are present and which have good

approximate co-ordinates. The co-ordinates of these points are updated and refined with each iteration along with the co-ordinates of any other unknown points in the adjustment. These revised co-ordinates are then used as the basis for the next iteration of the adjustment.

This approach to applying the bundle adjustment can be used to determine the interior orientation of a camera because the bundle adjustment does not require an accurate scaling factor between image and object space in order to determine these parameters. An exception is the principal distance which can not be determined correctly because it does require that the correct scaling factor be calculated in the adjustment. However, if it is required that the exterior orientation be correctly calculated, it is necessary to introduce an accurate scaling factor into the adjustment. This can be achieved by holding fixed the distance between two object points, either by holding their co-ordinates fixed or by accurately measuring the distance between the two points and holding the distance itself fixed.

This approach to applying the bundle adjustment was not used in this thesis since in all cases it was more convenient to use accurately surveyed control points. However, further discussion of this application of the bundle adjustment, as well as its limitations, can be found in Karara (1989, pg. 445) and Atkinson (1996, pg. 367).

The bundle adjustment is a flexible technique. It may be used to determine both orientations as well as object co-ordinates in a single process. It can also be used to determine some unknown parameters while holding fixed predetermined parameters. Table 1 below shows the requirements for some of the possible combinations of unknowns that can be solved for using the bundle adjustment. As was mentioned above, it is not strictly necessary to hold the object co-ordinates of the control points fixed, even when orientations are being calculated. However, if accurately surveyed object co-ordinates are available it is normally preferable to hold them fixed in the adjustment.

Required unknowns (assuming that those not required were predetermined)	Which image observations are required		Which parameters should be held fixed in the adjustment	
	Control points	Unknown object points	Object co-ordinates of control points	Interior and exterior orientation
Interior and exterior orientation parameters	yes	no	not strictly necessary	no
Orientation parameters and unknown object point co-ordinates	yes	yes	not strictly necessary	no
Unknown object point co-ordinates	no	yes	no	yes

Table 1 Table showing the requirements for some of the possible combinations of unknowns that can be solved using the bundle adjustment

More specifically, certain conditions must be satisfied if the bundle adjustment is to converge to a solution (Hoffa, 1996):

- every object point must be visible in at least two images
- a minimum of five object points, distributed throughout the image and with ideally some variation of depth in object space, must be visible on each image
- at least two full control points plus an ordinate of a third point must be known in order to provide a datum and orientation for the network
- the number of observations must be equal to or exceed the number of unknowns.

The mathematical formulation of the bundle adjustment follows basic least squares models. The observation equations are formulated by linearising the collinearity

equations through a Taylor series expansion. The standard parametric least squares formulation is given by:

$$v = Ax - l$$

Equation 11

The corrections to the initial approximations of the unknowns can be determined from:

$$x = \left(A^T PA\right)^{-1} A^T Pl$$

Equation 12

where:

A	is the design matrix containing the coefficients of the unknowns
P	is the weight matrix
l	is the vector of free terms
v	is the vector of residuals
x	is the vector of corrections to the initial estimates of the unknown parameters

3.2.2 The Direct Linear Transformation (DLT)

The DLT is an alternative method to the bundle adjustment for determining the interior and exterior orientation of an image. The DLT can be used as a method to determine direct transformation parameters between image and object co-ordinates (Abdel-Aziz and Karara, 1971). It has the advantage over the bundle adjustment in that it does not require any initial approximations of its unknowns. However, two of the eleven transformation parameters are linearly dependent on the other nine. If the dependencies are ignored, only approximate values for the parameters can be determined. As a result the DLT generally produces less accurate results than the bundle adjustment. For this reason the DLT is often used to determine the

approximate orientation parameters of individual images before a final adjustment of the parameters is made using a bundle adjustment.

The equations for the DLT are:

$$x_i - dx_i = \frac{b_{11}X_i + b_{12}Y_i + b_{13}Z_i + b_{14}}{b_{31}X_i + b_{32}Y_i + b_{33}Z_i + 1}$$

$$y_i - dy_i = \frac{b_{21}X_i + b_{22}Y_i + b_{23}Z_i + b_{24}}{b_{31}X_i + b_{32}Y_i + b_{33}Z_i + 1}$$

Equation 13

where:

x_i, y_i	are the image co-ordinates of the projected point
dx_i, dy_i	are the distortion parameters
X_i, Y_i, Z_i	are the object co-ordinates of the point of interest
b_{mn}	are the DLT parameters

The eleven DLT parameters can be converted into physical parameters of interior and exterior orientation (McGlone, 1989). These physical parameters may then be used as final values, or they may be used as initial values for a bundle adjustment. The conversions are given below.

$$\lambda = -1/\sqrt{(b_{31}^2 + b_{32}^2 + b_{33}^2)}$$

$$x_p = (b_{11}b_{31} + b_{12}b_{32} + b_{13}b_{33})\lambda^2$$
$$y_p = (b_{21}b_{31} + b_{22}b_{32} + b_{23}b_{33})\lambda^2$$

$$c_x = \sqrt{\left[(b_{11}^2 + b_{12}^2 + b_{13}^2)\lambda^2 - x_p^2\right]}$$
$$c_y = \sqrt{\left[(b_{21}^2 + b_{22}^2 + b_{23}^2)\lambda^2 - y_p^2\right]}$$
$$c = (c_x + c_y)^2$$

$$\phi = \sin^{-1}(b_{31} * \lambda)$$
$$\omega = \tan^{-1}(-b_{32} / b_{33})$$
$$r_{11} = \lambda(x_p b_{31} - b_{11}) / c_x$$
$$\kappa = \cos^{-1}(r_{11}) / \cos\phi$$

$$\begin{bmatrix} X_c \\ Y_c \\ Z_c \end{bmatrix} = \begin{bmatrix} b_{11} & b_{12} & b_{13} \\ b_{21} & b_{22} & b_{23} \\ b_{31} & b_{32} & b_{33} \end{bmatrix}^{-1} \begin{bmatrix} b_{14} \\ b_{24} \\ 1 \end{bmatrix}$$

Equation 14

where:

x_p, y_p	are the principal point co-ordinates
c_x, c_y	are the principal distances in the x and y image directions respectively
c	is the principal distance
ω, ϕ, κ	are the exterior orientation rotations
X_c, Y_c, Z_c	are the co-ordinates of the perspective centre

3.3 Image Matching

It was earlier stated that in order to either use an object point to orient an image, or to determine the object co-ordinates of the point, the image co-ordinates of that point must be measured in at least two images. Section 3.2 explains how control points can be automatically extracted and identified on each image. However, this relies upon the assumption that the targets appear as bright circles in the image. Very often points on

features to be measured are not as easily identifiable in an image as a target control point might be. Although it may be simple to select points to be measured in one image, by using one of a number of methods to find points of interest, the corresponding points in other images still need to be found in order to determine the object point co-ordinates by intersection. Automatic matching of corresponding points in images is thus a necessity if the object co-ordinates of points are to be found without the need for an operator to manually identify these image points.

A basic least squares image matching algorithm was developed by Gruen (1985). This algorithm automatically locates, in one or more search images, points corresponding to a point in a reference image. The technique establishes correspondence between points in two images by minimising the grey scale value differences between a reference patch around an initially selected point in the first image, and a search patch in the second image (a "patch" is simply a small region of the image). The central point of the patch in the second image at which this difference is minimised is considered to be the point which corresponds to the reference point in the first image. An affine transformation is used to match the reference patch to the corresponding search patch. The search patch in the reference image is generally square shaped whilst the shape of the patch in the search image is affected by the affine transformation parameters.

The reference and search patches can be represented as two dimensional functions $f(x,y)$ and $g(x,y)$. The two patches are assumed to correspond when

$$f(x,y) = g(x,y)$$

Equation 15

However, random noise, radiometric differences, perspective distortions and other factors affect Equation 15. Thus an error vector $e(x,y)$ can be included in Equation 15, resulting in:

$$f(x,y) - e(x,y) = g(x,y)$$

Equation 16

The purpose of the matching process is to determine the position of *g(x,y)* such that $\sum(e(x,y))^2$ is minimised. Equation 16 can be considered a non-linear observation equation which models the observation vector *f(x,y)* with a function *g(x,y)*, the location of which may be determined through a parametric least squares adjustment. The location of *g(x,y)* can be defined by an initial position $g^0(x,y)$ followed by a shift $(\Delta x, \Delta y)$ applied at the initial position.

Image shaping parameters are also introduced to account for systematic image deformations caused by the different perspectives of the images. Image shaping is performed by transforming the co-ordinates of $g^0(x,y)$ and determining new grey values by resampling between the original pixel grey values at the new co-ordinates. The interpolation method applied here, bilinear interpolation, is explained later in Section 6.1.5. The transformation of the image co-ordinates may be performed using an affine transformation as stated below in Equation 17. This transformation includes the shift parameters, a_{11} and b_{11}, as well as two scale factors, a rotation and a shearing angle.

$$x = a_{11} + a_{12}x_0 + a_{21}y_0$$
$$y = b_{11} + b_{12}x_0 + b_{21}y$$

Equation 17

Due to differences in the radiometric properties of the two images, it is also necessary to apply a radiometric shift correction to the grey level values in the search patch. A radiometric shift may be determined from Equation 18 where n is the number of pixels in the two patches.

$$r_s = \frac{1}{n}\left(\sum\left(g(x,y) - f(x,y)\right)\right)$$

Equation 18

Substituting Equation 17 into Equation 16 and then linearising the results by means of a Taylor series expansion, results in the following equation:

$$f(x,y) - e(x,y) = g^0(x,y) + \frac{\partial g^0(x,y)}{\partial x}dx + \frac{\partial g^0(x,y)}{\partial y}dy$$

Equation 19

in which:

$$dx = da_{11} + x_0 da_{12} + y_0 da_{21}$$
$$dy = db_{11} + x_0 db_{12} + y_0 db_{21}$$

Equation 20

If Equation 19 is rearranged and the radiometric shift parameter (Equation 18) is included, the following equation can be formed:

$$f(x,y) - e(x,y) = g^0(x,y) + G_x da_{11} + G_x x_0 da_{12} + G_x y_0 da_{21} +$$

$$+ G_y db_{11} + G_y x_0 db_{12} + G_y y_0 db_{21} + r_s$$

Equation 21

Here G_x and G_y are the grey scale gradients in the x and y directions respectively at each point in the patch. G_x and G_y are given by:

$$G_x = \frac{\partial g^0(x,y)}{\partial x} = \frac{g(x+1,y) - g(x-1,y)}{2}$$
$$G_y = \frac{\partial g^0(x,y)}{\partial y} = \frac{g(x,y+1) - g(x,y-1)}{2}$$

Equation 22

The corrections to the initial transformation parameters in Equation 20 can be determined by solving Equation 21 by means of a least squares adjustment which has the solution

$$x = (A^T PA)^{-1} A^T P\ell$$

Equation 23

where:

$$x^T = (da_{11}, da_{12}, da_{21}, db_{11}, db_{12}, db_{21}, r_s)$$

Equation 24

$$\ell = f(x,y) - g^0(x,y)$$

Equation 25

Initial estimates for the unknown transformation parameters can be set to the values:

$$a_{11}^0 = b_{11}^0 = a_{21}^0 = b_{12}^0 = 0$$
$$a_{12}^0 = b_{21}^0 = 1$$

The final values for these parameters are determined through an iterative solution by continuously applying the corrections obtained from the solution vector (Equation

24) to update the parameters. The solution is considered to have converged when all the elements of the solution vector are below a chosen threshold. The final position of the matched point in the search image is then given by Equation 17.

The technique of image matching described above is neither guaranteed to converge to the correct solution, nor to converge at all. A number of refinements and additions to the technique have been made to overcome some of the limitations of the basic least squares image matching technique. One such resulting method is that of multi-photo geometrically constrained (MPGC) matching as described by Baltsavias (1991). MPGC matching uses knowledge of the orientation of each image to constrain the search area in the images to areas in which the point to be matched is most likely to be found. A further refinement to MPGC matching is the use of multi-image correlation (MIC) as proposed by van der Vlugt (1995). Use of this technique further reduces the regions of the images in which the corresponding points are searched for. Incorporating MIC into the matching process reduces the possibility of mis-matches and increases the success rate.

4 REVIEW OF SOME CYLINDER PARAMETER DETERMINATION TECHNIQUES SUITABLE FOR DIGITAL PHOTOGRAMMETRY

Measuring the parameters of a cylinder may be accomplished by various methods other than photogrammetry. However, photogrammetry, whether it be analogue, analytical or digital based, offers some distinct advantages over other non-photogrammetric methods. Techniques to extract the parameters of a cylinder from a digital image should make full use of the benefits that working in both a digital and a photogrammetric environment offers, as well as addressing the restrictions imposed by digital photogrammetry. An obvious benefit of working in a digital environment is that computationally expensive methods are often more easily applied and can be performed faster than in a non-digital environment. An important benefit of working in a photogrammetric environment is that it presents the possibility of using techniques that are *only* possible using photogrammetry and which may be superior to non-photogrammetric techniques. Thus digital photogrammetry allows the automation (either semi or fully) of measurement techniques which may be computationally expensive and which may only be possible using photogrammetry.

This chapter reviews two currently existing techniques suitable for measuring the parameters of a cylinder using digital photogrammetry. The techniques approach the problem in two different ways by:

- utilising points on the circumference of the cylinder (Cammidge,1996)
- best fitting a cylinder through its surface points (Chandler & Cooper, 1991)

These two techniques, whilst not being exclusively photogrammetric, do lend themselves well to this form of measurement. Both gain significantly from being

implemented in a digital environment which allows many aspects of the techniques to be automated. These two techniques rely on a point-based approach in which points in the image are mapped to points in object space. Both of these techniques could have a place in a digital photogrammetric software solution, however, as will be discussed, both have some shortcomings. Its is for this reason that a further technique will be introduced.

This additional technique, which is introduced towards the end of this chapter and later discussed in detail in Chapter 4.1, can easily be applied using photogrammetry. In this thesis it has been developed in a digital photogrammetric environment which simplifies both the measurement and the calculation processes in comparison to other environments. This technique makes use of the information contained in the pipe's visible edges. The approach is based on mapping lines on the image to lines in object space and as such has more in common with line photogrammetry, from which it was inspired, than point-based photogrammetry.

4.1 A Technique Utilising Circumference Points

Any cylindrical object can be defined by seven parameters; its radius, a point on its longitudinal axis (three parameters) and either a direction vector (three parameters) or another point on the longitudinal axis (three parameters).

A simple point-based technique utilising the information inferred by the circumference of the cylinder, requires only three object points lying on a visible circumference. From this, the radius and, with limited accuracy, the direction of the pipe can be determined. For a more detailed explanation of this technique than this section offers, as well as an investigation into the technique, the reader is directed to Cammidge (1996).

It is possible to fit a circle through any three points in object space using vector geometry. As show in Figure 9, the three points A,B,C form two chords on the circle, two vectors in space.

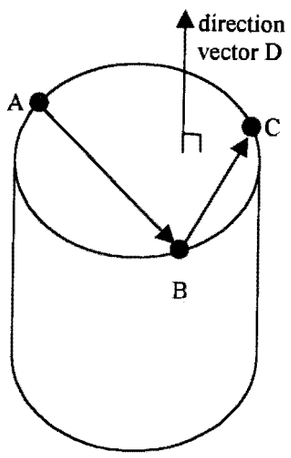

Figure 9 Circle through circumference points

The result of Equation 26 below produces the direction vector D orthogonal to the circle passing through the three points. If the three points lie on the circumference of a cylinder, then vector D gives the direction vector of the cylinder. These are three of the parameters necessary to define the cylinder in space.

$$D = AB \times BC$$

Equation 26

The radius of the circle can also be calculated using the two chords AB and BC. With this aim, a vector can be formed complying with the conditions:

- that it lie in the plane formed by ABC
- that it be orthogonal to AB

- that it pass through the centre of the circle formed by ABC.

In order to comply with the first two conditions, the vector must be orthogonal to both vector D and any of the vectors AB, BC, or CA, hence its direction can be given by

$$Rd_1 = D \times AB$$

Equation 27

Referring to Figure 10, it can be seen from simple geometry that the desired vector (Rp_1M) will, if it complies with the three stated conditions, pass through the mid-point of chord AB at Rp_1, where Rp_1 is given by Equation 28.

$$Rp_1 = A + \frac{1}{2}AB$$

Equation 28

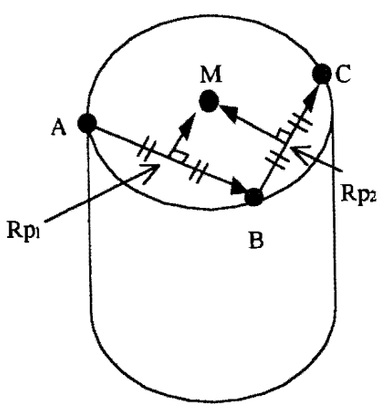

Figure 10 Circle centre bisector vectors

Basic two dimensional geometry states that a vector orthogonal to a chord and passing through the chord's midpoint will also pass through the centre of the chord's circle.

Hence the vector Rp_1M lies in the plane of the circle and passes through the mid-point of the circle at M; it complies with the stated conditions.

Similarly, the vector Rp_2M passing through the mid-point M, lies in the plane of the circle and is orthogonal to BC.

In theory the two vectors Rp_1M and Rp_2M intersect at M, the circle centre. However, due to rounding errors, it is likely that while they might pass close to each other, they do not intersect. Hence Cammidge uses a least squares technique and the equations given below to find the best-fitting intersection point.

$$s_1 Rd_1 + Rp_1 = M + \varepsilon_1$$

Equation 29

$$s_2 Rd_2 + Rp_2 = M + \varepsilon_2$$

Equation 30

Equation 29 and Equation 30 form the basis of the least squares calculations where s_1 and s_2 are the scale factors applied to the vectors with direction Rd_1 and Rd_2 originating from points Rp_1 and Rp_2 respectively. The error vectors ε_1 and ε_2 describe the shortest distance between the vectors originating from Rp_1 and Rp_2 respectively and the mid-point of the circle M. These error vectors apply small shifts to M to ensure that despite the previously mentioned rounding errors, M has the same value in both equations. If M lies midway between the shortest vector connecting the two vectors originating from Rp_1 and Rp_2, then Equation 31 holds true.

$$\varepsilon_1 - \varepsilon_2 = 0$$

Equation 31

If the best value of the mid-point M is considered to be that in which Equation 31 holds true, then Equation 32 can be formed by rearranging Equation 29 and Equation 30 and writing them in vector form.

$$\begin{bmatrix} (Rd_x)_1 & -(Rd_x)_2 \\ (Rd_y)_1 & -(Rd_y)_2 \\ (Rd_z)_1 & -(Rd_z)_2 \end{bmatrix} \begin{bmatrix} s_1 \\ s_2 \end{bmatrix} = \begin{bmatrix} (Rp_x)_2 - (Rp_x)_1 \\ (Rp_y)_2 - (Rp_y)_1 \\ (Rp_z)_2 - (Rp_z)_1 \end{bmatrix}$$

Equation 32

The values s_1 and s_2 in the above equation can be solved using a least squares approach. Once s_1 and s_2 are known, M can be determined from:

$$M = \frac{1}{2}[(Rp_1 + s_1 Rd_1) + (Rp_2 + s_2 Rd_2)]$$

Equation 33

These calculations produce a further three of the desired parameters.

Finally, the radius (R) of the cylinder can be found by any of :

$$R = |M - A|$$
$$R = |M - B|$$
$$R = |M - C|$$

Equation 34

Cammidge suggests determining R from the mean of the three values obtained using the equations in Equation 34.

The seven parameters defining the cylinder in object space have now been determined.

The actual measurement process as implemented by Cammidge involves the user manually identifying, on one image, three points known to lie on a single line defining the circumference of the pipe. The image co-ordinates of points corresponding to those points manually identified in the first image are found in a second image by the process of image matching (see Section 3.3 for a brief explanation of image matching). Once the image co-ordinates of the points are known in two images, it is trivial to determine the object co-ordinates of the points that are necessary for this method.

This technique has the benefits of being very quick and easy to implement. It has minimal requirements; only two images are required and only three points need to be identified in the first image with the corresponding image points in the second image being found through image matching.

However, it does have some shortcomings as well. The greatest is related to the identification of the three initial points. Since the technique relies completely on three points lying on the circumference of the cylinder, it will only work when a circumference is well defined. On smooth pipes, with poorly defined circumference lines, this poses a problem and would render the technique useless. This has particular significance for the measurement of cylindrical objects other than pipes. However, where welding and joining lines are visible on the pipe this technique can be used. It should also be kept in mind that the weld lines themselves may not be perfectly circular, nor necessarily flush with the surface of the pipe. Both the lack of circularity as well as the deviation from the true surface of the pipe will affect the positioning of the three initial points such that they do not lie exactly on the ideal circumference of the pipe.

Furthermore, the distribution of the three points with respect to each other around the circumference of the pipe will also affect the overall accuracy of the results. The closer the points are to one another, the more poorly they represent the curvature of the cylinder and the greater the chance that small inaccuracies in the positioning of the points will magnify, thereby resulting in great inaccuracies in defining the circle through these points (refer to Figure 11). This has the effect that the closer the three points are to one another, the more imperative it becomes that their positional accuracy be high. Any inaccuracy in determining the object co-ordinates of these three points has a greater overall effect the closer they are together since their accuracy affects the ability of Equation 26 to determine D accurately. This consequently affects the accuracy with which the other parameters can be determined.

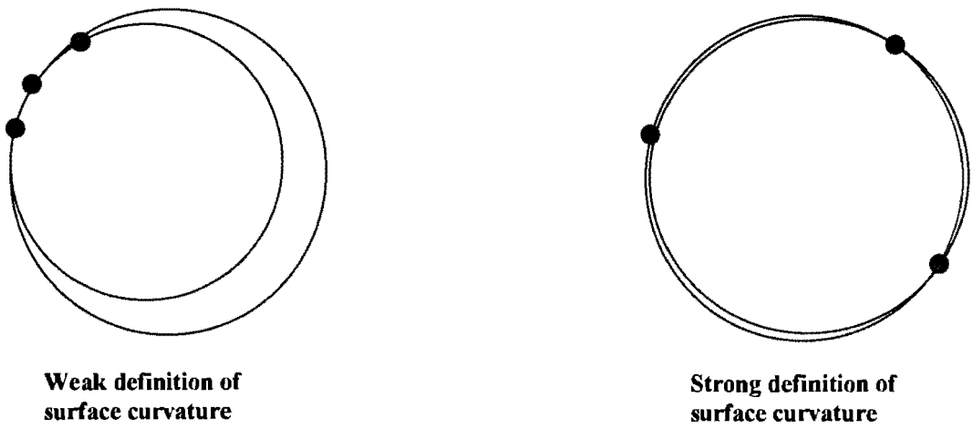

Figure 11 Weak and strong surface curvature representation through 3 points

One further possible shortcoming of this approach was that Cammidge pointed to the circumference points on the first image manually, by means of visual inspection. If higher accuracies were required, an automated method to extract points on the circumference of the pipe in the image would be required. Such a method would ideally not rely on raised weld lines and would be able to determine the position on the circumference line to sub-pixel accuracy.

The factors mentioned above have the result that whilst it ought to be possible to calculate a point on the axis of the pipe with some degree of accuracy, the final accuracy with which the cylinder parameters can be determined is heavily influenced not only by the accuracy with which the three initial object points can be determined, but also by how well distributed these points are around the cylinder's circumference. It is possible to use more than three points on the defined circumference in order to allow for some redundancy. This will reduce the criticality of the accuracy of the individual points. However, it does not reduce the importance of ensuring that the points do in fact lie on the true circumference and that they do represent the curvature of the cylinder sufficiently well.

In conclusion, this technique has the benefit of being rapid and easy to implement. However, it has the draw back that if a circumference line in the images is poorly defined or if the points defining the circumference cannot be accurately calculated in object space, the technique becomes only suitable for low to moderate accuracy requirements. If a circumference line cannot be defined on the image this technique cannot be used.

4.2 Best Fitting Cylinder

Some of the problems associated with the technique presented in Section 4.1 can be overcome if an algorithm can be devised which utilises points anywhere on the surface of the cylinder. Chandler and Cooper (1991) proposed one such method. In order to determine the parameters of the cylinder, their method uses a least squares approach to best fit a cylinder through points assumed to lie on its surface. Figure 12 indicates this concept.

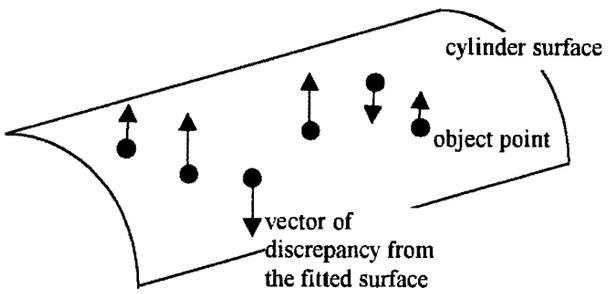

Figure 12 A cylindrical surface can be best fitted through surface object points

This technique has at least one distinct advantage over the technique described in Section 4.1 in that it is not based on the visibility of any particular parts of the pipe, such as circumference lines. Use is made of random points that can be measured in object space on the surface of the cylinder.

Chandler and Cooper choose to define the parameters of a cylinder in space as a point on a line and a direction vector, which together define the position and orientation of the cylinder. The final parameter is its radius.

They base their mathematical formulation on the fact that any point that lies on the surface of a cylinder lies at a constant orthogonal distance from the cylinder's longitudinal axis and that this distance is, by definition, the radius of the cylinder. Using this statement they formulated the following relationship:

$$R^2 - \frac{[l(Y_i - Y) - m(X_i - X)]^2 + [m(Z_i - Z) - n(Y_i - Y)]^2 + [n(X_i - X) - l(Z_i - Z)]^2}{(l^2 + m^2 + n^2)} = 0$$

Equation 35

where:

X,Y,Z are the co-ordinates of an arbitrary point on the axis

l,m,n are the direction ratios of the longitudinal axis

R is the radius of the cylinder

X_i, Y_i, Z_i are the object co-ordinates of point i on the surface of the cylinder.

This equation is based on the equation used to determine the distance from a point in object space to a line in object space. Equation 35 simply states that any point (X_i, Y_i, Z_i) on the surface of a cylinder with parameters (X, Y, Z, l, m, n, R) will lie an orthogonal distance, that of the radius, away from the cylinder axis.

Chandler and Cooper solve the seven unknowns in Equation 35 using a least squares approach. They use the "combined case" of the least squares model since it is not possible to separate the observations from the unknowns in Equation 35. The form of the combined case model is given in by:

$$Ax + Bv + w = 0$$

Equation 36

where:

- A is the design matrix containing the coefficients of the unknowns
- x is the vector of corrections to the initial estimates of the unknown parameters
- B is the coefficient matrix of the residuals
- v is the vector of residuals
- w is the vector of discrepancy terms

Equation 35 is linearised by means of a Taylor series expansion to comply with the criteria that in the Gauss-Markov model of the least squares adjustment observation equations must be linear.

The design matrix A is formed from the partial differentials of Equation 35 with respect to the unknowns in the x vector. A new row is added to the matrix for each point measured on the surface of the cylinder. This results in the matrix having dimensions (n x 7), where n is the number of surface points measured.

The B matrix has a new row for each measured point. The columns, however, correspond to the partial differentials of Equation 35 with respect to each ordinate of the measured point. Each measured point is referred to only once in the matrix resulting in the matrix having dimensions (n x $3n$).

From Equation 35 and Equation 36, the following solution vector can be determined:

$$x = (A^T (BP^{-1}B^T)^{-1} A)^{-1} A^T (BP^{-1}B^T)^{-1} w$$

Equation 37

where:

P is the weight matrix of the measured co-ordinates

The weight matrix used may be formed from the variance-covariance matrix obtained from the photogrammetric point adjustment used in determining the object co-ordinates of the surface points. Either the full matrix may be used or only those terms on the principal diagonal.

Initial approximate values for the cylinder parameters are required for the least squares solution. These are calculated from the object points measured on the surface of the cylinder. Cooper and Chandler determine the provisional value of the point on the cylinder axis by taking the mean value of all the object co-ordinates of all the surface points. The initial direction is calculated from two surface points which lie in the approximate direction of the cylinder's axis. The radius is determined as being the

distance from the provisional point on the axis to one of the surface points. They report that this provides sufficiently accurate provisional estimates to allow the least squares computation to converge to a solution.

The advantage of this technique is that unlike the previously described technique (section 4.1), the points measured on the cylinder surface do not need to lie on a defined circumference. An added advantage is that the reliance on a human operator or an extraction process accurately identify points on the circumference, an inevitable source of error in the first technique, is reduced.

Although this technique was initially developed for use in a non-digital environment, it readily lends itself to a digital photogrammetric environment. The numerous surface points required can quite easily be obtained via the initial application of an interest operator to a single image of the cylinder (provided the cylinder surface contains sufficient texture), followed by geometrically constrained multi-photo matching. This would result in a list of object points on the surface of the cylinder.

The method, however, has a similar disadvantage to the previously mentioned technique. It is important to obtain as great a spread of points as possible around the "curvature" of the surface of the pipe in order to ensure the maximum possible accuracy of the axis position. In order to obtain high directional accuracy it is important to have a good spread of points along the directional axis of the pipe. Clearly, as Chandler and Cooper state, a good spread of points located on the circumference of two imaginary circles at either end of the cylinder will produce the most accurate results.

4.3 Shortcomings of the Two Methods

Both methods are object point based techniques; they rely on mapping individual points in image space to points in object space. Although the method described in Section 4.2 is superior, it is faced with the same challenge as the method described in

Section 4.1; identifying relevant points in one image and then matching them in a second image (or perhaps multiple images). The problem associated with identifying suitable points using first technique is clear and has been remarked upon in Section 4.1. The second technique relies on the fact that there is suitable texture on the cylinder surface which can be matched in the other images. It cannot be assumed that suitable texture will always exist on the pipes and certainly suitable texture will often not exist in the case of other cylindrical objects.

Furthermore, both point based methods require that at least one other image exists in which the desired object points are visible. This places restrictions on the selection of camera positions. While it is desirable to keep the number of images used to a manageable amount, it is necessary to ensure that there is sufficient overlap between each pair of images. In order to provide good geometric coverage of the cylinder for these methods and to ensure the most accurate results, it is likely that at least two *pairs* of images will need to be captured.

4.4 The Concept of Line Photogrammetry

What is required to replace or supplement the two methods described is a method which is not based on object points and thus removes some of the restrictions imposed by point based methods. This proposed new method should be capable of being applied even when there is no surface texture of any kind; neither circumference nor general surface data. Ideally, the method should not be reliant on point correspondence between images and hence it should not be necessary for overlapping images of the cylinder to be captured. Furthermore, it would be advantageous if the technique could work in environments where some parts of the cylinder are obscured by other intervening objects. One such novel technique has been developed out of the concept of line photogrammetry. This technique will be explained in detail in Chapter 5. However, this current section continues by presenting an overview of the general concept of line photogrammetry.

Line photogrammetry is a general photogrammetric technique which is often used in place of point-based photogrammetry. Zielinski (1993) states

> "the reason for using line photogrammetry instead of point oriented stereo photogrammetry is that no stereo point-to-point relationship is required. The parameters of a line in object space can be calculated by measuring different parts of the line in two or more images. The images do not even have to overlap provided the same line is measured in both images."

Point photogrammetry maps image points to rays extending from the PC of the camera to the point in object space. The intersection of rays from two images results in the determination of the co-ordinates of a single object point. In comparison, line photogrammetry maps lines in images to planes in object space. The intersection of two planes defines a line in space.

4.4.1 Line Representation in Image Space

A line may be represented in image space in one of four ways.

1. A line may be represented by two points (x,y) through which the line passes in the image. This is perhaps the simplest representative form. However, it is often necessary to convert from this form to another for certain calculations in the image plane.

2. A line may be defined by the intercepts it makes with both the x and the y axes, resulting in the parametric equation:

$$\frac{x}{a}+\frac{y}{b}+1=0$$

Equation 38

where:

a and b are the x-axis and y-axis intercepts respectively

(x,y) are the co-ordinates of any point on the line

3. A line may also be represented by its gradient and its intercept with either the x or y axis. This form is convenient for certain calculations in the image plane and is the form used by the author in Section 5.1.

$$y = ax + b$$

or

$$x = \frac{1}{a}y - b'$$

Equation 39

where:

a is the gradient of the line

b is the y-axis intercept

$-b'$ is the x-axis intercept

4. A line may be described trigonometrically in a polar representation by the parameters θ and ρ as given in Equation 40 and indicated in Figure 13 where ρ is the shortest distance from the line to the origin.

$$x\cos\theta + y\sin\theta - \rho = 0$$

Equation 40

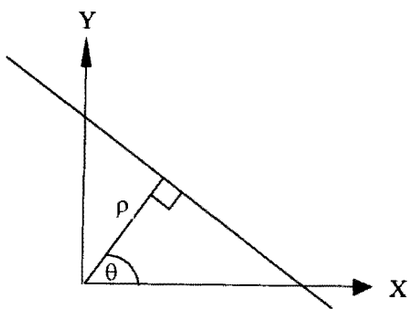

Figure 13 Trigonometrical representation of a line

4.4.2 Line Representation in Object Space

A variety of ways to represent a line in object space exist. Three of these are outlined below.

1. Mulawa choose to represent a line in object space for his formulation of the coplanarity constraint for line photogrammetry using a six parameter form. His representation of an arbitrary point on an infinite line is given by Equation 41 and shown in Figure 14.

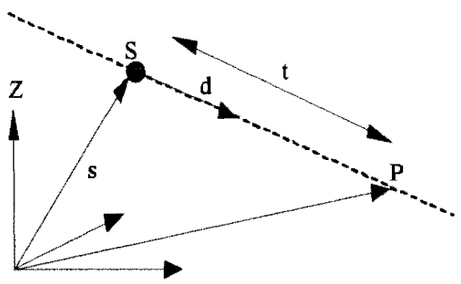

Figure 14 Six parameter representation of a 3D line

$$p = s + td$$

Equation 41

where:

p is the vector from the origin to the point P on the line

s is the vector from the origin to a point S on the line

d is the direction vector of the line

t is a scaling factor used to define P

The six defining parameters are thus (X_S, Y_S, Z_S) of the point S and (X_d, Y_d, Z_d) of the direction vector d.

The point S can be arbitrarily chosen as can the length of the direction vector d. It is necessary to apply two constraints in order to reduce the degrees of freedom of this representation to four, thereby uniquely defining a line in object space. This can easily be achieved by adding the constraint that the length of d should be unity, as formulated in Equation 42, and that the distance between point S and the origin be minimised i.e. that vectors s and d be orthogonal as indicated in Equation 43.

$$|d| = 1$$

Equation 42

$$d \bullet s = 0$$

Equation 43

2. Zielinski (1993) takes a different approach to representing a line in object space. He uses a formulation which has only four parameters; a scalar distance and three rotations. This interesting representation allows Zielinski to reduce some of the numerical problems that would otherwise have arisen in his implementation of line photogrammetry had he represented a line differently.

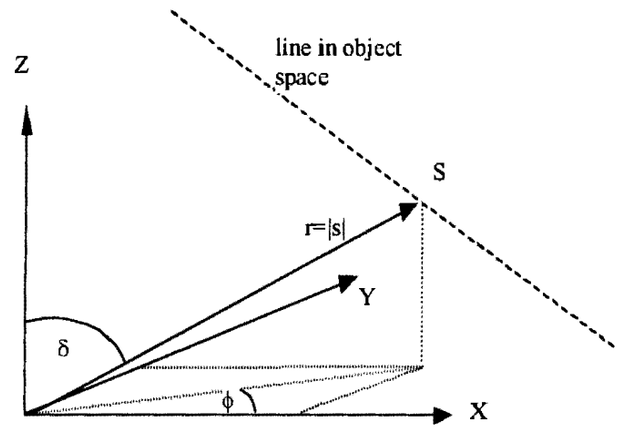

Figure 15 Polar co-ordinates of point *S*

In Figure 15 the point *S* can be defined in terms of polar co-ordinates (ϕ, δ, r). Point *S* is the point on the line closest to the origin. The scalar *r* is the distance from the origin to point *S*. The direction of vector *s* pointing to *S* can be defined by two angles. δ is the angle between vector *s* and the Z-axis and angle ϕ is the angle between the projection of the vector onto the X-Y plane and the X-axis. Thus three (ϕ, δ, r) of the four necessary parameters have been defined.

In order to obtain the final parameter, Zielinski defines a spherical co-ordinate system with its origin at point *S* (referring to Figure 16). The co-ordinate system is oriented such that the e_δ-axis is directed tangential to the meridian through *S*. Similarly the e_ϕ-axis is directed tangential to the parallel circle through *S*. The last axis, e_r, is directed such that it is normal to the plane e_δ-e_ϕ. Since by definition, *d*, the direction vector of the line in object space, always lies in the plane e_δ-e_ϕ, the fourth parameter γ can be defined as the angle between *d* and the e_δ-axis. Thus as Figure 16 shows, Zielinski can define a line in object space with 4 parameters (ϕ,δ,γ,r).

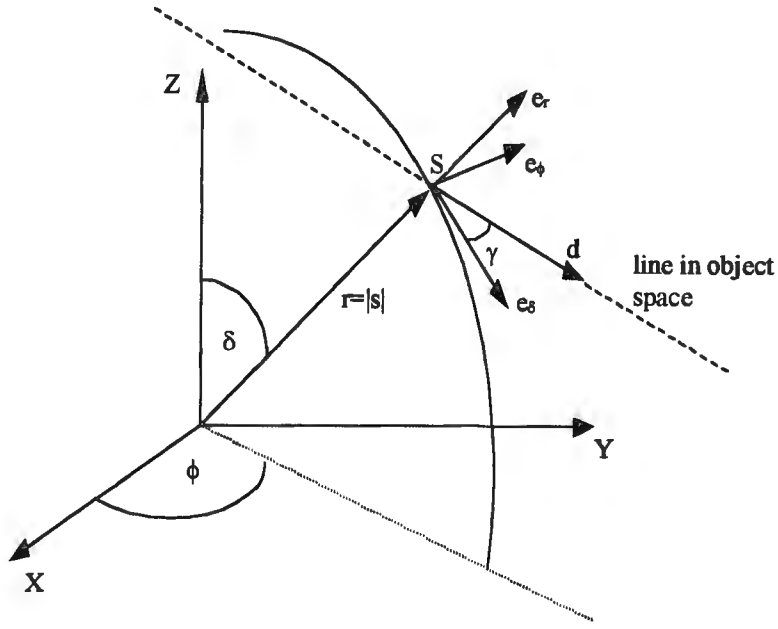

Figure 16 A line in object space expressed by the four parameters r,ϕ,δ,γ

3. Yet another way of representing a straight line in object space is to define a line as the intersection of two planes (Figure 17).

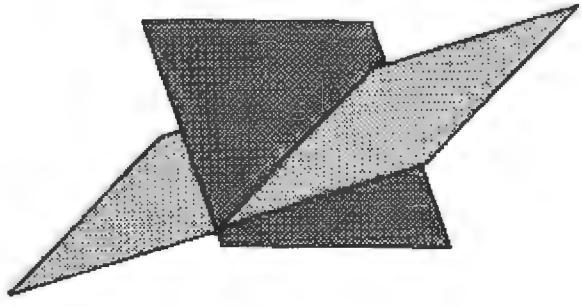

Figure 17 A line in object space defined by the intersection of two planes

The line can be represented by the parameters $(A_1,B_1,C_1,A_2,B_2,C_2)$ of two planes, as stated in Equation 44.

$$A_1X + B_1Y + C_1Z + 1 = 0$$
$$A_2X + B_2Y + C_2Z + 1 = 0$$

Equation 44

This is the representation used by the author in the cylinder parameter determination technique presented in Section 4.1, since it is the representation most easily adapted to that measurement technique.

4.4.3 Relating Lines in Object Space to Image Space

In order to make use of the information contained in lines in object space, some method is required to relate lines in object space to those visible in image space. A method to model this relationship, common in line photogrammetry, is by means of the coplanarity condition as stated by Mulawa and Mikhail (1988). The coplanarity constraint, together with Mulawa's parametric form of a line in object space (as stated in Section 4.4.2), allows the calculation of the parameters of a three dimensional line using any number of image observations in two or more images.

The features of the coplanarity constraint are shown in the Figure 18.

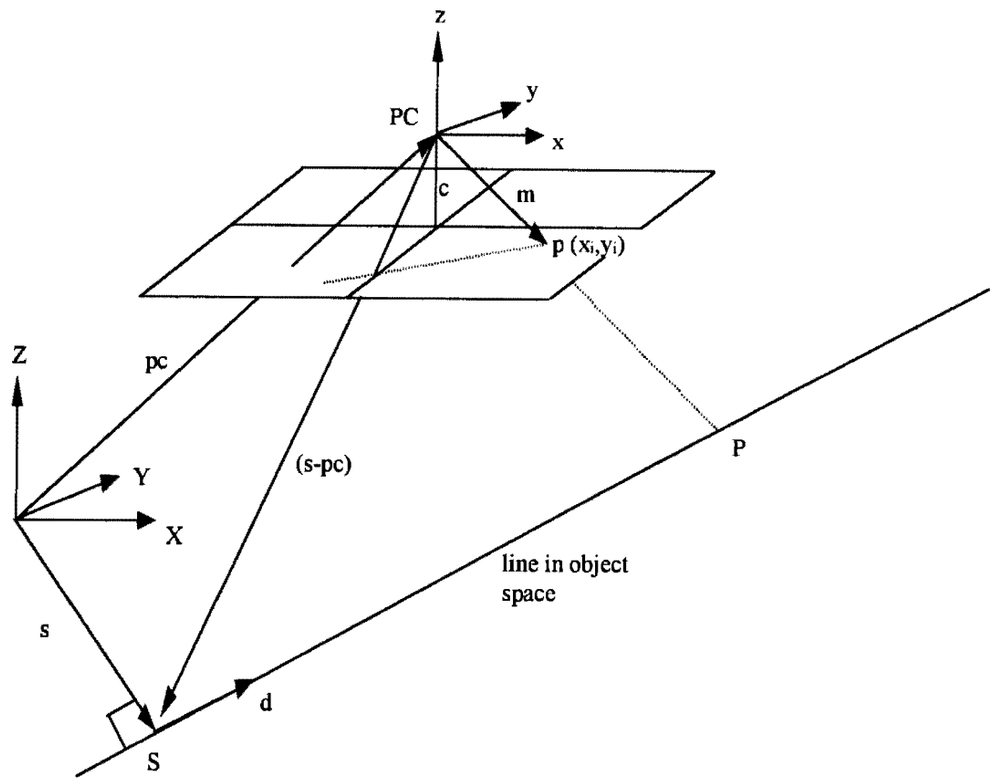

Figure 18 The coplanarity constraint defining the relationship between an object line and image space

The representation of the line in object space is the same as that mentioned in Section 4.4.2. Point S is the closest point on the line to the origin of the object co-ordinate system. The vector s is a vector from the origin of the object co-ordinate system to the point S on the line in object space and is orthogonal to the direction vector d of the line. P again represents an arbitrary point on the three dimensional line. pc is the vector from the origin of the object co-ordinate system to the camera PC. Thus $(s\text{-}pc)$ defines the vector from the PC to the point S on the three dimensional line. x_i and y_i are the image co-ordinates of the point p and c is the principal distance.

The vector m represents the observation ray through p to the object point P on the line in object space. Vector m will only coincide with the line joining PC to P if the rotation matrix R, as given in Equation 46, is known. The image must be oriented with respect to the object co-ordinate system. Thus the three rotation angles (ω,ϕ,κ) which form the elements of the rotation matrix R must have been determined. The

coplanarity condition can be expressed in the form given in Equation 45. Equation 45 states that all three vectors lie in the same plane i.e. that they are coplanar.

$$|s - pc, d, m| = 0$$

Equation 45

where:

$$m = R^T \begin{bmatrix} x_i \\ y_i \\ c \end{bmatrix}$$

Equation 46

and:

$$R^T = \begin{bmatrix} r_{11} & r_{21} & r_{31} \\ r_{12} & r_{22} & r_{32} \\ r_{13} & r_{23} & r_{33} \end{bmatrix}$$

Equation 47

Each observation to a point on the image provides an equation of the type given in Equation 45. Thus the unique determination of the parameters of a line in object space using two observations to the line in each of two images, provides four equations of the type shown in Equation 45. This is graphically indicated in Figure 19 in which each image has its own rotation matrix (R^T) and principal distance (c_i) which are used to calculate the observation vectors m_{ij}. Since two arbitrary chosen and four fixed parameters are needed to define the line (using Mulawa's object line representation), the four equations (of the type shown in Equation 45) are combined with the two constraints imposed by Mulawa's line representation. The parameters can now be solved for.

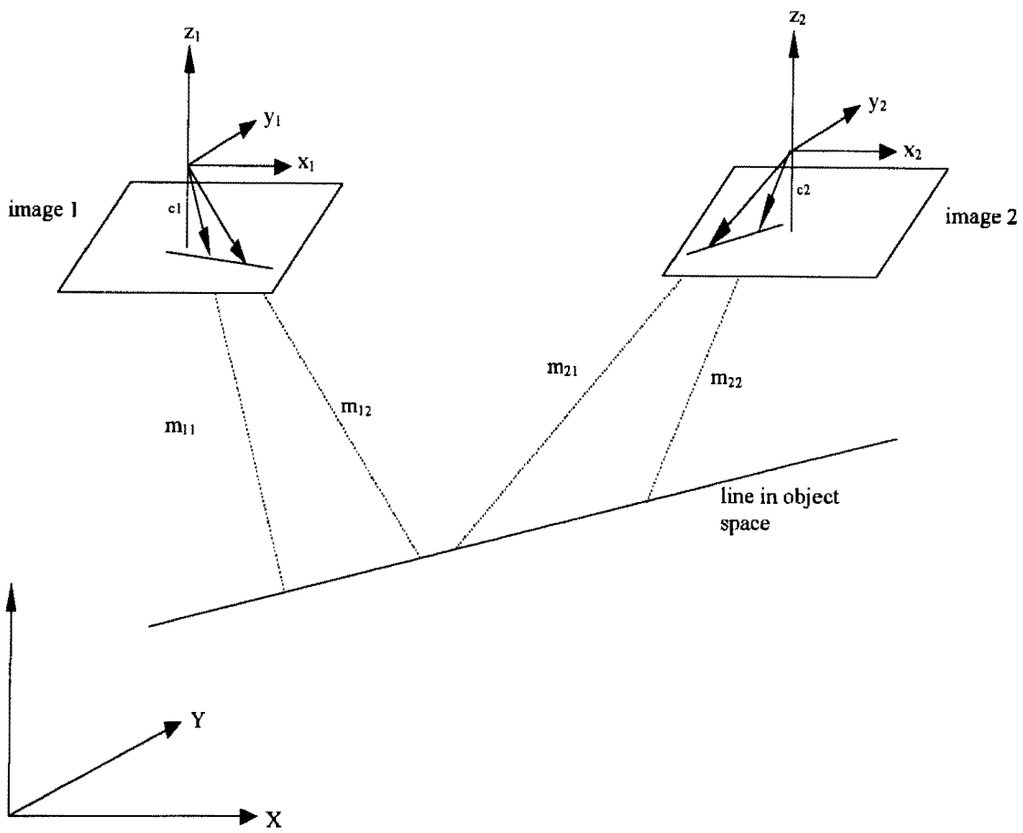

Figure 19 A line in object space determined from four image rays originating from two images

It can be seen that classic line photogrammetry appears to offer the potential to fulfil the requirements for a novel technique to measure cylinders. However, it has one drawback. While it does not require corresponding points to be present in images, nor does it even require any overlap of the line of interest between images, it does require that the same line be measured in both (or in the case of a redundant set-up, all) images. In the case of the measurement of cylindrical pipes, unless a line is clearly defined on the surface of the pipe, which is neither practical nor desirable, the use of classic line photogrammetry is not possible.

Chapter 5 presents a technique for calculating the parameters of a cylinder which is inspired by the concept of line photogrammetry. The technique has the benefits of line photogrammetry while at the same time not requiring any single line to be present in more than one image.

5 SILHOUETTE-EDGE METHODS

Chapter 4 described two digital photogrammetric methods suitable for determining the parameters of a cylinder. It also noted the shortcomings of these two methods and stated the requirements that an additional supplementary or replacement technique should have. Any new technique should not be limited by the restrictions imposed by requiring points to be matched between images. Furthermore, it would be advantageous if no part of the cylinder need appear in more than one image. It was shown that a technique based on line photogrammetry might fulfil these requirements and the theory of line photogrammetry was discussed.

However, in order to define a line in object space, line photogrammetry requires that sections of the same line appear in all images. As a result of this requirement, the model of line photogrammetry described in Chapter 4 is unsuitable. This chapter will present a method derived from line photogrammetry concepts which can be used to determine the parameters of a cylinder.

A cylinder is curved, so it has no well defined edges in the way that, for instance, a cube does. However, when a cylinder in object space is projected into two dimensional image space, as occurs when an image is captured, it produces a two dimensional feature which does have well defined edges (refer to Figure 20).

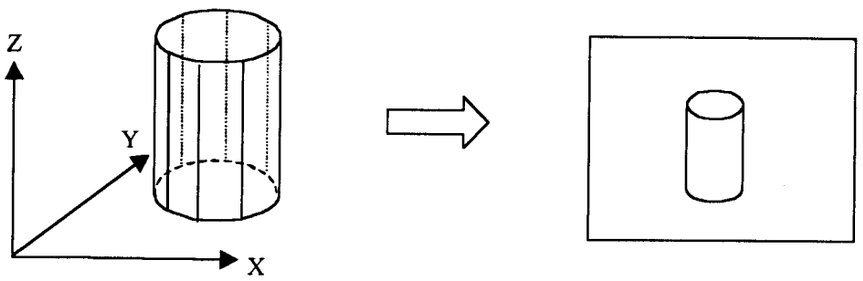

A cylinder represented in three dimensions

A cylinder represented in two dimensions

Figure 20 Two and three dimensional representations of a cylinder

This effect fulfils one of the prerequisites for line photogrammetry which requires that lines, as opposed to merely discrete points, be present in the images. However, as was previously mentioned it does not fulfil the criteria that the same line be visible in all images. Clearly, as can be seen in Figure 21, the edges formed by the projection of the cylinder into two dimensional space do not correspond with the same line in object space if the camera positions are not the same. It is this fact that prevents the use of line photogrammetry in its original form. However, elements of the concept of line photogrammetry may still be used to develop a new technique based on silhouette edges and the assumed circular shape of the cylinder.

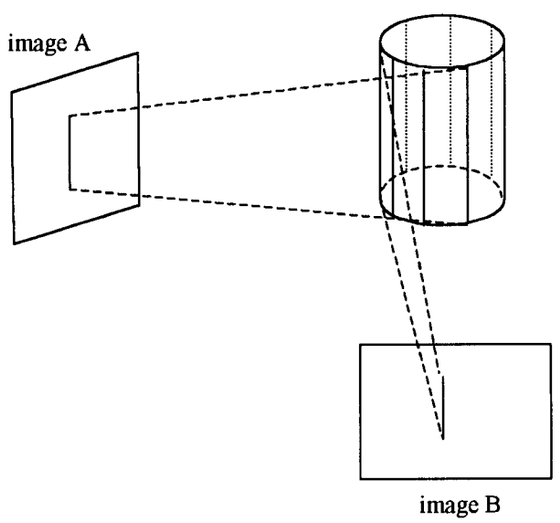

Figure 21 The silhouette edges projected onto the images differ for each image position

5.1 Using Tangential Lines to Determine the Position of a Circle in Two Dimensions

The solution to determining the position of a cylinder in three dimensions can perhaps be more easily understood by first looking at a similar two dimensional problem as indicated in Figure 22. The task is to determine the centre co-ordinate of the circle as well as its radius based on the known positions of the four lines tangential to the circle.

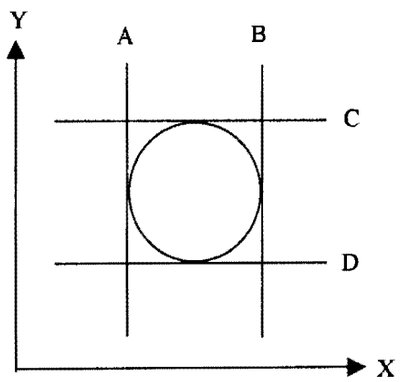

Figure 22 A circle uniquely defined within four lines

Clearly it can be seen that, provided the parameters defining each of the four lines (A,B,C and D) are known, basic geometry will allow the unknown centre and radius values to be calculated. The assumptions made are that the four lines are tangential to the circle and, obviously, that the circle is truly circular.

Figure 23 shows a method of solving this problem.

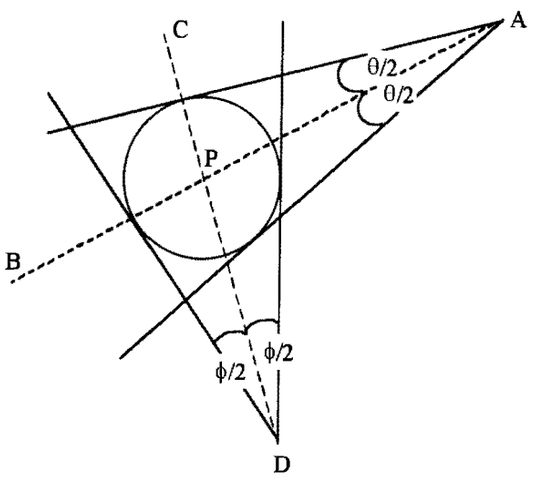

Figure 23 The use of tangential lines and their angular bisectors to determine the circle centre

A line *AB*, which is the acute angular bisector of the two lines tangential to the circle and passing through *A*, can be found. This line will pass through the point *P* which is the centre point of the circle. Similarly, the acute angular bisector *CD*, of the two lines meeting at *D* can be found and this line will also pass through *P*. If the defining parameters of each of these lines are known, then the parameters of the line *AB* can be solved for as can those of the line *CD*. From this the co-ordinates of the centre point of the circle *P* can be calculated from:

$$x_P = \frac{d-b}{a-c}$$
$$y_P = ax_P + b$$

Equation 48

where:

a and *b* are obtained from y=ax+b (the defining equation of line *AB*)

c and *d* are obtained from y=cx+d (the defining equation of line *CD*).

It can be seen that in two dimensional space, if a pair of lines originate from each of two points, and each line is assumed to be tangential to a circle, then they will uniquely define a single circle. A similar situation exist in three dimensions.

5.2 Using Silhouette Edges to Determine the Position of a Cylinder in Three Dimensions

During image capture the cylinder in object space is projected into two dimensional space. As shown in Figure 24, the silhouette edge of the pipe in object space (P_1P_2), the corresponding line produced in image space (p_1p_2) and the PC of the camera are all coplanar. Obviously the projection of the silhouette edge of the cylinder onto the image is formed by light rays which are tangential to the cylinder. As a result, assuming the image has been oriented, any plane which is formed through points p_1,p_2 and PC will pass through P_1 and P_2 and will be tangential to the cylinder.

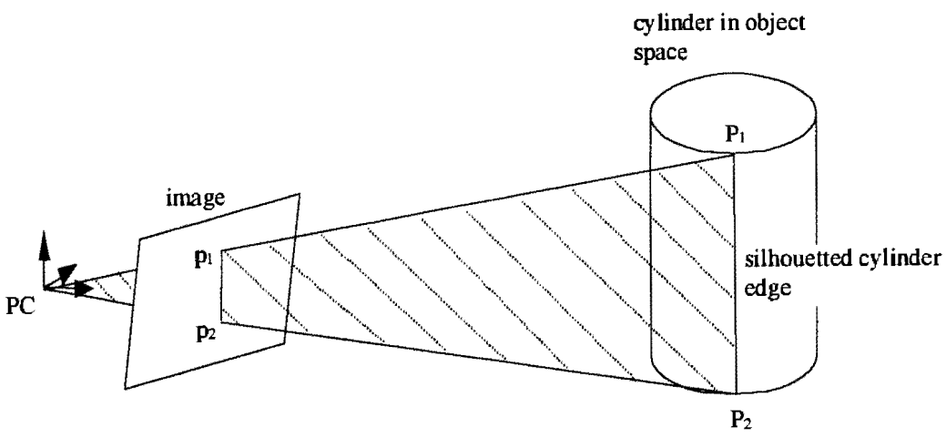

Figure 24 Points p_1,p_2, P_1,P_2 and PC are coplanar

If both silhouette edges of a cylinder are visible in an image then two lines will be projected onto the image. As a result two planes are formed which are tangential to the cylinder and which pass through the image and the PC of the camera. If two images are taken of the cylinder from different camera positions then a pair of planes will originate from each of the two PC points in space and each plane will be

tangential to the cylinder. (In the rest of this thesis such planes will be termed an "edge-plane".) This produces a geometric situation similar to that described in the two dimensional case above and forms the basis of the new technique to determine the parameters of a cylinder that has been photographically captured.

Numerous combinations of edge-planes from two or more camera positions can be used. However, the simplest solution utilises two edge-planes from each of two images (from two different camera positions). This is termed the four-edge-planes method.

5.3 The Four-Edge-Planes (FEP) Method

Before calculations using these methods can be performed, the interior orientation of the camera (or cameras) used must be determined and the exterior orientation of each image must be calculated (see Section 3 for an explanation of the principles of photogrammetry for non photogrammetrists).

This technique also assumes that the parameters defining the lines on the image representing the silhouette edges are known in the image co-ordinate system. It is assumed that the lines are represented using the form given in Equation 39. This form was chosen due to the simplicity with which it can be stored in a computer program. It is also a convenient representation which can be used to find any point which lies on the line. However, any other two dimensional line representation could have been used. A detailed explanation of the techniques used and the process involved in extracting the parameters of these lines accurately from an image is presented in Chapter 6. However, it should be noted here that the parameters of these lines need to be determined on an ideal, undistorted image. Only if this is true will the lines on the image be coplanar with the PC of the camera and the silhouette edge of the cylinder. For this reason the effect of lens and other distortions must be removed from the line parameters. Section 3 explained the effects of these distortions as well as describing how to remove their influence from an image observation. It may be recalled that the

equations in Section 3.1.1 assume that image (metric) co-ordinates, not pixels co-ordinates, be used. As a result, the parameters of the lines are calculated in, and are true only for, image space not pixel space (refer to Figure 7).

The first step in the method is to calculate an edge-plane from one of the edge lines on the image. A plane can be uniquely defined if it is known to pass through three points in object space. The PC of the camera is chosen to be one of these points. Two further points in object space need to be determined to define the plane. As Figure 24 shows, the position in object space of the two image points p_1 and p_2 would be sufficient to define the plane. It is therefore necessary to determine the three dimensional co-ordinates of these points. It should be noted that what are required are the actual object space co-ordinates of these points where they lie on the image, not the object co-ordinates of the points on the features which were projected onto the image.

In order to determine the co-ordinates of p_1 and p_2 in object space, the image co-ordinates of these points must first be determined. The parameters a and b which represent the line on the image can be used to find the co-ordinates of any two image points on the line. In fact, the two points do not have to fall within the dimensions of the real image, rather they merely need to fall on the infinite line which lies in the image plane. The image points can be found by simple substitution of two arbitrary x values into the equation of the form given by Equation 39, which results in the corresponding y values.

Once the two image points have been determined they must be transformed into object space. The perspective transformation given in Equation 49 and shown in Figure 25 describes the transformation of a point in image space into a point in object space. The photo scale factor (λ_i) at an image point is used to indicate the relationship between two distances; the distance from the PC to the point on the image, and the distance from the PC to the point on the feature in object space. Commonly, when determining object co-ordinates photogrammetrically, this value is the only unknown; the image points (x_i, y_i) are observations, while the interior orientation elements

(x_p, y_p, c) and the exterior orientation elements $(X_C, Y_C, Z_C, \theta, \phi, \kappa)$ are known from previous calculations. The scaling factor is the value which needs to be determined when using rays from two images to perform an object point intersection calculation. Once this scaling factor is known, the object co-ordinate (X_i, Y_i, Z_i) can be easily calculated.

However, if these two distances are the same, then the scaling factor can be chosen to be unity and the point in object space that is calculated will be the co-ordinate in object space of the point on the imaging media itself.

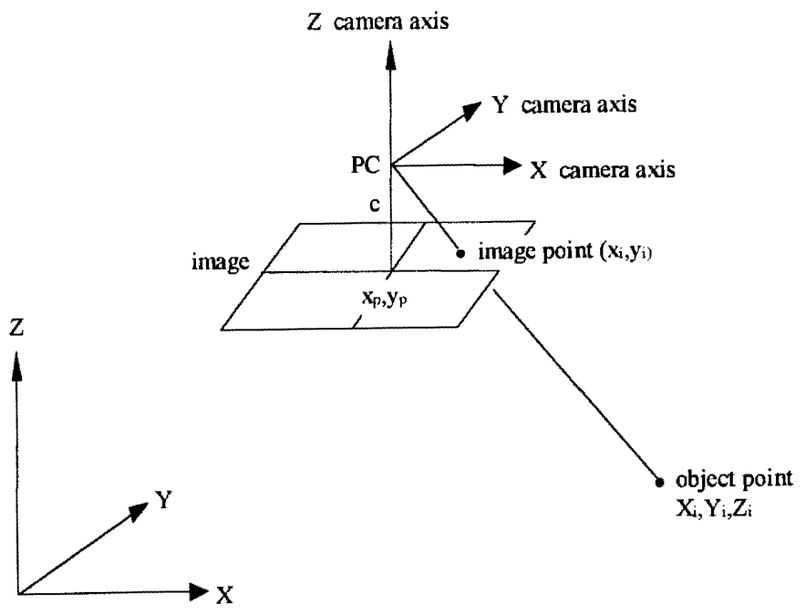

Figure 25 The projection of an object point onto an image

The perspective transformation equations are

$$X_i - X_C = \lambda_i \left[m_{11}(x_i - x_p) + m_{21}(y_i - y_p) + m_{31} c \right]$$

$$Y_i - Y_C = \lambda_i \left[m_{12}(x_i - x_p) + m_{22}(y_i - y_p) + m_{32} c \right]$$

$$Z_i - Z_C = \lambda_i \left[m_{13}(x_i - x_p) + m_{23}(y_i - y_p) + m_{33} c \right]$$

Equation 49

where:

$$
\begin{aligned}
m_{11} &= \cos\phi\cos\kappa \\
m_{12} &= \cos\omega\sin\kappa + \sin\omega\sin\phi\cos\kappa \\
m_{13} &= \sin\omega\sin\kappa - \cos\omega\sin\phi\cos\kappa \\
m_{21} &= -\cos\phi\sin\kappa \\
m_{22} &= \cos\omega\cos\kappa - \sin\omega\sin\phi\sin\kappa \\
m_{23} &= \sin\omega\cos\kappa + \cos\omega\sin\phi\sin\kappa \\
m_{31} &= \sin\phi \\
m_{32} &= -\sin\omega\cos\phi \\
m_{33} &= \cos\omega\cos\phi
\end{aligned}
$$

Equation 50

and where:

X_i, Y_i, Z_i	is the co-ordinate of point *i* transformed into object space
x_i, y_i	is the image co-ordinates of the point *i*
X_c, Y_c, Z_c	is the co-ordinate of the PC of the camera
λ_i	is the photo scale factor at the image point *i*
m_{ij}	are the elements of the rotation matrix transforming from object to image space
ω, ϕ, κ	are rotations about the x,y,z camera axes respectively, positive in the counter clockwise direction
x_p, y_p	is the image space co-ordinate of the principal point of the image
c	is the principal distance of the camera

It should be noted that the rotation matrix given in Equation 50 is the inverse of that given in Equation 3. The rotation matrix used in Equation 3 transforms from object to image space, whilst that given above transforms from image to object space.

If the photo scale factor in Equation 49 is set to unity, then the object co-ordinate being calculated will fall on the image plane. In other words, the object space co-ordinate of the image point will be determined. By substituting the image co-ordinates of the two points that were calculated on the image line into the equations in Equation 49, two object points are calculated. These two object points, together with the co-ordinate of the PC can be used to form a plane in object space.

A plane may be defined by the four parameters A,B,C,D using the relationship:

$$Ax + By + Cz + D = 0$$

Equation 51

The values of the parameters defining the plane which passes through three known points $P(x_p,y_p,z_p), Q(x_q,y_q,z_q), R(x_r,y_r,z_r)$ can be found by forming the vectors PQ and PR.

$$PQ = (x_q - x_p, y_q - y_p, z_q - z_p)$$
$$PR = (x_r - x_p, y_r - y_p, z_r - z_p)$$

Equation 52

The cross product of the two vectors formed in Equation 52 is normal to the desired plane. From this the values of the defining parameters of the planes can be determined from:

$$A = (y_q - y_p)(z_r - z_p) - (z_q - z_p)(y_r - y_p)$$
$$B = (z_q - z_p)(x_r - x_p) - (x_q - x_p)(z_r - z_p)$$
$$C = (x_q - x_p)(y_r - y_p) - (y_q - y_p)(x_r - x_p)$$
$$D = -Ax_p - By_p - Cz_p$$

Equation 53

The edge-plane formed, as described earlier in this chapter, passes through the PC of the camera and the line representing a silhouette edge of the cylinder on the image. This plane is tangential to the cylinder.

If a second silhouette edge of the same cylinder is visible on the image, then a second edge-plane to that silhouette edge can be formed (refer to Figure 26).

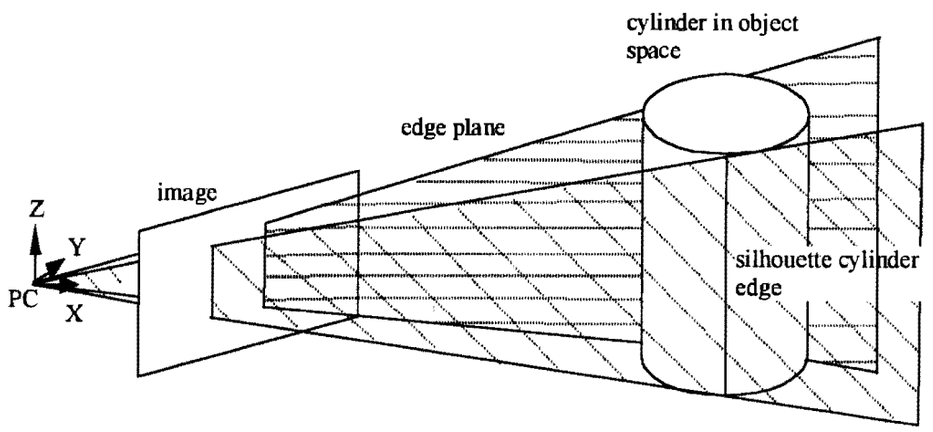

Figure 26 Two edge-planes formed from a single image

The PC of the camera lies on the line formed by the intersection of the two edge-planes. The planes which form the angular bisector of these two edge-planes will also pass through the PC. The intersection of the two edge-planes forms both an acute and an obtuse angle. As a result two bisecting planes will be calculated; one which bisects the acute angle between the two edge-planes and the other which bisects the obtuse angle.

The parameters of a plane which bisects the angles between two planes can be determined using the knowledge that any point on the new plane must be equidistant to the original planes:

$$\frac{A_1x+B_1y+C_1z+D_1}{\sqrt{A_1^2+B_1^2+C_1^2}}=\pm\frac{A_2x+B_2y+C_2z+D_2}{\sqrt{A_2^2+B_2^2+C_2^2}}$$

Equation 54

where:

A_1, B_1, C_1, D_1 are the parameters of the first edge-plane

A_2, B_2, C_2, D_2 are the parameters of the second edge-plane

x,y,z is the co-ordinate of a point on the plane bisecting the edge-planes

From Equation 54 the parameters of the two bisecting planes can be determined from:

$$\begin{aligned}
A_3 &= (T_2A_1+T_1A_2)\\
B_3 &= (T_2B_1+T_1B_2)\\
C_3 &= (T_2C_1+T_1C_2)\\
D_3 &= (T_2D_1+T_1D_2)\\
A_4 &= (T_2A_1-T_1A_2)\\
B_4 &= (T_2B_1-T_1B_2)\\
C_4 &= (T_2C_1-T_1C_2)\\
D_4 &= (T_2D_1-T_1D_2)
\end{aligned}$$

in which:

$$\begin{aligned}
T_1 &= \sqrt{A_1^2+B_1^2+C_1^2}\\
T_2 &= \sqrt{A_2^2+B_2^2+C_2^2}
\end{aligned}$$

Equation 55

where:

A_3, B_3, C_3, D_3 and A_4, B_4, C_4, D_4 are the parameters of the two bisecting planes.

In the rest of this thesis a bisecting plane such as those calculated above will be called an "edge bisector plane". While both of the planes determined pass through the PC of the camera, only one passes through the longitudinal axis of the cylinder.

It can be assumed that the angle formed between the two edge-planes and which is "between" the PC and the cylinder, will be acute as indicated in Figure 27.

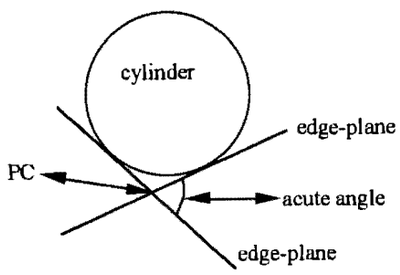

An obtuse angle falls "between" the PC and cylinder

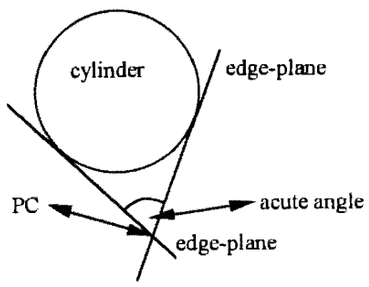

An acute angle falls "between" the PC and cylinder

Figure 27 The figure shows the two possible positions of the acute angle between the two edge-planes with respect to the cylinder and the PC

As Figure 28 shows, this assumption is true provided the PC is no closer than 0.4 times the cylinder radius from the surface of the cylinder.

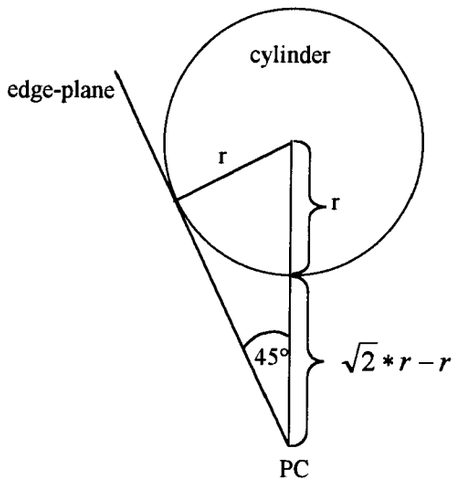

Figure 28 The determination of the closest distance between the perspective centre and the cylinder surface under which the described cylinder measurement technique is applicable

To ensure that the chosen edge bisector plane passes through the cylinder, the edge bisector plane which bisects the acute angle between the two edge-planes must be selected. From a practical (i.e. programming) perspective this is perhaps most easily accomplished by initially determining both possible edge bisector planes. Then clearly, the desired edge bisector plane will form an angle of less than 45° with either of the two edge-planes. It is simple to determine which of the edge bisector planes conforms to this criteria using the following equation:

$$\theta = \cos^{-1}\left|\frac{A_1A_2 + B_1B_2 + C_1C_2}{\sqrt{A_1^2 + B_1^2 + C_1^2} * \sqrt{A_2^2 + B_2^2 + C_2^2}}\right|$$

Equation 56

where:

θ is the angle between two planes

A_1,B_1,C_1,A_2,B_2,C_2 are the parameters representing two planes.

A second image of the cylinder is captured from another camera position. Two more edge-planes can be created from that image and an edge bisector plane bisecting the acute angle between these two edge-planes can be found.

Each image has one edge bisector plane passing through the longitudinal axis of the cylinder, as can be seen in Figure 29. In the same way to that of the two dimensional case (refer to Figure 23) explained earlier in the chapter, the longitudinal axis of the cylinder will lie in both of the two edge bisector planes. The position and direction of the longitudinal axis of the cylinder in space is defined by the intersection of these two planes. The method by which the radius of the cylinder may be calculated is described later in Section 5.5.

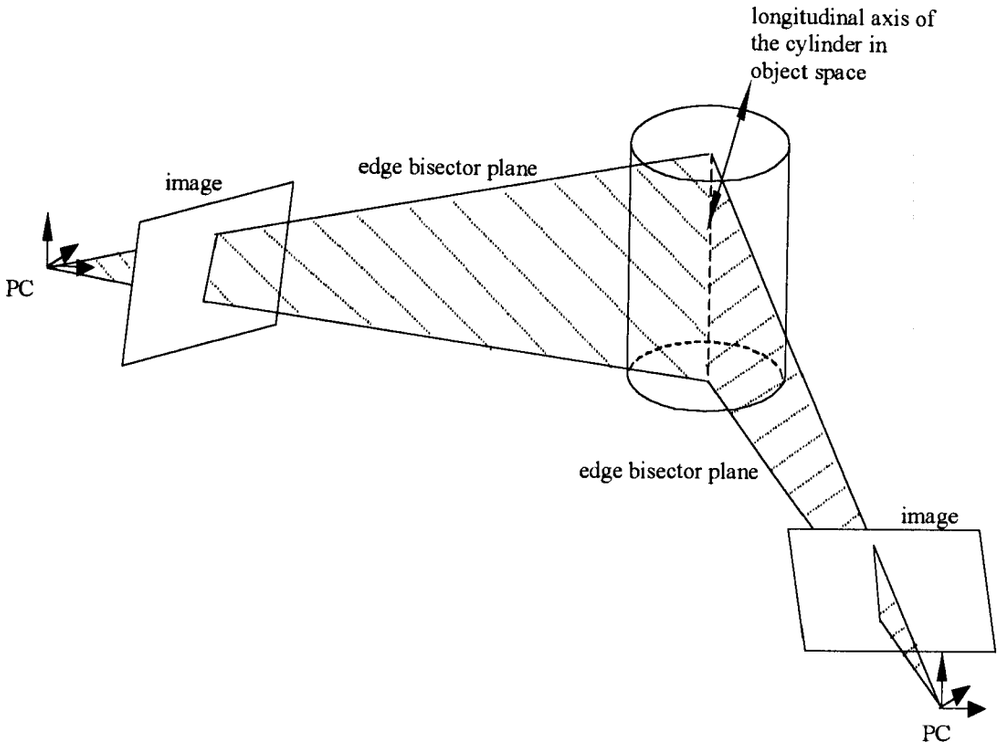

Figure 29 The longitudinal axis of a cylinder in object space defined by the intersection of two edge bisector planes

It should be noted that the two bisecting planes will define the cylinder's axis uniquely under most circumstances. The exception however, is when the two bisecting planes coincide. This will occur if the longitudinal axis of the cylinder and the two PCs all fall on the same plane. Care needs to be taken to ensure that this does not occur. Furthermore, the angular separation of the two bisecting planes has an effect on the accuracy of the method. This is discussed in Chapters 7 and 8.

5.4 Further Silhouette-Edge Methods

As was mentioned earlier in the chapter, a variety of combinations of camera positions and edge-planes can occur since it is not always possible to ensure that two edge-planes are visible from every camera position. This may occur because the view of the cylinder is partially occluded by other objects falling between the camera and the cylinder. This is especially likely in cluttered working environments. Poor lighting can also make one of the edges of the cylinder indistinct on the image, either through making one side of the cylinder too bright or by casting it in shadow. For these reasons it is necessary to expand the previously described technique to calculate cylindrical parameters from two more basic combinations:

1. The three-edge-planes method, and
2. The three-separate-edge-planes method.

Analysis of the effectiveness of these methods as well as the previously mentioned method is discussed in Chapters 7 and 8.

5.4.1 The Three-Edge-Planes (TEP) Method

This method is a modification of the four-edge-planes (FEP) method and like that method uses images captured from two camera positions. The method differs from that previously described in that while one of the images contains two silhouette edges, only one edge is visible from the second camera position. This method also differs from the FEP method in that it does not determine a unique solution for the cylinder's position and orientation.

As in the case of the FEP method, the images are assumed to be oriented and the parameters of the edge lines on the image known. The parameters of the edge-planes from the lines on the two images may be calculated in the same way as was done in Section 5.3 (refer to Equation 49-Equation 53). Figure 30 shows the resulting situation in a plan view.

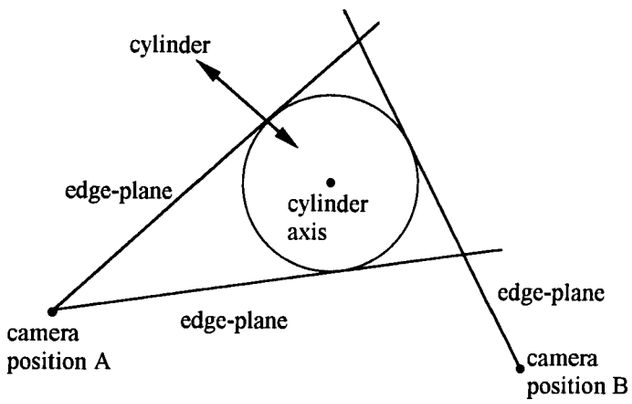

Figure 30 Plan view of the TEP scenario

Proceeding as in the FEP method, the edge bisector plane originating from camera position A can be determined using the equations described by Equation 54-Equation 56. The edge bisector from camera position A defines the plane along which the cylinder axis is known to lie. It is not possible however to create an edge bisector plane originating from camera position B since only one edge-plane is available. A situation as indicated in Figure 31 now exists in which the cylinder axis may lie on either side of the edge-plane originating from camera position B.

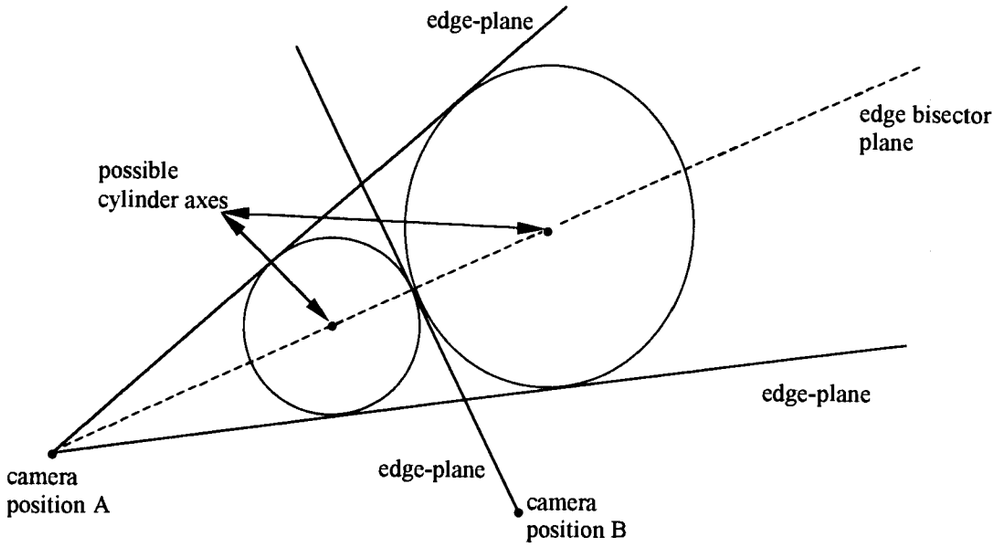

Figure 31 Since only one edge-plane originates from camera position B, no edge bisector plane can be created originating from this camera position

In order to determine the two possible positions of the cylinder axis, a line on which a "virtual" camera station would fall can be created. This line is formed from the intersection of the edge-plane originating from camera position B and either of the two edge-planes from camera position *A*. This line is shown by the point *B'* in Figure 32, which is once again a plan view. The term "virtual" camera station describes the fact that further calculations will proceed as if an image had been captured by a camera whose position fell on the line described by the point *B'*. In the same way that two edge-planes from the cylinder pass through *A*, two edge-planes also pass through the "virtual" camera PC at *B*.

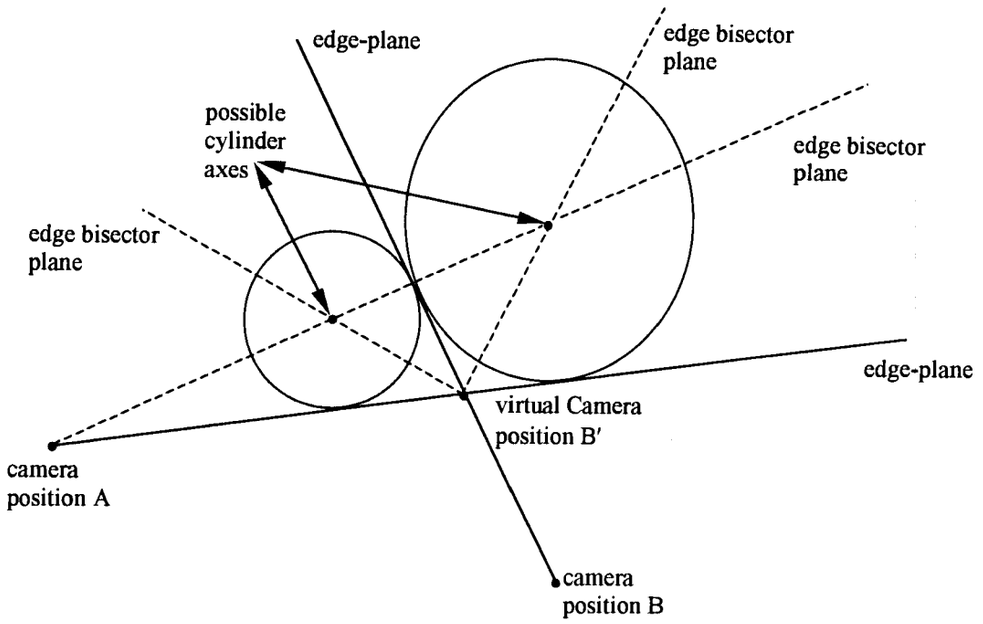

Figure 32 Plan view indicating the two possible cylinder axes found using the TEP method

Thus a situation identical to that discussed in the FEP method now exists whereby the two possible axes of the cylinder are described by the intersection of two planes. It is not possible to automatically determine which of the two axes defines the true cylinder axis. A practical solution will be described in the following section.

5.4.2 Practical Considerations to Implementing the Method

If this method is implemented in an interactive program, the problem of selecting the true axis from the two possible axes can be overcome. Input can be obtained from the user either before the axes are calculated and the correct axis then chosen automatically, or the two possible axes can be calculated and displayed overlaying the image on the screen and the user then given the option of choosing the correct axis. The latter option is less complicated and simply involves back projecting the axes lines in object space into the images. The user can then by inspection select whichever axis lies on the true axis of the cylinder. Given the speed at which the calculations can be performed on a personal computer this is no less convenient than the first option.

The axes lines in object space can be back projected onto the images by determining any two points on the axis in object space and finding the corresponding image co-ordinates for points using the collinearity equations as given in Equation 1 and Equation 2. The two points projected onto the image can then be joined to represent a possible axis line.

An important consideration when determining the image co-ordinates is the effect of the additional distortion parameters. It is likely that if the object points chosen to define the line in space are chosen arbitrarily, they will not fall within the field of view of the camera. However, it is computationally more expensive to ensure that the chosen object space points fall within the field of view of the camera. Although arbitrarily chosen object points would project onto the same plane as the image, they would not necessarily project onto the image itself. It is important to recall that the additional parameters apply *only* to co-ordinates measured on the image; the effect of additional parameters cannot be extrapolated. If the additional parameters are applied to points which fall on the plane of the image, but not on the image itself, large, erroneous corrections will be applied to the resulting co-ordinates. As a result the cylinder axis will not be correctly displayed on the image. The simplest solution to this problem is simply not to apply the additional parameters when determining the image co-ordinates. Although this is strictly incorrect from a photogrammetric perspective, the resultant lines shown on the image are sufficiently accurate to allow the selection of the correct axis.

It is also possible to use *a priori* information about the expected approximate parameters of the cylinder, such as the radius value or object points the cylinder axis is expected to pass through. This will reduce the number of possible axes presented to the user for selection.

5.4.3 The Three-Separate-Edge-Planes (TSEP) Method

A further common situation is that in which three images are available, each containing only one silhouette edge. Unlike the TEP method (refer to Section 5.3) or the FEP method (refer to Section 5.4.1), there are no edge bisector planes which can be directly formed from one of the camera stations. The edge-planes formed from each camera station may (from a mathematical perspective) be tangential to either side of the cylinder. As a result, the complexity of the solution is increased, however, the correct cylinder parameters can still be found in ways similar to the previous two methods.

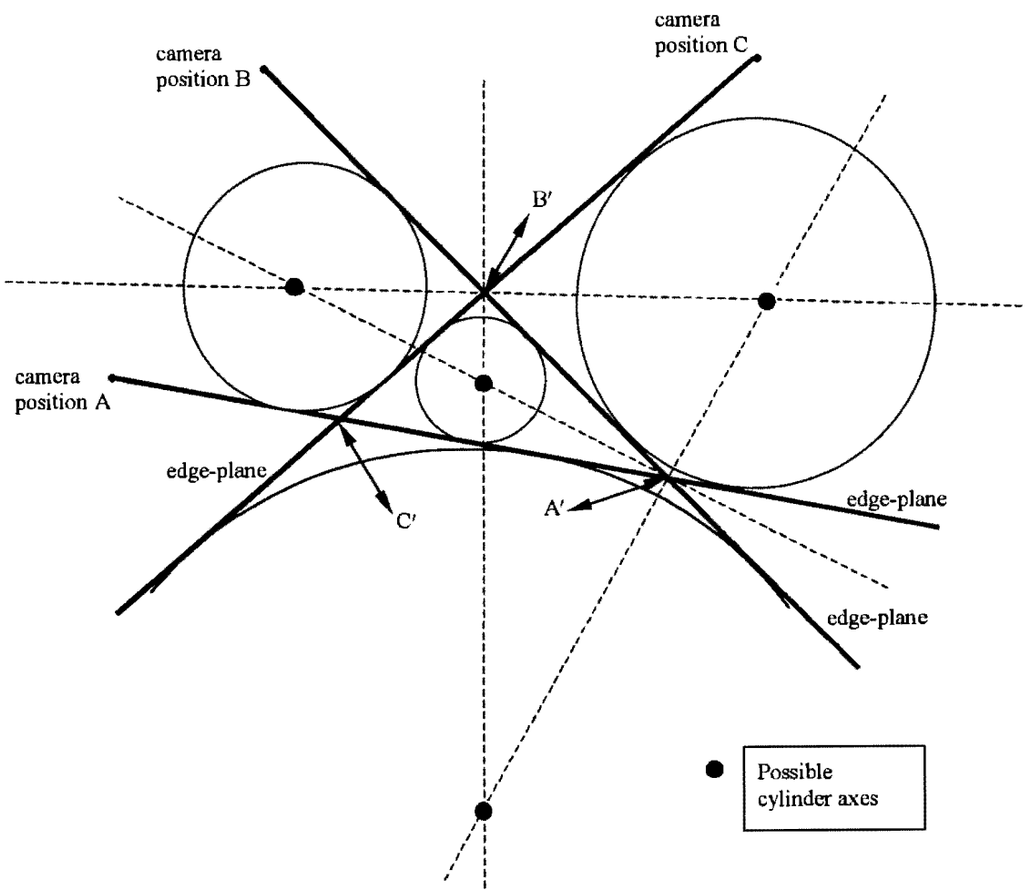

Figure 33 The four possible cylinder axes found using the TSEP method

Figure 33 graphically shows the solution used in this method. As the figure shows, it is not possible to create an edge bisector plane from any camera station. However,

"virtual" camera positions can be found in exactly the same way as in the TEP method. Virtual camera position A' is formed where the edge-planes from camera positions A and B intersect. Virtual camera position B' is formed where the edge-planes from camera positions B and C intersect. A further virtual camera position can be formed at C' by edge-planes from the camera positions A and C. However, only two virtual camera positions are required in order to determine the possible cylinder axes and any two of the three virtual camera positions will suffice. Two edge bisector planes can then be formed at each of these virtual camera positions. The intersection of any of two edge bisector planes provides the mathematically correct position of a cylinder to which the edge-planes from all three images are tangential. Again, only one of these represents the true axis of the cylinder captured on the images. As in the previous method it is a simple task to use back projection to allow the user to indicate which is the true axis.

5.4.4 Towards the Use of Redundant Observations

The TSEP method may be extended to use a greater number of edge-planes than the minimum of three which is required to solve for the parameters of the cylinder. "Virtual" camera positions are formed in the same way to that described by the previous methods. Each "virtual" camera position produces two edge bisector planes and it is again the intersection of these planes which define possible axis positions. The number of possible axes increases greatly with each camera position which is added. Whilst there are four possible axes produced from three edge-planes from three camera positions, there are ten possible axes produced from four edge-planes from four camera positions. However, one of the two edge bisector planes produced at each virtual camera position will pass through the true cylinder axis. As a result, the true axis can be identified from the set of possible axes as the possible axis through which the most number of edge bisector planes pass.

A practical suggestion to determining the correct axis is to project all the edge bisector planes onto a plane (for the purpose of clarity we will term this the "projection plane"). A simplified example is shown in Figure 34. In reality there would be many more edge bisector planes and consequently numerous lines (we will call them edge bisector lines) would be projected onto the projection plane.

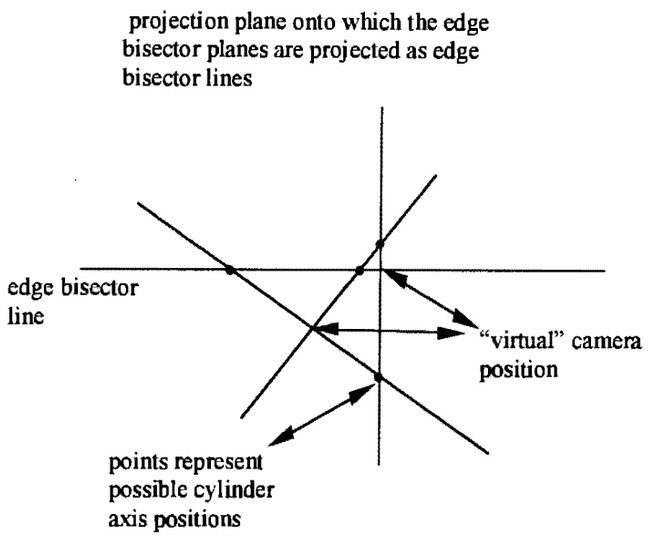

Figure 34 Edge bisector planes can be projected onto a plane, thereby producing edge bisector lines on the projection plane

Theoretically each possible axis will be represented by the perfect intersection of a number of these lines. As was previously stated, the true axis will be represented by the intersection point at which the greatest number of lines intersect since this is the only point through which one edge bisector line from every camera station must pass. However, because of the redundancy in the observations it is unlikely that each possible axis will be formed by the perfect intersection of the edge bisector lines describing it. Instead, each possible axis will be surrounded by numerous points, each representing the intersection of two edge bisector lines on the projection plane (and two edge bisector planes in space). The true cylinder axis will be found in the region of the plane with the highest density of these points (refer to Figure 35). It would be possible to utilise some form of cluster detection algorithm to detect this region on the plane. The approximate position of the true axis will then be known and the correct

edge bisector planes from each "virtual" camera position selected. The line best representing the cylinder axis can then be calculated by means of a least squares best fit of the edge bisector planes from each "virtual" camera position (see Hill, 1998 for a description of an algorithm to determine a line in space from the least squares best fit of intersecting planes).

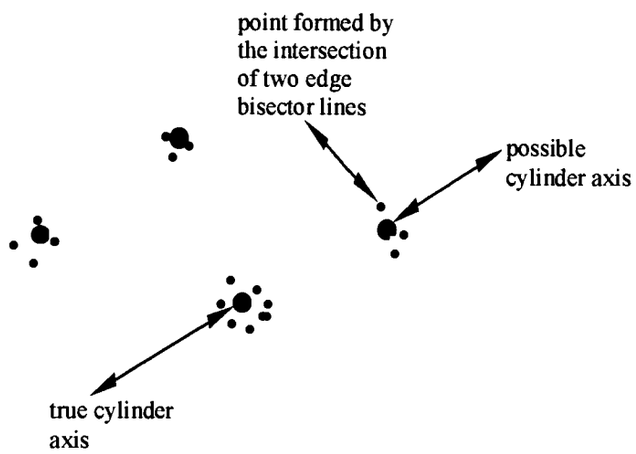

Figure 35 The true axis is surrounded by the most points representing the intersection of edge lines

5.5 Calculating the Radius of a Cylinder

The radius of the cylinder is the final cylinder parameter that needs to be calculated and can only be calculated once the other defining parameters (the position and direction of the longitudinal axis of the cylinder in object space) are known. The technique for calculating the radius is the same no matter which method in Sections 5.3 or 5.4 are used.

Under ideal situations the calculation of the radius is simple. The line defining the axis of the cylinder is already known and the edge-planes that have previously been calculated are all known to be tangential to the cylinder (refer to Figure 30). A simple calculation would then be sufficient to determine the orthogonal distance (i.e. the shortest distance) between the line in space and the edge-plane tangential to the cylinder.

However, unavoidable inaccuracies will be present in both the definition of the cylinder axis as well as in the definition of the edge-planes. These will arise from inaccuracies in the observations which lead to the definition of the parameters defining the silhouette edge lines on the images, and to a lesser extent, rounding errors associated with the calculations. As a result of these inaccuracies it cannot be guaranteed that the calculated cylinder axis and the edge-planes will be truly parallel in object space. Consequently the cylinder axis is likely to intersect the various edge-planes at some point in space. Any calculation which determines the radius of the cylinder by merely calculating the distance between the axis and edge-plane, is likely to determine the radius to be zero.

It must be recognised that this limitation only occurs because neither the definition of the axis line nor the edge-planes restrict the extension of the features; both the line and the planes have infinite length and area respectively. It is this infinite extension of the edge-planes and axis line which ensures that any slight errors in their definition eventually results in them intersecting.

Some geometric methods which, appear simpler than the one presented below, have been investigated. However, only the one presented can reliably ensure that an accurate radius value is calculated.

Within the confines of the section of object space visible in an image used to create an edge-plane, the assumption that the edge-planes and the cylinder axis are parallel is effectively true; any deviation from the ideal positions is, in this context, negligible. Figure 36 shows this section of object space as that which is bounded by the rays *A,B,C,D* (the field of view represented by the four corners of the image) and the PC. It is appropriate to measure the distance only between those parts of the edge-plane and cylinder axis which fall within this field of view of the camera.

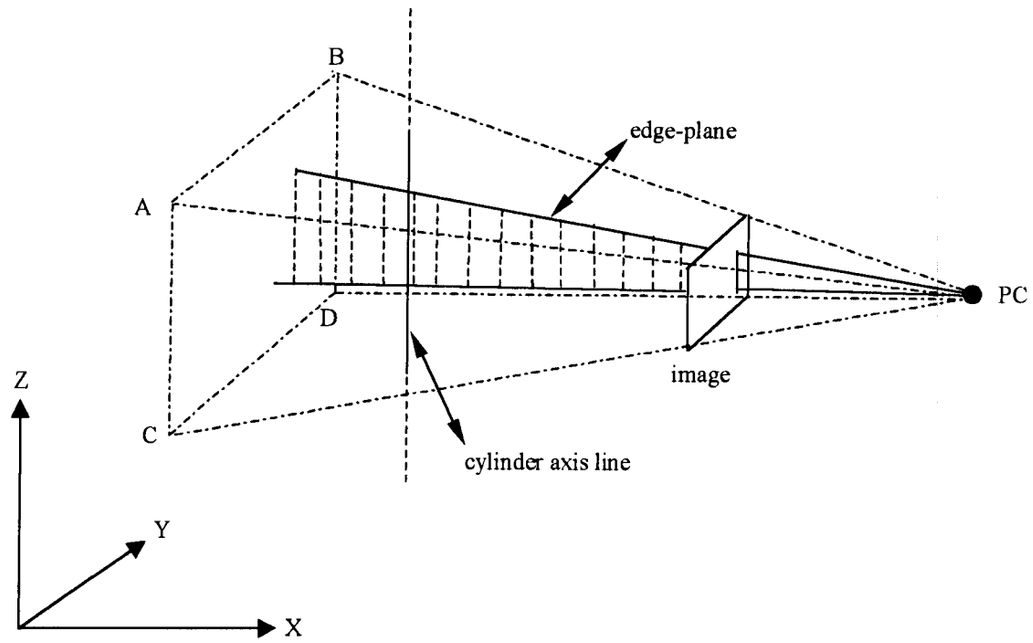

Figure 36 Only the sections of cylinder axis and edge-plane which fall within the field of view of the camera should be used to calculate the cylinder radius.

One way to ensure that only those parts of the axis and edge-plane which fall within the field of view of the camera are used for the radius calculation, is to slightly alter the approach to the method by which the radius is calculated. Instead of determining the shortest distance between the axis and the edge-plane, the distance between the axis and a specific line lying on the edge-plane can instead be calculated. The line can be chosen as a ray which passes through the PC of the camera and the edge line on the image. This ensures that the line will lie on the part of the edge-plane which falls within the field of view. The line is defined by the co-ordinate of the PC and the co-ordinate, in object space, of a point on the line in the image.

If only the parameters of the edge line are available, Equation 57 can be used to determine the image co-ordinate of a point on the edge line which is closest to the origin of the image co-ordinate system. This ensures that the image co-ordinate formed does indeed lie within the bounds of the true image.

$$x_L = \frac{-ab}{a^2+1}$$
$$y_L = -\frac{1}{a}x_L$$

Equation 57

where:

a, b are the parameters of the edge line

x_L, y_L is the co-ordinate of the point L on the edge line closest to the origin of the image co-ordinate system

The object co-ordinate of the image point L (x_L, y_L) is found using Equation 49. This object point, together with the co-ordinate of the PC, forms a line in object space. The line may be defined by a vector joining the two points PC and L.

As was mentioned previously in this chapter, the cylinder axis is defined by two edge bisector planes. Two points (P and Q) lying on the cylinder axis may be calculated by selecting two arbitrary X ordinate values and solving Equation 58 for each of P and Q in turn. It should be noted that if the cylinder axis is parallel to the Y or Z co-ordinate system axes, it will be necessary to instead select arbitrary Y or Z ordinate values.

$$\begin{vmatrix} Y \\ Z \end{vmatrix} = \begin{vmatrix} B_1 & C_1 \\ B_2 & C_2 \end{vmatrix}^{-1} \begin{vmatrix} -D_1 - A_1 X \\ -D_2 - A_2 X \end{vmatrix}$$

Equation 58

where:

A_1, B_1, C_1, D_1 and A_2, B_2, C_2, D_2 are the parameters of the two edge-planes

The axis line may then be defined by the vector joining P and Q.

The shortest distance between the two vectors $P.Q$ and $PC.L$ may then be found from:

$$D = \frac{1}{\|PC.L \times P.Q\|} |(PC.L \times P.Q) \bullet PC.Q|$$

Equation 59

where:

$PC.L$ and $P.Q$	are the two vectors described in the text above
$PC.Q$	is a vector between the PC and the point Q calculated on the cylinder axis
D	is the distance between the two line defined by the vectors $PC.L$ and $P.Q$

The distance D is the approximate radius of the cylinder. A distance may be calculated using each image edge line available and the mean of these taken to produce a final value for the radius of the cylinder.

This provides the last parameter needed to define a cylinder in space.

Test results obtained using the methods described in this chapter are presented in Chapters 7 and 8.

6 EDGE DETECTION AND LINE EXTRACTION

The discussion of the cylinder parameter determination methods described in Chapter 5 assumed that the parameters defining the lines representing the cylinders silhouette edges on the images are known. Before calculations to determine the cylinder parameters may begin these parameters need to be determined from the image. This chapter explains some of the techniques which can be used to determine the parameters of these lines. As with Chapter 3, some of the information provided here may be commonly known to digital photogrammetrists, however, it is provided for the benefit of non-experts.

The human brain interprets its surroundings in a complex way. Cameras using conventional film produce images of a scene with a near continuous tone and which have a similar appearance to how the human brain and eyes would view the same scene. Since analogue images have a near continuous tone they may often be magnified without any significant loss of quality. Although the individual grains of the film emulsion will eventually become visible, this only occurs after considerable magnification. As a result of this property, a human operator using powerful magnification and analogue images could easily and accurately mark the silhouette edges of a cylinder.

However, a continuous tone image captured using an analogue camera has very different properties to that of a digital image. A digital image may be produced either by scanning an analogue image, capturing an image using a frame grabber and a CCD (Charge Coupled Device) video camera or through the use of a still digital video camera such as the Kodak DCS420 used in this thesis. In all cases however, the resultant digital image has the same form.

The information which defines a digital image is quantized[1] both spatially and radiometrically. Whereas an analogue image has a continuous tone, digital images consist of discrete, small finite picture elements (pixels). An image consists of an array of pixels each containing a quantized grey value (or a colour value in the case of colour images). This value relates to the amount of light that fell onto a part of the imaging medium assigned to this pixel and it is the variation in these values across an image which produces a recognisable picture of the scene captured. It is most often not possible to magnify a digital image to the same degree as an analogue image while still retaining usable image quality. The maximum usable magnification of a digital image is limited by the resolution at which the image was originally captured. This may prevent the operator from magnifying the image sufficiently to be able to accurately identify the cylinder's silhouette edges on the image. In any case it is desirable to reduce the amount of operator interaction. Methods which semi-automatically identify edges in digital images and can then extract information about those edges more accurately than an operator could have done, have been developed (Haralick and Shapiro, 1992).

The determination of the parameters of the silhouette edge lines can be divided into two steps.

1. Identifying possible edge pixels in the image
2. Selecting those edge pixels which form the desired silhouette edge line and determining the parameters of that line

The first step can be accomplished through the use of edge detection filters which are applied to the image. The second step involves the use of line extraction techniques to select the desired line.

[1]In the context of this thesis, the term "quantized" is taken to mean "divided up into equal sub-ranges within an overall range".

6.1 Edge Detection Algorithms

An ideal edge in a digital image is represented by a discontinuous change of grey level intensities between two adjacent pixels. Some forms of ideal edges are shown in Figure 37.

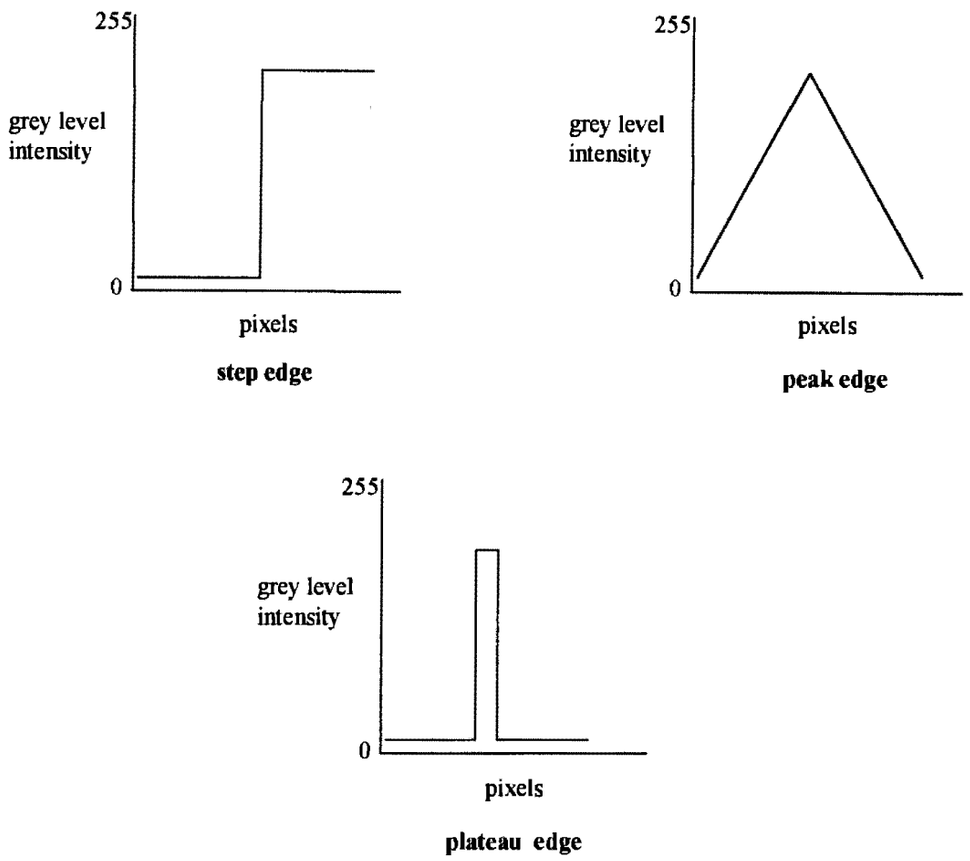

Figure 37 Some common forms of ideal edges

Any edge detection technique must attempt to reduce the amount of information presented in an image to that which is relevant only to edges. All the techniques presented in this section accomplish this by testing each pixel in the image to determine to what extent it conforms to the characteristics of an edge pixel. At each pixel a value or values representing edge "strength" are calculated. The value at each pixel relative to the other pixels in the image can be judged and only the pixels above a given threshold are selected as edge pixels.

In the following sections the maximum gradient, Sobel, and Canny filters are presented. These three filters all locate an edge to single pixel accuracy. In order to determine the position of an edge to sub-pixel accuracy, the technique of sub-pixel edge location by means of moment preserving may be used. This technique is also described below.

6.1.1 Maximum Gradient Filter

The maximum gradient filter is one of the simpler edge detection filters that can be applied to an image. The filter is based on the characteristic that the grey intensities at an edge change noticeably. The gradient in a 3x3 pixel neighbourhood around the central pixel of interest is found in each of four directions by means of the following equation:

$$gradient = \frac{greyvalue_j - greyvalue_i}{2}$$

Equation 60

where the combinations of (i,j) are (4,6) (1,9) (2,8) (3,7) and correspond to the pixel labels as indicated in Figure 38.

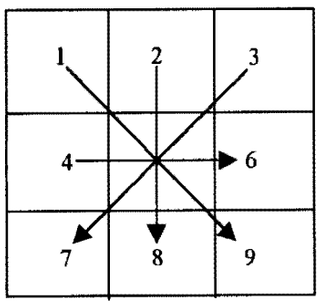

Figure 38 Gradient directions for the maximum gradient filter

The maximum of the four gradients is then selected as the measure of edge strength at the pixel of interest and stored in an array to later produce a gradient image. Pixels in the gradient image with high maximum gradient values are more likely to be edge pixels. The edge direction, to the closest multiple of 45°, can be determined at the pixel of interest from the direction of its maximum gradient.

6.1.2 Sobel Filter

The maximum gradient method pays equal attention to the gradients in the diagonal neighbourhood of the pixel of interest as it does to those in the horizontal and vertical neighbourhoods. The Sobel filter on the other hand, gives greater weight to those pixels in the horizontal and vertical neighbourhoods of the central pixel of interest.

Two gradient values, G_x and G_y, are produced by applying the masks shown in Figure 39 in the x-direction and the y-direction respectively at the pixel of interest.

-1	0	1
-2	0	2
-1	0	1

-1	-2	-1
0	0	0
1	2	1

Figure 39 The Sobel mask applied at the pixel of interest to calculate G_x and G_y

For each pixel of interest, both of the gradient values are stored to later produce gradient images in the horizontal and vertical directions. As with the maximum gradient method, pixels with higher maximum gradient values are more likely to be edge pixels. The edge direction can be determined from the horizontal and vertical gradient values.

6.1.3 Canny Operator

A property of edge detection filters is that they have the tendency to identify very localised points as possible edges. The two previous filters are both applied to a 3x3 pixel neighbourhood. As a result it is possible for noise in the image to cause certain pixels to be given a high gradient value despite these points not being true edge pixels. One way to over come this is to utilise a wider mask at each pixel of interest. As a result, more grey values are included in the calculation, so the effect that any single pixel containing noise has on the calculation is reduced. A further way to reduce the effect of image noise is to pass a smoothing filter over the pixels before gradient calculations are performed, thereby reducing the effect that pixels with "outlier" grey levels have on the gradient calculations.

The interest operator developed by Canny (1986) combines both the gradient and smoothing functions into one operator. The smoothing aspect of the operator is provided by Gaussian smoothing. The interest operator is given by the first derivative of the Gaussian and is convolved across the image in the vertical and horizontal directions separately. The Gaussian function in one dimension is given by:

$$G(x) = \frac{1}{\sqrt{2\pi\sigma}} e^{\frac{-x^2}{2\sigma^2}}$$

Equation 61

The first derivative of the Gaussian is:

$$\frac{\partial G}{\partial x}(x) = \frac{-x}{\sigma^2} G(x)$$

Equation 62

in which:

σ is the shaping parameter of the Gaussian function

x is the one dimensional pixel location relative to the pixel of interest

Figure 40 shows the relationship between the Gaussian function and its first derivative.

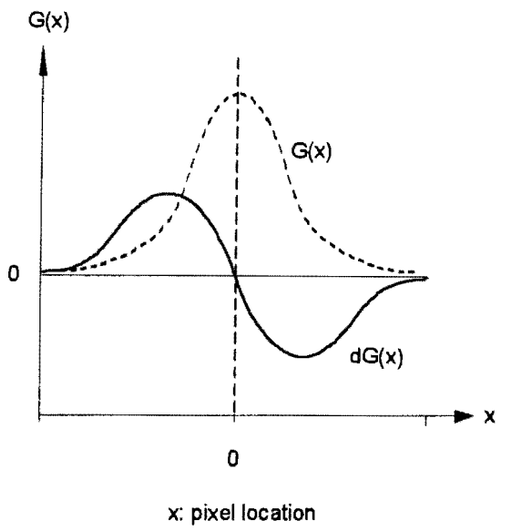

Figure 40 The Gaussian and the first derivative of the Gaussian

The Canny operator given in Equation 62 is convolved vertically and horizontally with the image. As was stated earlier, the grey levels of a number of pixels on either side of the pixel of interest are involved in the calculation. The size of the convolution mask is determined by the magnitude of the shaping parameter σ. As σ is increased the size of the mask increases. The size of the mask for any given σ can be determined as the next odd number above w, the value calculated from the following equation:

$$w = 3 * 2\sqrt{2} * \sigma$$

Equation 63

By increasing the size of the convolution mask as a function of σ, the amount of Gaussian smoothing is increased. This reduces the effect that any single pixel, including those containing noise, has on the final convolution value produced by Equation 62, while at the same time retaining the effect of the trend in grey levels in the vicinity of the pixel of interest. The selection of σ therefore affects the ability of the Canny operator to effectively detect edges in an image. The optimum σ value needs to be determined for each image individually, however, values between 1 and 1.5 were found to be suitable for the images processed in this thesis.

The value of each element of the convolution mask is determined using Equation 62 where x is the mask element relative to the central element (x=0) which is always placed over the pixel of interest. The image is then convolved with this mask in both horizontal and vertical directions forming two gradient images. A large positive or large negative convolution value at a pixel of interest, relative to the convolutions values of other pixels, indicates a strong possibility of an edge pixel existing at the central pixel. As with the Sobel method mentioned in the previous section, the edge direction can be determined from the horizontal and vertical convolution values.

6.1.4 Thresholding of Gradient Arrays

In all three of the edge detection methods presented above, gradient or convolution values are determined at each pixel in the image. These values are then stored in an array; a gradient image or convolution array. In the case of edge detection methods which produce both vertical and horizontal convolutions, two arrays, one for each direction, are created. In order to produce an image or array of pixels which are most likely to be edge pixels, the gradient image arrays must be thresholded to extract the pixels most likely to be those of edges.

The author found it convenient to use a two step process. The pixels which are most likely to be edge pixels are those which have the highest gradient value. In the case of convolution values obtained from the Canny operator, the absolute values at each pixel should be evaluated. An array is formed by combining the arrays containing the

convolution values in the horizontal and vertical directions. The value of each element in this array is chosen to be the greater of the two convolutions, horizontal and vertical, at that pixel. An initial threshold value is then chosen below which it is unlikely that any true edge pixels exist. This is demonstrated in Figure 41. It is convenient to determine this threshold value as a percentage of the highest convolution value in the array; the percent value may be pre-set in the software. Only pixels with values above this threshold will be presented to the operator as possible edge pixels.

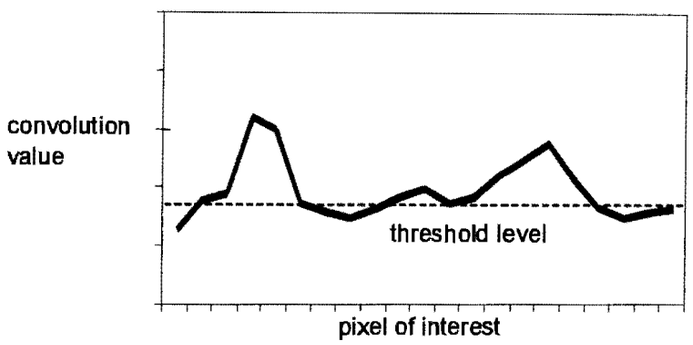

Figure 41 Selection of pixels above a threshold value

The convolution values of these remaining possible edge pixels are then quantized into a fixed number of sets. The range of each set is determined by dividing the difference between the maximum and minimum available convolution values in the array, by the number of sets desired. The user is able to manually, by inspection, threshold the image by only selecting and displaying pixels with a quantized value greater than that of a chosen value (refer to Figure 42). An advantage of this approach is that clearly, if the convolution values were not quantized into a *limited* number of values, attempting to manually adjust the threshold level could be time consuming if the range of convolution values was high.

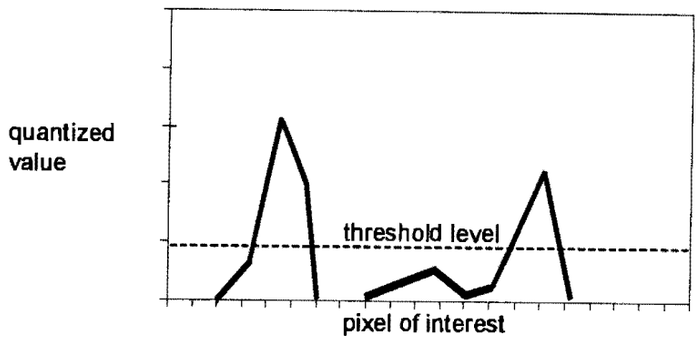

Figure 42 Selection of pixels above a threshold interactively determined by the user

In an image where there is a great variation in contrast between different areas within the image, this thresholding method may at times not provide satisfactory results. A problem arises when a desirable edge lies in an area of the image with low contrast relative to other parts of the image. The convolution values of pixels in this region can only be quantized into relatively few sets. This might make precise selection of the threshold level in this region impossible. An elementary solution is to only perform the edge detection in that region of the image. It is a simple matter for the user to place a window around the area of the image containing the feature of interest and to restrict further calculations to within this window. This not only results in the convolution values of the pixels in this area being spread out over far more quantization sets, but it also greatly increases the speed at which the edge detection calculations can be performed.

It is possible to refine the thresholding process slightly in order to prevent two edges with equal strength being detected on either side of a two pixel wide plateau edge (see Figure 37). This is desirable since the image line defining the edge would otherwise be represented by a two pixel wide line. This can be accomplished by eliminating selected pixels from the horizontal and vertical arrays before they are combined. If two neighbouring pixels in the horizontal array have the same convolution value, then the convolution value of the pixel on the right is set to zero. Similarly, the vertical array is scanned for any occurrence of pairs of pixels directly above one another which have identical convolution values. The value of the bottom pixel of such pairs of pixels is set to zero.

Another situation in which it might be advantageous to modify the thresholding process is that in which an image contains areas of high and low contrast, both of which contain edges which the user wishes to display. The author has had limited success using a thresholding technique nearly identical to that previously described, in order to attempt to solve this problem.

It was previously suggested that areas of low contrast could be manually identified and further calculations restricted to this area. The calculation of quantized values of each pixel within this area would then only be influenced by the convolution values of pixels within the area, and not by those in other parts of the image.

It is possible to similarly reduce the effects of poor contrast by modifying the thresholding process so that it automatically restricts the convolution values considered when determining a pixel's quantized value to only those pixels within its neighbourhood. A pixel with a high convolution value which is in an area of the image where surrounding pixels have even higher convolution values will be allocated a relatively low quantized value. A pixel with a low convolution value which is in an area of the image where surrounding pixels have even lower convolution values will be allocated a relatively high quantized value. Care needs to be taken to ensure that not too many desired genuine edges are lost. This can only be achieved by not only determining an ideal threshold level of the quantized values, but also by determining the ideal neighbourhood size for each image. This proved to be a cumbersome process.

6.1.5 Moment Preservation Technique of Sub-Pixel Edge Location

The previously described edge detection methods are capable of determining at which pixels in an image a possible edge pixel exists. They do so, however, to only single pixel accuracy. This is sufficient to locate the edge pixels of the silhouette edges of a cylinder on an image. However, it is desirable to locate the true position of the

cylinder edge to as high a degree of accuracy as possible. Tabatabai and Mitchell (1984) describe a technique to detect edge locations to sub-pixel accuracy using the method of preservation of moments.

An ideal step edge consists of a sequence of pixels of one intensity followed by another sequence of pixels with a different intensity. An ideal step edge is shown in Figure 43 where the grey level intensities of the two levels of the step are h_1 and h_2. However, in a real image an edge is more like likely to be indicated by a gradual, relatively smooth increase of grey levels between the pixels on either side of the edge. These pixels are shown as a series of crosses (x) in Figure 43. The technique described by Tabatabai and Mitchell determines the most likely sub-pixel position of the edge defined by the sequence of pixels . The position of the edge is indicated in the diagram below by k which is the number of h_1 values from the beginning of the sequence of pixels to the edge.

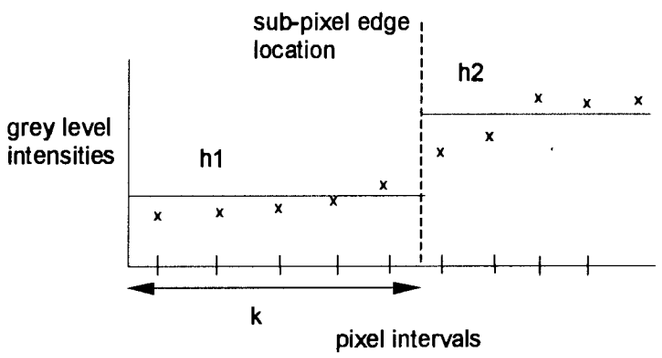

Figure 43 An ideal step edge compared to real pixel data

The algorithm described by Tabatabai and Mitchell is usually applied at an edge pixel which was previously identified using edge detectors capable of single pixel accuracy. The direction of the edge at the pixel of interest was previously determined using the calculated horizontal and vertical convolution values. Using this known direction, the direction orthogonal to the edge can be calculated. A sequence of grey level values can then be calculated extending in this new direction and centred on the pixel of

interest. The grey level values of this orthogonal line are determined by resampling the image, at intervals of one pixel for each new element of the sequence, on both sides of the central pixel. This ensures that the sequence of grey level values used is in the direction of maximum gradient at the pixel of interest.

Resampling of the new grey level values may be performed through a variety of methods, however, a simple method is that of bilinear interpolation as shown in Figure 44.

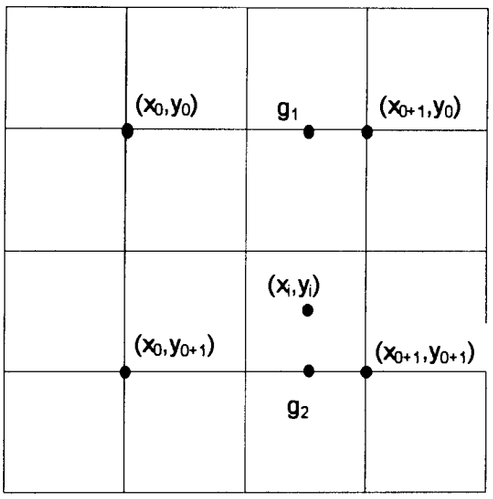

Figure 44 Resampling by means of bilinear interpolation

$g(x_i,y_i)$ represents the grey scale value at the point (x_i,y_j) which has non-integer co-ordinates. $g(x_i,y_i)$ is resampled based on the grey values of the surrounding pixels which have integer co-ordinates. The bilinear interpolation equations is given by:

$$g(x_i, y_i) = g_1 + (g_2 - g_1)(y_i - y_0)$$

Equation 64

where:

$$g_1 = g(x_0, y_0) + (g(x_0 + 1, y_0) - g(x_0, y_0))(x_i - x_0)$$
$$g_2 = g(x_0, y_0 + 1) + (g(x_0 + 1, y_0 + 1) - g(x_0, y_0 + 1))(x_i - x_0)$$

Equation 65

The sub-pixel edge location method is described using the following equations (Equation 66-Equation 73) and refers to Figure 43.

The first three sample moments of the input data to be preserved are given by:

$$\overline{m}_i = \frac{1}{n}\sum_{j=1}^{n} x_j^i$$

Equation 66

where:

i = 1,2,3 are the moments to be preserved

j is the position of each grey level value in the sequence

n is the number of pixels in the sequence

Letting k denote the number of h_1 values from the beginning of the sample to the ideal edge, there are three equations to solve for the unknowns h_1, h_2 and k (Smit, 1997).

$$\overline{m_1} = \frac{kh_1 + (n-k)h_2}{n}$$
$$\overline{m_2} = \frac{kh_1^2 + (n-k)h_2^2}{n}$$
$$\overline{m_3} = \frac{kh_1^3 + (n-k)h_2^3}{n}$$

Equation 67

The final sub-pixel location of the step edge may then be determined from Equation 68. The edge of the first pixel in the sequence is at j=1/2 and the edge is found a distance of k from this position. Once the sub-pixel edge position in the sequence is known, its position in the sequence relative to the central pixel of interest can be calculated. The image co-ordinates of the edge can then be determined from this relative position and the image co-ordinates of the central pixel of interest. The solution is:

$$k = \frac{1}{2}n(1 - \frac{c}{\sqrt{4+c^2}})$$

Equation 68

where:

$$c = \frac{3\overline{m_1 m_2} - 2\overline{m_1}^3 - \overline{m_3}}{\sigma^3}$$

Equation 69

and

$$\sigma = \sqrt{\overline{m_2} - \overline{m_1}^2}$$

Equation 70

$$h_1 = \overline{m_1} + \beta\sigma$$

Equation 71

$$h_2 = \overline{m_1} - \frac{\sigma}{\beta}$$

Equation 72

$$\beta = \sqrt{\frac{k}{n-k}}$$

Equation 73

The sub-pixel location of any edge identified in the image using the methods described in Sections 6.1.1 - 6.1.3 may be found in this way. While it is possible to perform this calculation on all the possible edge pixels identified in an image, it is less computationally expensive to first determine which edge pixels define a silhouette edge on the image. Sub-pixel edge location can then be performed on only these pixels.

6.2 Line Extraction

The application of the edge detection and subsequent thresholding methods described in previous sections results in an edge map image. It is convenient to present this image as a binary image; every pixel determined during the thresholding process to be a desirable edge pixel is given the same high grey level intensity and all others are presented as black. Providing a suitable threshold was selected, the edge pixels representing the cylinder's silhouette edge line will be amongst those edge pixels visible. In order to determine the parameters of this line, a line which is best represented by these pixels must be found.

In the following sections, two simple methods which have been developed to determine which pixels in the image represent the straight line, are described. Once the pixels have been identified it is possible to determine the parameters of the line which passes through them. Another method, the Hough Transform, was also investigated but was later found to be unsuitable for the requirements of this thesis;

this method will also be briefly discussed. An important criterion upon which the selection of a method was based was that it should be as automated as possible on the one hand, and yet at the same time highly reliable. A compromise needs to be found between these two requirements. It is perhaps more inconvenient for an operator to be required to check and edit the results of an automated method than it is for the user to be involved from the start of the selection process of a semi-automated method.

6.2.1 The "Best-Fit" Line Following Method

The more automated of the two methods developed is the "best-fit" line following method. This is a semi-automated method which requires very little interaction from the operator. The operator merely needs to indicate the approximate start and end points of the line on the image and the algorithm then determines which edge pixels most likely form the indicated line.

The algorithm requires two initial pixel co-ordinates. These co-ordinates are determined by the operator using a mouse to indicate on the image the approximate start and end points of the line. The two indicated pixels have to be within a coarse threshold distance from the "true" line. As the algorithm was implemented in this thesis, these points have to be within three pixels of the "true" line. A line is then formed between these two initial pixels. As shown in Figure 45, all edge pixels which fall within the distance of the coarse threshold value from this line are selected and placed into a chain. As can be seen from the figure, not all of the pixels which fall within these bounds and are selected are in fact pixels which form the "true" line. However, provided the two initial points are within the coarse threshold of the "true" line and that the line is well represented by edge pixels, the majority of points selected will belong to the "true" line and few pixels belonging to this "true" line will be ignored.

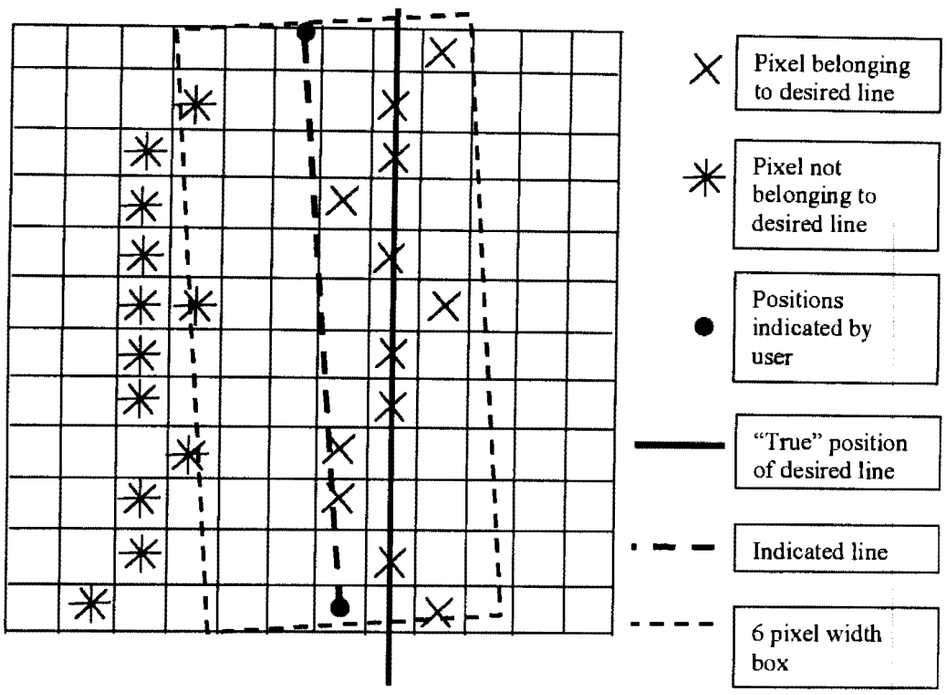

Figure 45 Edge pixels falling within the coarse threshold distance from the line, indicated by the user, are added to a chain of pixels for future calculations

If the sub-pixel edge location (section 6.1.5) at each of the pixels in the chain has not previously been determined, then it must be done so now. Linear regression (discussed later in Section 6.2.3) is then performed on the chain of pixels in order to establish the parameters of a line which can be best fitted through them. Equation 74 and Equation 75 (pg. 117) give the parameters a and b of this line in which x and y are the pixel image co-ordinates of each edge pixel in the chain. Due to the influence of pixels in the chain which were not part of the "true" line, the new line will not coincide with the "true" line, but will approximate its position.

Once the parameters of this new line are know, the second stage of the calculations can begin. All of the edge pixels in the image which are within the distance of a fine threshold value from the new line are selected and placed into a second chain. This is shown graphically in Figure 46. A value of one for the fine threshold was used in the tests in this thesis. This has the effect of removing those pixels in the chain which are unlikely to belong to the "true" line while retaining most of those that do. New,

previously excluded pixels may also be selected, although this is unlikely to occur if the operator indicates the two initial points sufficiently close to the desired line. Once again the parameters of the best fitting line through the pixels in the second chain is determined. This best fitting line and its parameters indicate the true silhouette cylinder edge sufficiently well to be used in the cylinder parameter determination methods described previously in Chapter 5.

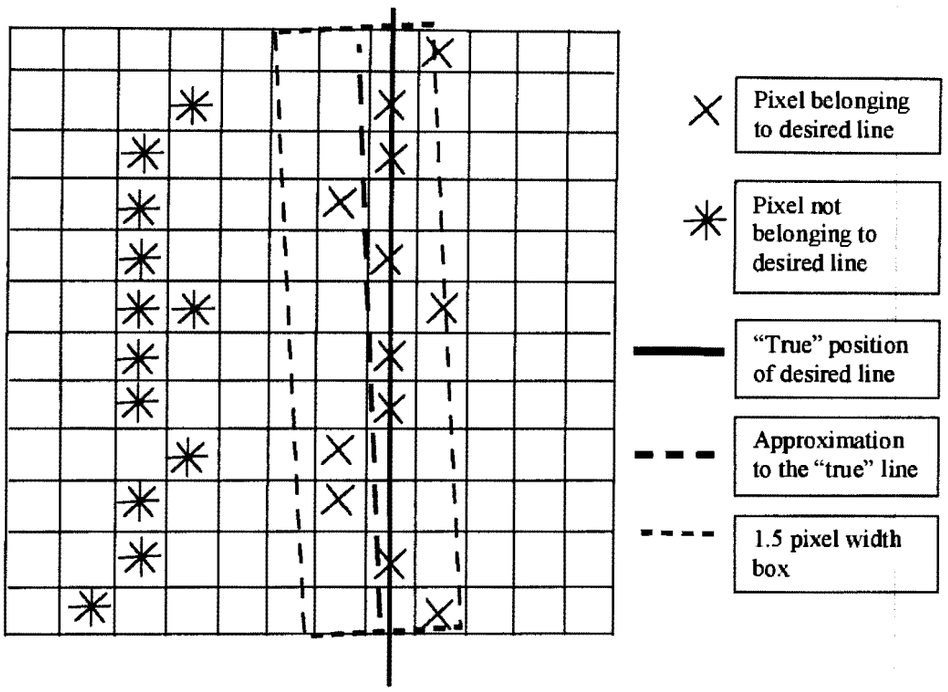

Figure 46 Edge pixels falling within the fine threshold distance from the line previously calculated are added to a second chain of pixels from which the final best-fitting line can be calculated

Whilst this method is quick and convenient it has some limitations. If there are many edge pixels within the coarse threshold distance of the initially indicated line which do not belong to the "true" line, then it is possible that the line calculated in the second step may be significantly far from the "true" line. Should this occur, insufficient edge pixels belonging to the "true" line will be selected for the final chain. The line best fitting through points in this chain will not be sufficient to represent the "true" line in further calculations. This can be alleviated somewhat by ensuring that the user indicates the two initial points as close to the "true" line as possible. Furthermore, the

user could modify the threshold values until they are optimum, this however, is inconvenient.

As a result of these limitations it is inadvisable to use this method in situations where two edge lines lie close together or where the signal to noise ratio of the line is poor in relation to surrounding edge pixels. In these situations it is preferable to use a method in which the user has more control. One such method is presented in the following section.

6.2.2 The Manual Line Following Method

A method has been developed which allows the operator greater control over which edge pixels are selected, compared to the control offered by the method described in the previous section. This second method still attempts to keep the amount of user input to a minimum. This method is more reliable than the previously described method in situations where edge lines lie in close proximity to each other. This situation frequently occurs where true edges of a feature lie near "false" edges created by shadows.

The technique requires that the operator identify both the start and end points of the line to be extracted, as in the previous method. However, unlike the previous method, it is necessary that these two points accurately identify edge pixels that lie on the desired line. This is necessary since, unlike the previous method in which the two initial points merely define an approximation to the desired line, these two points not only provide an approximate direction of the line, but they are also used as the start and end points for line following. Line following is carried out by a simple linking method which starts at the initial point, proceeds in the determined direction and connects each edge pixel to one of its neighbours until the identified end point is reached. Specifics of the method are described later in this section.

Both van der Merwe (1994) and Heipke *et al* (1994) describe line following techniques which are based on linking neighbouring pixels together.

The line following technique that van der Merwe employed is designed to extract the boundaries of features. He describes a method in which a mask is placed over a pixel of interest. Every neighbouring pixel is examined in turn to determine whether it is an edge pixel. Figure 47 shows that the order in which the neighbouring pixels are examined is determined from the relative position in which the previous edge pixel was found. If for instance, a pixel is found at position 4 in the current search (inner ring), the next search will start at position 2 (outer ring). In this way van der Merwe allows the selection of pixels which deviate slightly from the previous direction of tracking. The algorithm is designed to be optimised for speed as well as preventing the tracking from reversing direction and returning upon itself. Van der Merwe successfully implemented this method to track around the boundary of a feature. However, it does not constrain the search sufficiently to ensure that only straight lines are extracted; unless there are no further new neighbouring pixels, a new pixel will always be added to the chain.

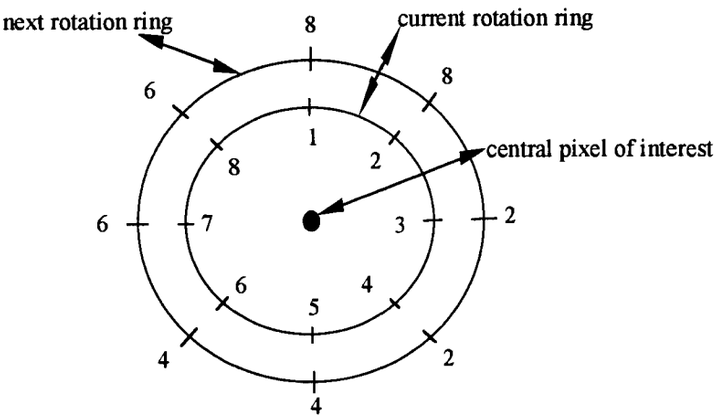

Figure 47 A circular search order for line following

Heipke *et al* describes a method of line following intended to extract the edges of roads from aerial images. While this method once again does not restrict itself to

extracting merely edge pixels belonging to straight lines, it does provide a useful basis on which to build an algorithm which does. The technique described by Heipke is based on a number of search matrices. Each search mask in centred on the current pixel of interest and corresponds to a particular search direction. The search direction is determined from previously extracted edge pixels. Only certain pixels within the search matrix associated with the current direction are examined at the pixel of interest. If no further edge pixels are found, perhaps due to a gap in the line being followed, the search process is terminated and waits for further input. Like the method employed by van der Merwe, this method can track curved lines. However, by restricting searches to matrices associated with the current search direction, it more effectively prevents the selection of pixels which would result in a sudden change of tracking direction and which may not belong to the line being followed.

The technique developed in this thesis and presented below is based on that of Heipke's. However, unlike Heipke's method, this technique must restrict itself to edge pixels which form a sequence of pixels approximating a straight line. Furthermore, the technique attempts to reduce the amount of user interaction required by reducing the number of occasions upon which the extraction process terminates due to a gap in edge pixels. For this reason the technique was developed to be capable of bridging a four pixel wide gap in the line. It could be modified to bridge a larger gap, however this would increase the possibility of mis-identifying an edge pixel as part of the line.

Once the two initial edge pixels have been correctly identified by the operator, the direction from the first to the second is determined. This direction is then set equal to the closest quantized value of one of 24 directions between 0° and 360°, each having a range of 15°. Using this quantized direction, a search mask can be selected to be used for the duration of the entire line following session for the particular line.

The search mask is placed over the starting pixel indicated by the operator. Examples of two search masks are given in Figure 48. The numbering of the elements of the masks indicate the order in which the neighbouring pixels are searched. The search

positions and their sequence are derived heuristically by inspection. A table showing the evaluation sequences and positions for all the quantized directions is given in Section 11.2.

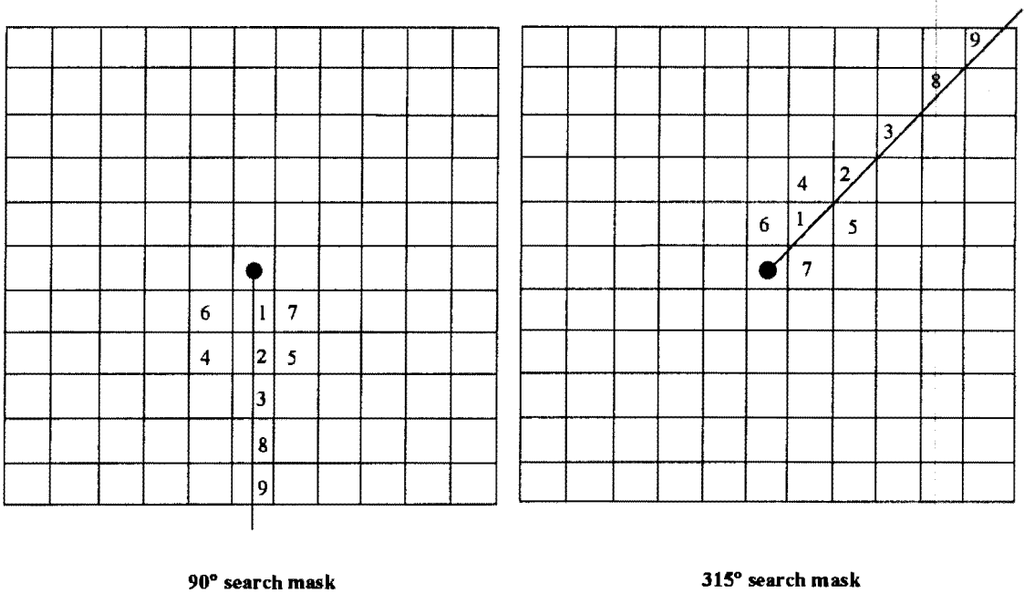

Figure 48 Two search masks centred over a pixel of interest. The surrounding pixels are searched for edge pixels in the order of the numbers shown

Initially only pixels in the search positions 1-3 are examined. The pixel co-ordinates of any of these pixels which are found to be edge pixels are added to the edge pixel chain. If an edge pixel is found within the first three pixels of the sequence, a new search is begun, using the same search direction and centred on the last pixel added to the chain. The new search is centred on the last pixel added to the chain, furthest from the previous pixel of interest, in an attempt to ensure that the direction between the two successive positions of the search mask as closely as possible approximates the intended direction of the search. This in turn ensures that the tracking continues in the direction of the end point indicated by the user.

Should an edge pixel not be found in the first three pixels, then positions 4-7 are checked (in sequential order). Positions 4-7 are only checked if no edge pixels are

found in positions 1-3, since positions 1-3 better approximate the search direction than positions 4-7. Furthermore, positions 4-7 are checked in numerical order since positions 4 and 5 better approximate the search direction than positions 6 and 7. Immediately an edge pixel is found in any of these positions, its pixel co-ordinate is added to the edge chain and a new search is begun, centred on this pixel.

Finally, should no edge pixels be detected in positions 4-7, then a further two pixels are checked at positions 8 and 9. Whilst these positions approximate the search direction better than any of the previous positions, positions 1-7 are checked first in an attempt to associate as many edge pixels as possible with the line being followed. Should a pixel finally be found at position 9, the line following process will have succeeded in bridging a four pixel wide gap. Should no pixel be found in any position, the tracking process terminates and requests that the user reposition it on a new edge pixel.

Although examining positions 4-7, which do not approximate the intended search direction as well as the other search positions do, allows the technique to be used in "real world" images, it also increases the possibility of the tracking being led away from the desired line. If the new search position is repeatedly found at one of these positions (i.e. position 7), the chain of pixels that is built up will move away from the desired line.

A simple and effective check is performed to prevent this from occurring. A check is performed each time five new pixels have been added to the chain since the last check was performed. The direction between the last pixel and the fifth last pixel in the chain is determined. This direction is then set equal to the nearest quantized search direction. The quantized values one above and one below this value are also determined. These three directions are then compared to the initial quantized search direction which was calculated using the beginning and end points of the line indicated by the user. If none of the three directions match the initial quantized search

direction then it is assumed that the tracking has moved too far away from the intended line and the tracking is terminated.

The explanation above can perhaps be better understood using a numerical example. If the direction between the beginning and end points of the desired line, as initially indicated by the user, is 65°, then the nearest quantized direction value is 60° (assuming 0°-360° is divided into 15° intervals). If the direction between the last five pixels in the edge chain is found to be 63°, then the nearest quantized direction value is 60°. The quantized values above and below this direction are 75° and 45°. In order for the tracking process to be allowed to continue, one of the three directions, 45°, 60° and 75° must match the initial quantized search direction (60°). In this example a match occurs and the tracking process is assumed to be proceeding correctly.

In practice this line following technique has proved consistently reliable, often requiring only minimal intervention from the operator. Although its inability to bridge gaps of greater than four pixels in a line results in it being less automated than the method described in Section 6.2.1, it can be used in situations in which that method simply cannot be used.

6.2.3 Linear Regression

Linear regression is required as a component of the line following method described in Section 6.2.1 as well as the method described above. If the method described above is used, a final chain of edge pixels will be produced containing pixels which are believed to represent the silhouette edge line on the image. The sub-pixel positions of the edge pixels can then be determined using the algorithm described in Section 6.1.5. In order to determine the parameters of the line best fitting through the points in the chain, linear regression must be performed.

If a line is represented in image space by an equation of the form given in Equation 39, then the parameters a and b may be determined from Equation 74 and Equation 75.

$$a = \frac{(\sum x^2)(\sum y) - (\sum x)(\sum xy)}{n(\sum x^2) - (\sum x)^2}$$

Equation 74

$$y = \frac{n(\sum xy) - (\sum x)(\sum y)}{n(\sum x^2) - (\sum x)^2}$$

Equation 75

where:

(x,y)	are the image co-ordinates of each pixel in the chain
n	is the number of pixels in the chain

An important consideration when performing linear regression on points extracted from an image and intended to represent a line on the image, is that the co-ordinates of each point must be assumed to be effectively on an *undistorted* image. In other words the image co-ordinates used in the linear regression calculations must have had the effects of lens and other distortions removed from them before the regression calculations are performed. Figure 49 shows graphically how the line determined by linear regression is shifted from its true position if the affects of distortion are not removed prior to the regression calculations.

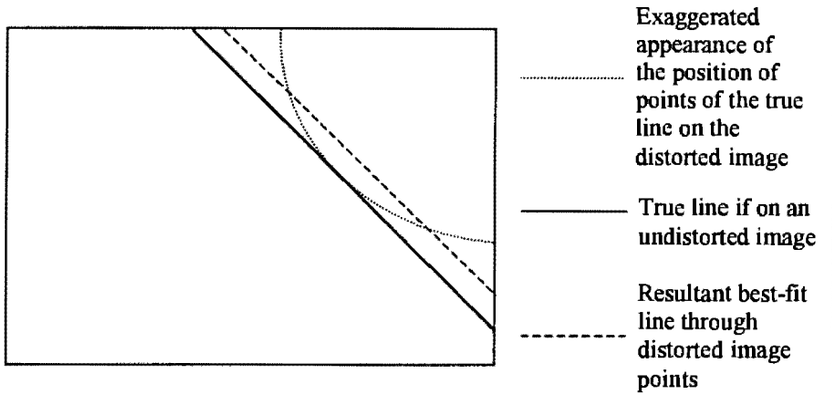

Figure 49 An exaggerated effect of applying linear regression to points on an image distorted by radial distortion

Unless image distortions are taken into account, an image point will not fall precisely on the image where the perspective projection transformation would state it should fall. If distortions are not removed from the individual image points before linear regression is applied, the best-fitting line that is determined will not represent the position where the true line falls. Furthermore, it is not possible to later apply corrections for distortion to points which were determined on this line using the calculated line parameters.

Whilst the effect of distortion may not always be sufficient to prevent the line being tracked, the effect of distortion *is* sufficient to affect the final parameters of the desired line. This in turn will affect the accuracy with which the parameters of the edge-planes can be determined, as described in Chapter 5, and subsequently reduce the overall accuracy of the techniques.

6.2.4 Hough Transform Technique

Although the two methods described in Sections 6.2.1 and 6.2.2 above were found to be the most suitable for the requirements of this thesis, another method was initially investigated and is described here.

The Hough transform is a method that can be used to detect straight lines and curves in images. The method is given the family of curves being sought and produces the set of curves from that family that appear on the image (Haralick and Shapiro, 1992).

Adamos and Faig (1992) claim that the advantage of using a Hough transform to detect lines in an image is that the algorithm is unaffected by gaps in lines. Furthermore, they report that the technique performs well in the presence of noise.

The technique is termed a transform since the edge pixels in the image are mapped into sinusoidal curves in parameter space. If for a number of image points, the corresponding sinusoidal curves intersect at a common point (θ_K,ρ_K) then these points lie on a straight line (Adamos and Faig, 1992). For straight line extraction the definition of a straight line is chosen to be that given previously in Equation 40, where the line is defined by θ and ρ. Parameter space is therefore defined with θ in one axis and ρ in the other. Every edge pixel which is mapped into parameter space has an associated θ and ρ value. An accumulator array can be built from these values. Both the range of θ and ρ values can be quantized into a number of sets; e.g. θ may be quantized into 36 sets each with a range of 10° and ρ may be quantized into sets each covering a distance of three pixels. The dimensions of the accumulator array correspond to the quantized values of θ in one direction and the quantized values of ρ in the other. This concept is illustrated in Figure 50.

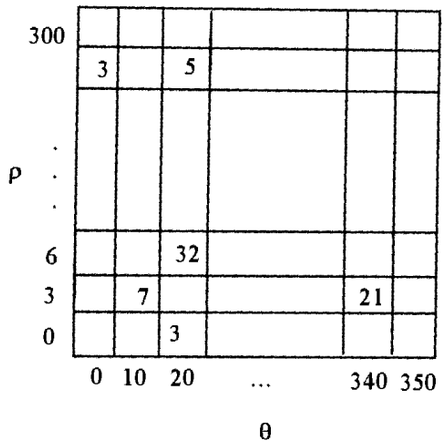

Figure 50 An accumulator array for finding straight lines (Adamos and Faig, 1992)

At each pixel in the image the parameters θ and ρ are determined from the convolution values previously calculated by an edge detection method. θ is the edge direction at the pixel and ρ is the distance between the pixel and the origin of the pixel co-ordinate system. In order for an accurate edge direction to be calculated, an edge detection method which produces edge strength values in both the x and y directions must be used. The θ and ρ values determined at a pixel of interest are then set equal to the closest θ and ρ quantized values respectively. The value of the element in the accumulator array corresponding these values is then incremented by one.

All the pixels in the image are examined in this way and the accumulator array filled. The most probably straight lines in the image correspond to lines represented by accumulator array elements whose values are the highest. Provided a separate array of the parameter values of each pixel is kept, it is possible to then find the pixels which most likely form lines in the image.

The Hough Transform appears to offer a convenient automated way to extract straight lines from an image. However, it was found that the Hough Transform has some shortcomings which made it unsuitable for use in this thesis. Firstly, it is necessary to

determine the ideal number of sets into which to quantize θ and ρ. This differs from image to image. Secondly, it is still necessary for the user to indicate which of the lines found in the image is the desired line. However, the greatest drawback of this technique considering the environment and nature of the images used in this thesis, was its lack of reliability. Although the desired line was some times detected, it just as frequently went undetected. It is most likely that this problem was related to the selection of the number of quantization sets as well as the accuracy of the edge directions determined by the edge detectors. For these reasons it was decided to utilise the semi-automatic methods described above in Sections 6.2.1 and 6.2.2, since ultimately they proved to be more appropriate for the task

7 TESTING PROCEDURE AND DISCUSSION OF RESULTS

Testing of the methods described in Chapter 5 was carried out using four different scenarios. The objective in each case was to determine whether the methods could calculate the position and orientation of a cylinder axis sufficiently accurately and with sufficient repeatability so as to be viable techniques for measuring pipes in an industrial plant. The absolute accuracy to which pipes must be measured when building an as-built CAD model of an industrial plant varies. However, these accuracy requirements are not as stringent as in other areas of industrial photogrammetry and accuracies of 10-20mm are usually considered sufficient. This is true because of the level of tolerance considered acceptable between connecting pipes during the construction and fitting process. Pipes are often lagged, supported by adjustable brackets off pillar centres and may even be suspended from springs to allow for large expansion differential movements (Lloyd, 1995). PDS software packages are also capable of manipulating calculated data within a CAD model to ensure that the data correctly models the functionality of the pipe network.

7.1 Description of the Testing Procedure

The testing procedure used for the four scenarios was similar in each case. This section presents a brief description of the common procedure which was followed in order to obtain the cylinder parameters for each test case. Details specific to each particular scenario are discussed later in the chapter. The chart shown in Figure 51 shows the various steps in the common procedure. These steps are explained more fully in the text following the chart.

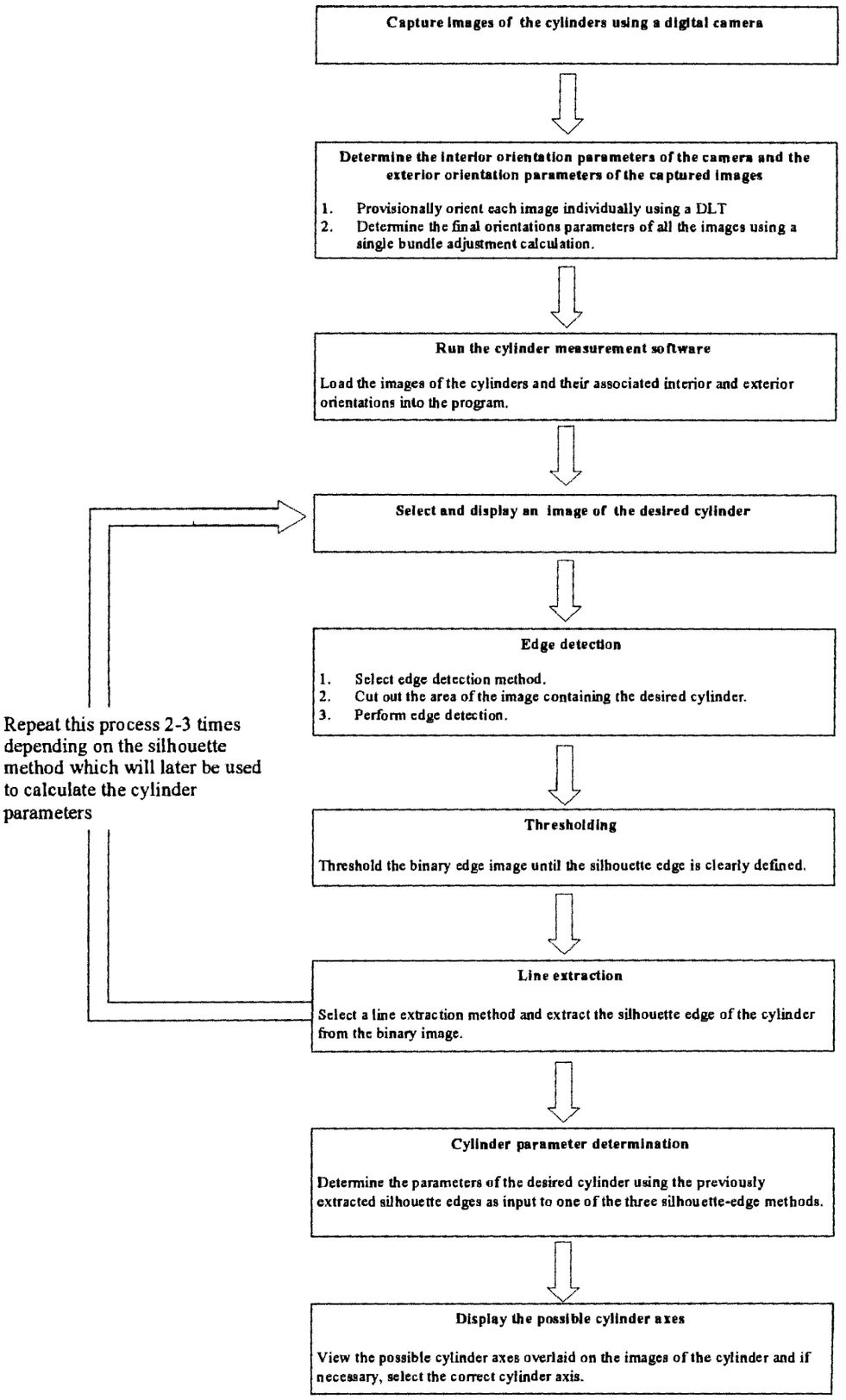

Figure 51 The chart shows the steps involved in determining the parameters of a cylinder

All images were captured using a Kodak DCS420 camera. The DCS420 is a still digital camera with a 14x9.3mm CCD sensor chip with 1524x1012 pixels, with each pixel approximately 9x9μm in size. An integrated removable PCMCIA hard drive provides storage for the captured images. During these tests a wide-angle Sigma lens with a 14mm focal length was used. The DCS420 is a popular camera for digital photogrammetry and its suitability for achieving high accuracy results has been well documented (Fraser and Shortis, 1994).

The images were oriented using control points placed within the field of view of the camera. The object co-ordinates of these points were pre-determined before the images were captured. Photogrammetric software developed within the Department of Geomatics was used to manually locate and label some of the control points in the image. The image co-ordinates of the centres of these points were then calculated by the software. The remaining control points in the image were subsequently automatically located, the image co-ordinates of their centres found and then each control point was correctly labelled by the software. This process was carried out for each image in the set used for measuring the cylinder.

The image co-ordinates of the control points visible in each image were used to calculate provisional interior and exterior orientations for the images using a separate DLT calculation for each image. Once the provisional interior and exterior orientations of each image had been calculated, these, together with the image observations of the control points measured in all the images, as well as the control points co-ordinates, were adjusted in a single bundle adjustment solution. The output produced by the bundle adjustment are the interior orientation parameters of the camera that was used and the refined exterior orientation parameters of each individual image. For an explanation of both the mathematical and practical aspects of camera calibration and image orientation, the reader is referred to Section 3.2.

The output of the bundle adjustment software provided the input required by the cylinder measurement software developed as part of this thesis. Appendix 11.1 provides an overview of some of the programming aspects relating to this thesis.

All the images used to determine the cylinder's parameters were first loaded into the cylinder measurement program. At the same time the interior and exterior orientation parameters of each image were loaded and stored in memory. The first image to be processed was then selected from a menu and displayed. This can be seen in Figure 52.

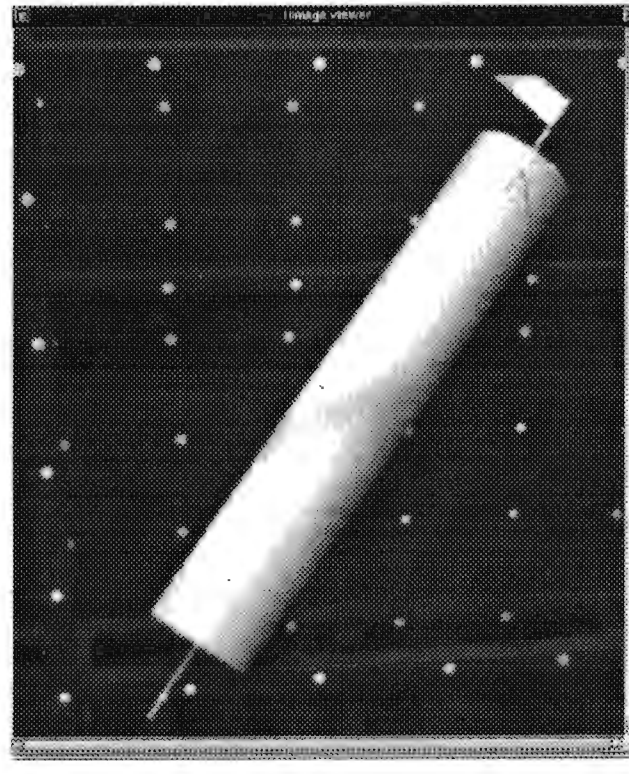

Figure 52 An unprocessed image of a cylinder with control targets in the background

Using the menu system, a method of edge detection was selected. For these tests the Canny operator (described previously in Section 6.1.3) was chosen and the parameter σ was set to 1. In order to reduce processing time, as well as the likely resultant range of convolution values, the section of the image containing the cylinder was "cut-out" from the original image prior to the edge detection calculations. The resultant binary edge image (as shown in Figure 53) was then thresholded by inspection until the silhouette edges of the cylinder were clearly defined.

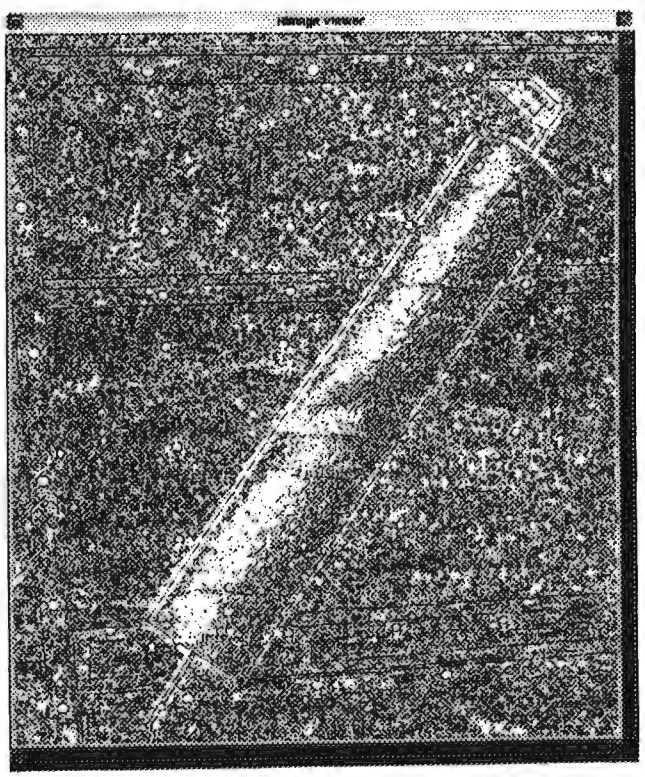

Figure 53 An unthresholded binary edge image

Depending on how clearly the silhouette edges in the image were defined, one of the two line extraction methods described in Section 6.2 was selected from the menu. The start and end points of the lines were then indicated manually and the line extracted (as indicated in Figure 54). A detailed description of the edge detection and line extraction techniques is given in Chapter 6. The extracted silhouette edge was then associated with a label identifying the cylinder. This process was repeated for all the images to be used.

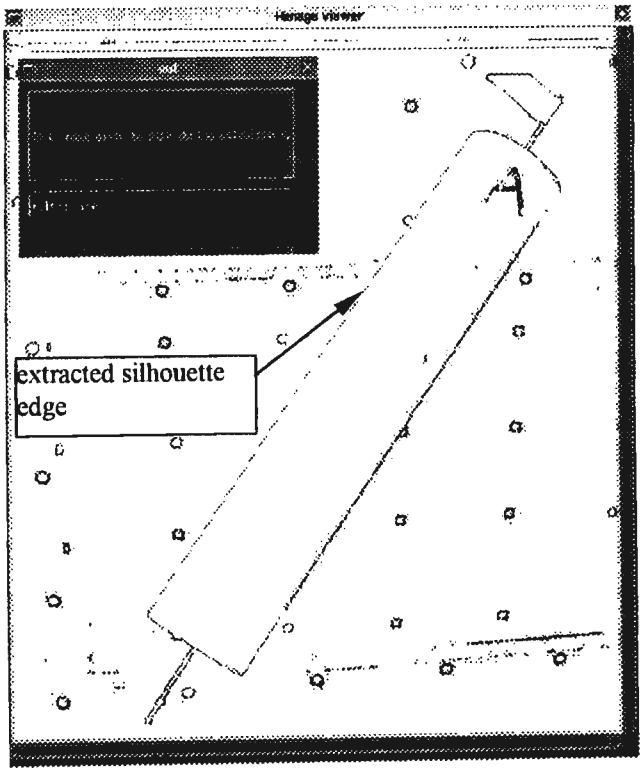

Figure 54 A thresholded binary edge image showing an extracted silhouette line

Finally, the parameters of the cylinder were calculated by selecting one of the three silhouette-edge methods (see Chapter 5) for each cylinder in turn. Once the position and orientation of the cylinder were calculated, the original images could be redisplayed and the axis projected into the image if desired (as indicated in Figure 55).

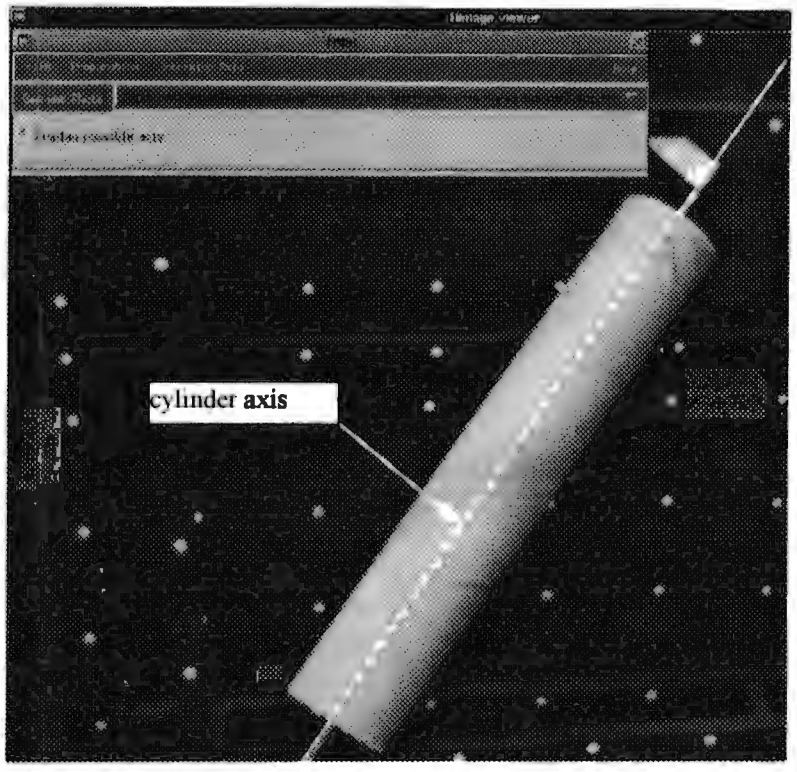

Figure 55 Original image with the calculated cylinder axis projected into it as a line

7.2 Calculation of the Parameters of a Small Bore Cylinder: Test A

The initial set of tests using the silhouette-edge techniques were performed on a small bore tube. Repeated physical measurements of the tube using vernier callipers determined a mean radius of 42.0mm. However, the diameter differed slightly at various sections of the tube, resulting in variations of as much as ±0.2mm in the radius.

Control points for orientation of the images were provided by placing the tube directly in front of a control frame. The images were captured from camera positions that varied between 0.8m and 1.6m from tube. The tube was positioned in various poses with respect to the co-ordinate system to determine whether the pose of the cylinder had any significant effect on the method's ability to produce consistent results.

The figures below give a graphical representation of the six poses of the tube used in the tests.

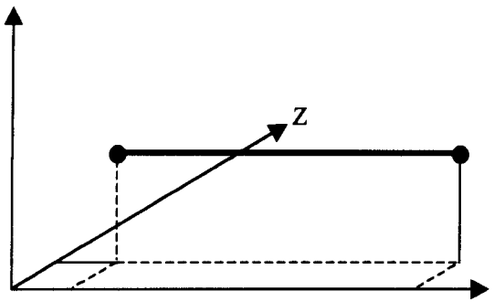

Figure 56 Cylinder pose No.1

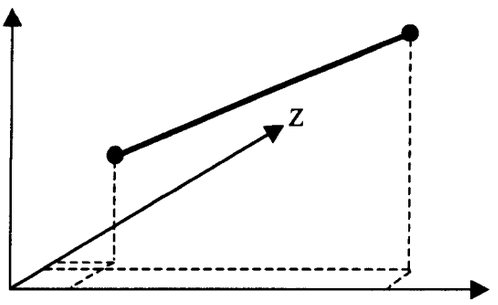

Figure 57 Cylinder pose No.2

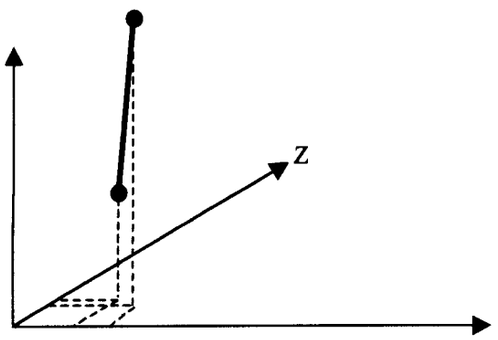

Figure 58 Cylinder pose No.3

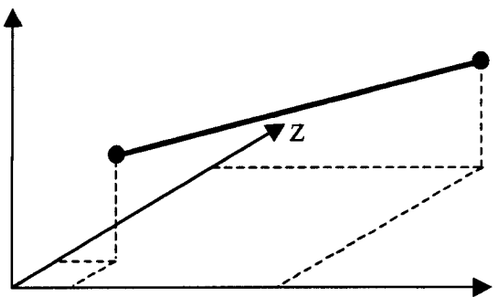

Figure 59 Cylinder pose No.4

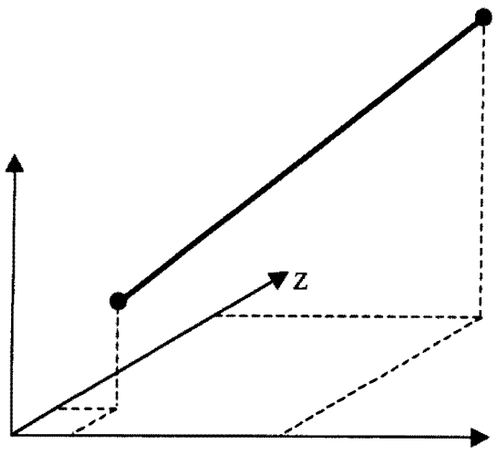

Figure 60 Cylinder pose No.5

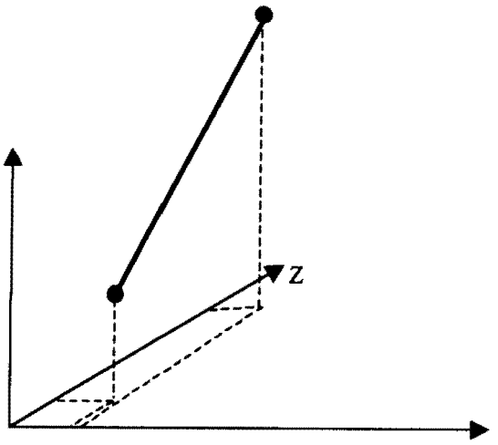

Figure 61 Cylinder pose No.6

A number of images of the cylinder were captured for each pose and each image in the set was captured from a different camera position. An attempt was made to ensure that the intersection angles between the edge bisector planes of successive images in a set was similar and that the angle formed between the first and last image in each set was as large as possible. Figure 62 shows graphically what is meant by the intersection angle between two edge bisector planes.

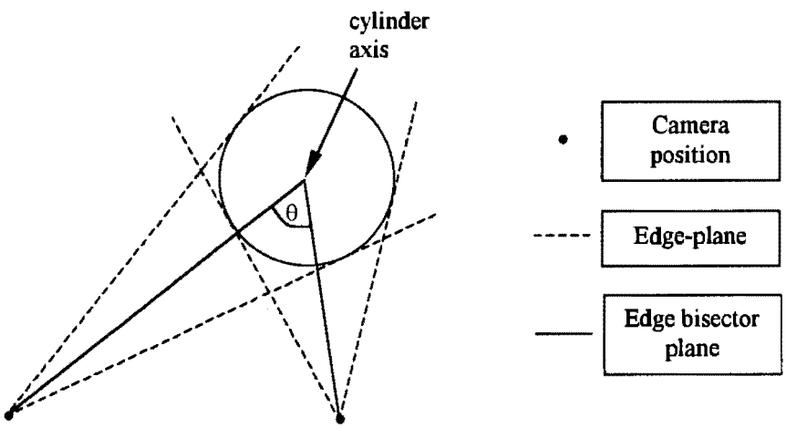

Figure 62 The angle formed between two edge bisector planes is shown as θ

By determining the tube's parameters using successive images in a set, as well as later those which were not successive, it was possibly to study whether altering the

intersection angle between the edge bisector planes affects the results in any significant way.

In order to provide a comparison with the results obtained using the silhouette-edge methods, it was necessary to determine the tube's parameters using a further method. A thin metal rod was positioned along the longitudinal axis of the tube with retro-reflective targets attached to the surface of the rod at either end of the tube. The positions (pt_1 and pt_2) of these two targets were determined photogrammetrically for each pose. These two points were intended to define the true axis of the cylinder and should lie on the axis determined using the silhouette-edge methods, provided these methods determine the axis accurately. However, inaccuracies in positioning the rod centrally in the tube, as well as the 1.5mm offset of the targets from the surface to the centre of the rod, reduce the accuracy with which the "true" axis could be defined. Furthermore, a certain amount of observational error is introduced during the photogrammetric determination of these points. As a result, these two points cannot be expected to define the true axis with an accuracy of greater than approximately 3mm.

Although the three-edge-planes (TEP) and three-separated-edge-planes (TSEP) methods were also tested, only the results of the four-edge-planes (FEP) method are shown in this section. A second set of tests was later conducted and the results of this second test, using the TEP and TSEP methods, are consistent with the results obtained for this first test. A discussion and the results of the second test, using all three methods, are presented in Section 7.3.

Table 2 shows the results calculated using the FEP method for each set of data. The results within each set are ordered by intersection angle between the two axes defining the edge bisector planes. The calculated radius values are displayed in the table. The distances (Δpt_1 and Δpt_2) from the calculated axis to the two points (pt_1 and pt_2) which lie on the "true" axis are also shown. *Mean* and *range* values (the difference between

the smallest and largest value in a set) are calculated for various values within each set.

Set	Intersection angle (degrees)	Radius (mm)	Δpt1 (mm)	Δpt2 (mm)
1	31	42.18	2.29	1.43
	39	41.98	2.32	1.96
	46	42.07	2.08	1.35
	71	42.03	2.18	1.85
	mean	42.07	2.22	1.65
	range	0.20	0.24	0.61
2	37	42.10	3.19	1.93
	38	42.21	2.68	1.86
	75	42.24	2.75	1.88
	mean	42.18	2.87	1.89
	range	0.14	0.51	0.07
3	35	42.05	2.11	N/A[2]
	39	42.08	2.30	N/A[2]
	74	42.06	1.63	N/A[2]
	mean	42.06	2.34	N/A[2]
	range	0.03	0.67	N/A[2]
4	17	42.00	1.94	1.57
	27	42.28	1.94	1.56
	45	42.12	1.94	1.57
	mean	42.13	1.94	1.57
	range	0.28	0.00	0.01
5	29	42.02	2.15	1.27
	43	41.99	2.15	0.88
	72	42.13	2.09	0.68
	mean	42.05	2.13	0.94
	range	0.14	0.06	0.59
6	47	42.06	2.5	2.52
	74	42.14	2.18	1.97
	mean	42.10	2.34	2.25
	range	0.08	0.32	0.55
Overall mean		42.10		
Overall range		0.30		

Table 2 Summary of results using the FEP method: Test A

Referring to Table 2 it can be seen that the overall mean value calculated for the radius is 42.10mm. This differs by 0.10mm from the radius of the tube determined using the vernier callipers. Furthermore, the overall range of radius values shown in

[2]Due to an error in data capture, the object co-ordinates of this point were not determined.

the table is 0.3mm. This compares favourably with the 0.2mm variation in radii experienced when measuring the cylinder with the vernier callipers. Although the mean radii of each set differs between sets, it is not possible to state that any pose results in significantly better or worse determination of the radii. Furthermore, it does not appear that the intersection angle of the edge bisector planes has any significant effect on the radius value calculated.

It is meaningless to examine the overall mean value for Δpt_1 and $\Delta pt2$ since the object co-ordinates of pt_1 and pt_2 differ for each set and were calculated separately. However, the *mean* and *range* values of Δpt_1 and $\Delta pt2$ within each set are meaningful. In all cases Δpt_1 and Δpt_2 are within the 0-3mm range to which pt_1 and pt_2 were able to be determined with respect to the true axis. This suggests that the method is capable of determining the axis no less accurately than it could be defined using the photogrammetrically determined points, pt_1 and pt_2. If it were assumed that pt_1 and pt_2 do not lie on the true axis, it would be expected that Δpt_1 and Δpt_2 would be non-zero values. If the true axis parameters had been correctly determined using the silhouette-edge method, then the values Δpt_1 and Δpt_2, although non-zero, would be expected to be constant for all angles within a specific set and their range within the set would be expected to be zero. The range within each set therefore gives a measure of how *consistently* the method determines the axis position.

All of the sets, with the exception of set 4, have ranges for Δpt_1 and/or Δpt_2 of approximate 0.50mm. No single set displays a range significantly different from the other sets. Furthermore, there is no evidence that the intersection angle has any significant affect on the results.

7.3 Calculation of the Parameters of a Small Bore Cylinder: Test B

A second test, similar to that conducted in the previous section, was carried out. In the previous test it had proved difficult to determine the true axis parameters of the

cylinder in order to compare them with the results obtained using the methods being tested. In an attempt to better determine the true parameters of the tube for comparison purposes, a different technique to that used in the first test was used to measure the true axis.

Small, white, circular balls were placed onto the ends of the rod running through the tube. Since the balls are spherical they appear as circles on an image, irrespective of the camera position from which the images were captured. The image co-ordinates of the centres of these circles can be found using the same target detection algorithm as was used to find normal retro-reflective stick-on targets. If the tube is photographed from a number of camera stations, it is possible to determine the co-ordinates of object points formed from the intersection of these image co-ordinates. These object points will be the centres of the balls. If the tube is then rotated 180° about its longitudinal axis, a second object co-ordinate can be found corresponding, once again, to each ball. As indicated in Figure 63, the mean value of the co-ordinates of the two object points corresponding to each ball, will produce the object co-ordinate of a point which lies on the longitudinal axis of the tube. In this way, the true axis of the tube can be defined by the co-ordinates of two points lying on the tube's axis.

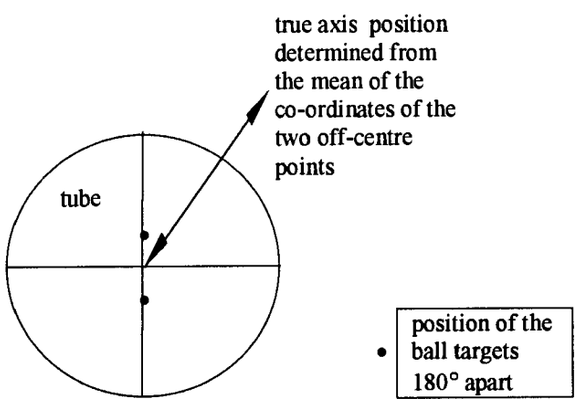

Figure 63 End view of the tube showing the two points used to determine the co-ordinate of a point on the longitudinal axis of the tube

This technique relies on the tube being rotated about its longitudinal axis. In an attempt to ensure that this occurred, a special "cradle" was designed to hold the tube in position. For each set of images, the tube was placed on the cradle by lining up a mark on the tube with the edge of the cradle. The cradle was then oriented to place the tube in the desired pose. Then, as in the previous test, four images were taken of the tube in order to examine the possible effect that intersection angles between the edge bisector planes may have on the final results. The tube was then rotated 180° by lining up marks made on opposite sides of the tube with the edge of the cradle, as shown in Figure 64. A further four images were then captured. Later, while using a bundle adjustment to determine the orientation of the images, the co-ordinates of the two object points which corresponded to each ball's position, before and after rotation, were determined. The two object points which were assumed to lie on the longitudinal axis of the tube were then calculated as the mean of each pair of object co-ordinates.

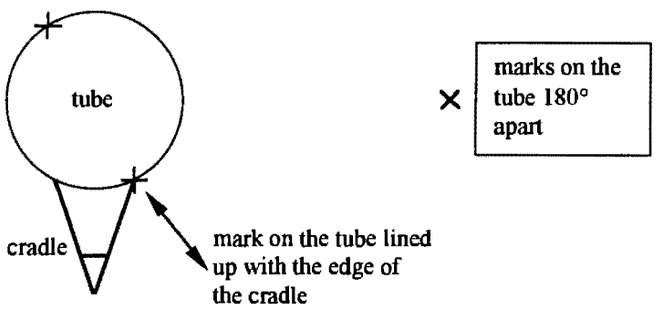

Figure 64 Cross-section through the tube and cradle

Whilst this method offered a potential for greater accuracy than the method used in the first test, there were still some possible sources of error. In particular, the method was prone to inaccuracy introduced when rotating the tube 180°. Whilst every attempt was made to ensure that the marks on opposite sides of the tube were 180° apart, it is unlikely that they were ideally positioned. Furthermore, attempting to line the edge of the cradle up with these marks introduces unavoidable alignment errors. An added source of error was the slight instability and flexibility of the stand holding the cradle itself. It is unlikely that the co-ordinates of the two points intended to define the true axis were any closer than 1-1.5mm from the true axis.

The results of tests using the three silhouette-edge methods are presented in Sections 7.3.1 - 7.3.3. The tables in these sections are similar to those created from the previous test results. Once again the results within each set are ordered by intersection angle between the two axes defining edge bisector planes. The calculated radius as well as the distance, Δpt_1 and Δpt_2, of the two points lying on the "true" axis from the calculated axis are shown. An additional value which is presented, is the angle between the directional vector of the "true" axis and the directional vector of the axis determined using the method being tested. This value gives an indication of the directional deviation of the two axes from one another.

7.3.1 The FEP Method

Some noticeable features of the results obtained using the FEP method are discussed below.

- An examination of the radii displayed in Table 3 (pg. 139) shows that almost all lie within the expected range (42.0±0.2mm). There is no indication that any set, nor any angle within a set, displays significantly different results from those which were expected. As was the case with the test in the previous section, the radii have been determined with a consistently high degree of accuracy.

- The apparent poor results of set 6 seem to imply that something is at fault with the technique when measuring this pose. On closer inspection however, it was found that the standard deviations of the object co-ordinates of pt_1, determined from intersection calculations for this set, are higher than the standard deviations of pt_1 or pt_2 for any other set. Thus it seems likely that the high Δpt_1 values for set 6 can in part be explained by a worse than average object co-ordinate determination for pt_1. This is also evident in the tables depicting the two other methods that are shown later in this section.

- An interesting feature of the table are the poor results produced by calculations which show very small intersection angles (8° and 14°) between the defining edge bisector planes. This is evident in set 2 and 4. In both cases the results produced are significantly different from the others in the set as can be seen by studying their Δpt_1, Δpt_2 and *angular offset* values in relation to others in their set.

- As with the previous test, a direct comparison with the "true" values of the cylinder's position and orientation is difficult since the values of pt_1 and pt_2 each have an uncertainty of ≈1.5mm. The uncertainty in these points leads to an uncertainty of ≈0.25° in the direction of the "true" axis. With the exception of the 14° calculation of set 4, the deviation from the "true" axis of all the results calculated in sets 1-6 fall within this range. The only other exception is the 49° calculation in set 6. However, as was previously stated, pt_1 of this set has a lower accuracy than the axis defining points in the other sets. That most results fall within this range, implies that regardless of whether or not the calculated axis is shifted away from the true axis, the calculated direction of the axis is similar to the true axis direction.

- When examining the Δ values (Δpt_1 and Δpt_2) of the sets, two features are apparent. Not all of the values lie within the expected 1.5mm range, and as depicted by the *range* values, the Δ values within each set are not always consistent. Even if the results of the calculation of the small angles in sets 2 and 4 are ignored, the range of Δpt_1 and Δpt_2 in all sets, except 4 and 5, exceeds 1mm. Thus, even if one were to assume that pt_1 and pt_2 were known to an accuracy of worse than 1.5mm, this would still imply that the method is unable to produce *consistent* positional parameters to greater than 1mm. A study of the intersection angles does not suggest any significant trend in either an increase or decrease in Δpt_1 or Δpt_2 values at angles >20°. Furthermore, when the results of this test are examined in conjunction with the test in the previous section, it is apparent that sets 4 and 5 do not produce significantly superior results to the sets relating to other poses.

It can be concluded that the FEP method is capable of determining the radius and orientation of a cylinder with acceptable accuracy. However, the positional accuracy of the method appears to produce results which have a consistency of no better than 1-1.5mm. This is unacceptable for photogrammetric measurement for which a high accuracy and consistency is required. However, this accuracy and consistency is acceptable for measuring pipes with a similar diameter in an industrial environment. Further tests will be presented in this chapter to establish whether the inconsistency noted is specific to these two initial tests, or whether it is a general weakness in the technique.

Set	Intersection angle (degrees)	Radius (mm)	Δpt1 (mm)	Δpt2 (mm)	Angular offset (degrees)
1	16	42.25	1.23	1.06	0.058
	18	42.13	1.26	1.50	0.04
	21	42.10	1.10	1.81	0.08
	39	42.10	1.19	1.66	0.06
	46	42.06	2.22	1.41	0.10
	56	42.13	1.99	1.83	0.06
	mean	42.13	1.50	1.55	0.06
	range	0.19	1.12	0.77	0.06
2	8	42.21	2.22	2.75	0.15
	22	42.08	1.88	1.88	0.06
	25	42.20	1.55	0.64	0.10
	47	42.11	1.73	1.25	0.06
	70	42.15	1.90	2.50	0.17
	mean	42.15	1.86	1.80	0.11
	range	0.13	0.67	2.11	0.12
3	43	42.04	1.82	0.84	0.11
	44	42.21	1.38	1.46	0.19
	86	42.05	0.58	1.22	0.06
	mean	42.10	1.26	1.17	0.12
	range	0.17	1.24	0.62	0.13
4	14	42.04	3.82	0.96	0.46
	51	42.11	0.95	1.38	0.04
	52	42.16	1.35	1.06	0.05
	mean	42.10	2.04	1.13	0.18
	range	0.12	2.87	0.42	0.42
5	25	42.38	2.46	0.45	0.19
	35	42.07	2.5	0.2	0.22
	60	42.15	2.48	0.36	0.21
	69	42.12	2.36	0.19	0.21
	mean	42.18	2.45	0.30	0.21
	range	0.31	0.14	0.26	0.03
6	30	42.34	2.36	0.76	0.16
	49	42.14	3.59	0.43	0.30
	79	42.10	3.02	0.58	0.23
	mean	42.19	2.99	0.59	0.23
	range	0.24	1.23	0.33	0.14
Overall mean		42.10			
Overall range		0.30			

Table 3 Summary of results using the FEP method: Test B

7.3.2 The TEP Method

The values shown in *italics* in Table 4 are the result of calculations using small intersection angles. Since it has been established that axes defined by planes with a

small intersection angle produce weaker results, the *mean* and *range* values shown below do not include results from these angles.

An examination of the radii show that most values lie within the expected range. The range of radii within each set is greater than in the previous test. This indicates that some consistency in determining the radius is lost by using this method, relative to using the FEP method.

Similar to the previous test, the angular offset of the calculated axis from the "true" axis falls within the expected $\approx 0.25^{\circ}$ for nearly every results. In most cases the range within each set is larger than the ranges determined in the previous test, however, this increase is not significant. As before, it can be stated that the calculated axes directions are similar to the "true" axes directions.

An examination of the Δpt_1 and Δpt_2 values reveals results similar to the those produced by the previous method. Not all of the values lie within the expected range nor are the Δ values within each set consistent. Although the results of this test are similar to those obtained using the previous method, there is a slight increase in the range values within individual sets. This implies that, similar to the radius and directional calculations, this method produces slightly less accurate and less consistent results than the FEP method.

Set	Intersection angle (degrees)	Radius (mm)	Δpt1 (mm)	Δpt2 (mm)	Angular offset (degrees)
1	*8*	*42.47*	*3.00*	*1.89*	*0.13*
	10	*42.07*	*0.28*	*2.24*	*0.19*
	20	42.18	0.90	2.33	0.17
	64	42.19	1.66	1.90	0.02
	77	42.08	1.97	1.37	0.08
	78	42.04	1.07	0.61	0.04
	mean	42.12	1.40	1.55	0.08
	range	0.15	1.07	1.72	0.15
2	13	42.17	1.92	0.19	0.16
	61	42.03	2.44	1.40	0.12
	75	42.24	1.12	1.10	0.02
	mean	42.15	1.83	0.90	0.10
	range	0.21	1.32	1.21	0.14
3	43	41.87	0.60	1.85	0.11
	70	42.24	0.94	1.22	0.13
	70	42.18	1.54	0.30	0.12
	mean	42.10	1.03	1.12	0.12
	range	0.37	0.94	1.55	0.02
4	25	42.10	0.63	1.57	0.09
	73	42.14	1.93	1.36	0.07
	84	42.02	1.33	0.97	0.22
	mean	42.09	1.30	1.30	0.13
	range	0.12	1.30	0.60	0.15
5	30	42.43	2.22	0.78	0.26
	74	41.85	2.50	1.40	0.14
	79	42.32	3.02	0.60	0.23
	mean	42.20	2.58	0.93	0.21
	range	0.58	0.80	0.80	0.12
6	39	42.30	2.47	0.56	0.18
	67	41.92	4.64	0.61	0.38
	76	42.38	2.26	0.56	0.17
	mean	42.20	3.12	0.58	0.24
	range	0.46	2.38	0.05	0.21

Table 4 Summary of results using the TEP method: Test B. The values shown in *italics* are not included in the calculations of the mean and range values

7.3.3 The TSEP Method

The last method to be tested using this set of images was the TSEP method. As was previously explained in Section 5.4.3, the three silhouette edge-planes are used to

create two "virtual" camera positions. At each of these two positions, edge bisector planes are created. The intersection of edge bisector planes from two virtual cameras define the positions of possible axis. For each axis calculated, three intersection angles are shown in Table 5 (pg. 144). Figure 65 describes these angles graphically. The first angle shown in the table is the angle (θ) between the two edge bisector planes which define the axis; this is the same angle as shown in the previous tables. The two other angles (α and β) are the angles formed between the two silhouette edge-planes which create each "virtual" camera position.

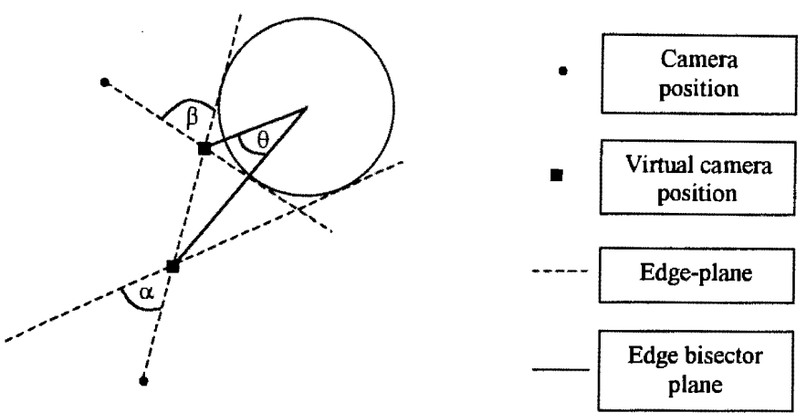

Figure 65 The angle formed between two edge bisector planes is shown as θ and the angles between the intersecting edge-planes at virtual camera positions as α and β

Because the same images were used to test this method as were used to test the FEP method earlier in this chapter, two silhouette edges were visible in each image of the cylinder. This allowed various combinations of edges (i.e. using the left or right silhouette edge of the cylinder in the image) from various images to be tested. As shown in Figure 66, there are two "patterns" that a combination of the three edge-planes can produce. All three edge-planes can be directed towards one side of the cylinder (pattern A) or one edge-plane can be directed towards the side opposite from the other two edge-planes (pattern B).

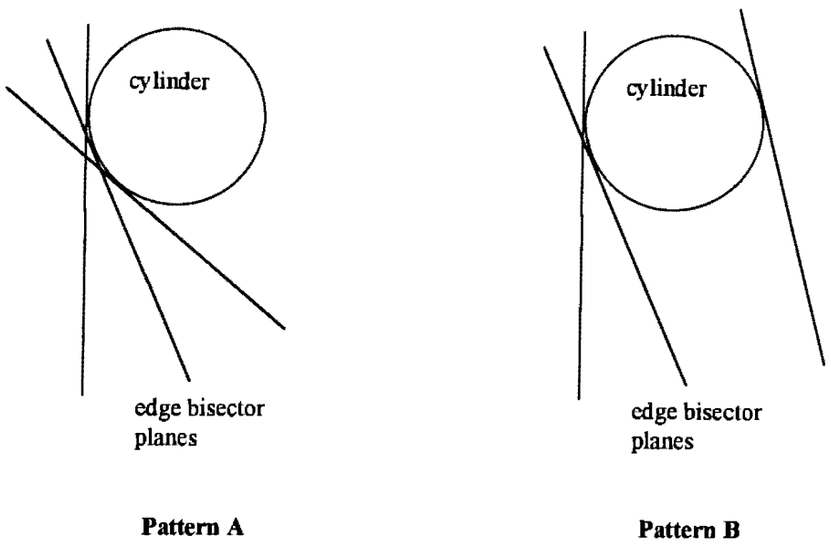

Figure 66 The two possible "patterns" formed by three edge-planes

The algorithm used to determine the cylinder parameters is identical, regardless of which of the two "patterns" are used. However, when a combination of silhouette edges were chosen which resulted in "pattern A" being formed, the results of the tests were significantly poorer that when edge-planes forming "pattern B" were used. Results obtained using combinations of silhouette edges which form "pattern A" are shown in *italics* in Table 5. As with the tests of the other methods, only selected representative results are displayed in this table.

Despite a study of the method's algorithm, as well as the intersection angles formed, it is not clear why poor results occur when using combinations of silhouette edges which form "pattern A". In each case the intersection angle of the defining edge bisector planes is small. However, this in itself does not appear to be the sole cause of the loss of accuracy. Repeated tests have produced results using "pattern B" with similar angles and acceptable results (e.g. the 21° in set 3). Furthermore, there does not appear to be any correlation between the intermediate intersection angles and these poor results. Combinations of edges resulting in "pattern B" produce similar intermediate angles and yet better results.

Set	Intersection angle between the defining edge bisector planes as well as the Intersection angles formed between edge-planes which create the "virtual" camera positions (degrees)			Radius (mm)	Δpt1 (mm)	Δpt2 (mm)	Angular offset (degrees)
1	*8*	*40*	*55*	*37.08*	*5.76*	*4.59*	*0.13*
	64	36	15	43.09	1.40	1.11	0.06
	68	17	60	42.36	3.00	1.94	0.16
	71	15	18	43.09	1.40	1.11	0.06
	82	20	34	42.12	1.91	1.38	0.05
	mean			42.67	1.93	1.39	0.08
	range			0.97	1.60	0.83	0.11
2	*12*	*22*	*46*	*39.10*	*5.45*	*1.7*	*0.39*
	24	18	29	42.24	1.16	1.13	0.02
	79	22	42	42.15	0.50	2.24	0.20
	79	26	46	42.08	2.30	1.33	0.11
	mean			42.16	1.32	1.57	0.11
	range			0.16	1.80	1.11	0.18
3	*21*	*44*	*86*	*40.78*	*4.10*	*1.72*	*0.46*
	21	43	86	42.39	2.60	1.02	0.33
	66	41	43	41.56	0.55	0.94	0.14
	70	42	47	42.23	0.96	0.70	0.05
	mean			42.06	1.37	0.89	0.17
	range			0.83	2.05	0.32	0.28
4	*18*	*51*	*15*	*45.12*	*24.00*	*12.00*	*3.57*
	80	36	56	42.24	2.09	1.32	0.07
	84	40	50	41.98	1.90	1.14	0.16
	mean			42.11	2.00	1.23	0.12
	range			0.26	0.19	0.18	0.09
5	*17*	*25*	*60*	*41.66*	*2.92*	*1.82*	*0.29*
	75	34	64	42.58	2.61	1.46	0.11
	79	34	56	42.58	2.42	1.25	0.34
	79	38	60	42.28	2.76	1.04	0.16
	mean			42.48	2.60	1.25	0.20
	range			0.30	0.34	0.42	0.23
6	15	49	79	41.88	2.5	1.19	0.26
	24	*79*	*30*	*40.52*	*5.50*	*0.61*	*0.48*
	73	48	82	42.74	4.99	0.62	0.42
	76	52	79	42.18	3.67	0.59	0.29
	76	49	76	42.38	2.50	0.20	0.22
	mean			42.30	3.42	0.65	0.30
	range			0.86	2.49	0.99	0.20

Table 5 Summary of results using the TSEP method: Test B. The values shown in *italics* are not included in the calculations of the mean and range values.

Although it is not fully understood why the stated effect occurs, it is simple to avoid its occurrence by ensuring that only combinations of edges which form "pattern B" are used. The *mean* and *range* values in the table above are calculated using only "pattern B" combinations of edge-planes.

An examination of the radii produced from "pattern B" edge-plane combinations reveals, that many do not fall within the expected range (42.0±0.2mm). The *mean* and *range* of radii within some sets are greater than in the results of tests using the previous two methods. However, in all cases the calculated radius falls within the range 42.2±0.9mm. This translates into an inaccuracy of no more than 1.8mm for the diameter of the cylinder.

Most of the angular offsets fall within the expected ≈0.25° range. Those which do not fall within this range all deviate from the "true" axis direction by less than 0.5°.

As was the case with the tests of the previous methods, the Δpt_1 and Δpt_2 values exceed the expected 1.5mm range. In almost all cases these values were less than 3mm indicating that the calculated axis position was no more than 3mm away from the "true" axis. Although the Δpt_1 values of set 6 are higher than average, they are similar to the mean values of set 6 in the tests using the previous methods.

Once again the *range* values of Δpt_1 and Δpt_2 indicate that the position of the cylinder is not being determined consistently. However, in most cases the range of Δpt_1 and Δpt_2 values is below 2mm which is quite sufficient for the purpose of measuring pipes in industrial plants.

7.3.4 Conclusions

The graphs below allow an easy comparison between the *mean* and *range* values calculated for each cylinder pose by the three methods (FEP, TEP, TSEP). The graphs

show the *mean* and *range* values of each of the four calculated values (*radius, angular offset, Δpt_1, Δpt_2*) in millimetres and degrees, for each set of images within each method[3].

RADIUS

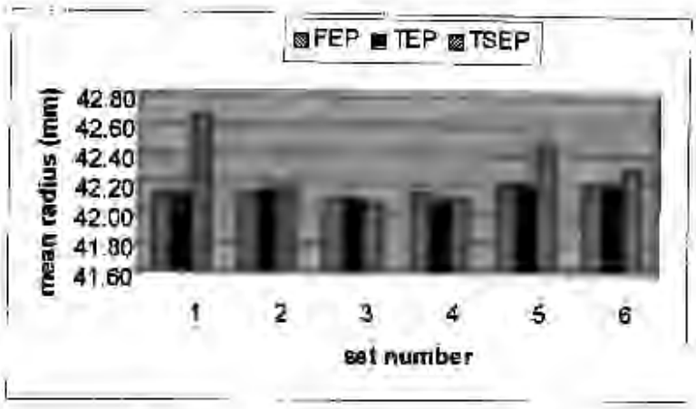

Figure 67 Comparison of the *mean* radius values obtained using each of the three methods

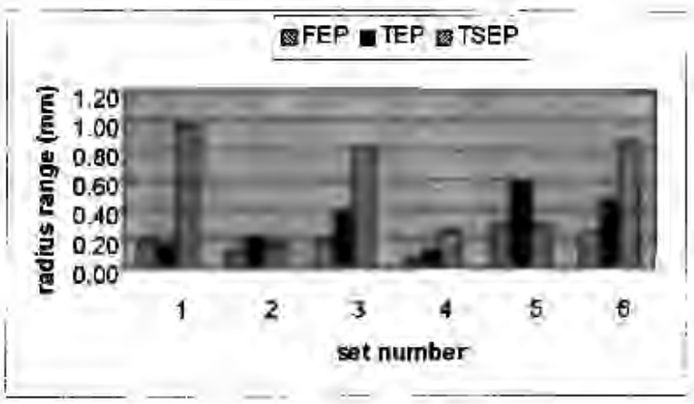

Figure 68 Comparison of the *range* of the radius values obtained using each of the three methods

[3] Due to a shortcoming of the word processor used, the graph axis on the following pages which should have been labeled Δpt_1 and Δpt_2 have instead been labeled as *(delta)pt1* and *(delta)pt2*.

show the *mean* and *range* values of each of the four calculated values (*radius, angular offset, Δpt_1, Δpt_2*) in millimetres and degrees, for each set of images within each method[9].

RADIUS

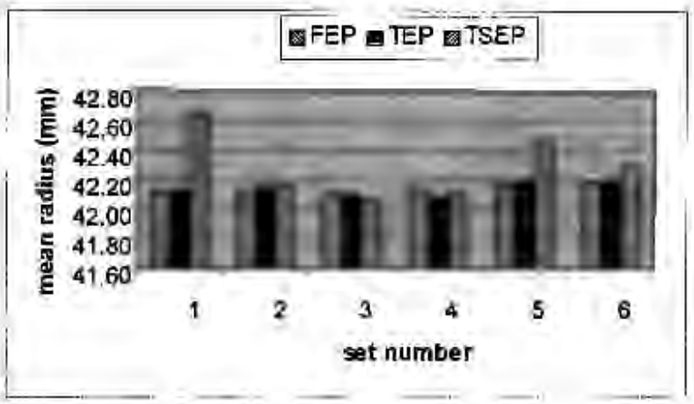

Figure 67 Comparison of the *mean* radius values obtained using each of the three methods

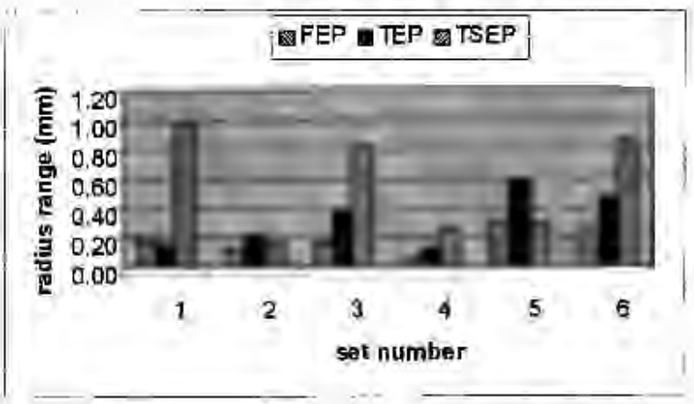

Figure 68 Comparison of the *range* of the radius values obtained using each of the three methods

[9] Due to a shortcoming of the word processor used, the graph axis on the following pages which should have been labeled Δpt_1 and Δpt_2 have instead been labeled as *(delta)pt1* and *(delta)pt2*.

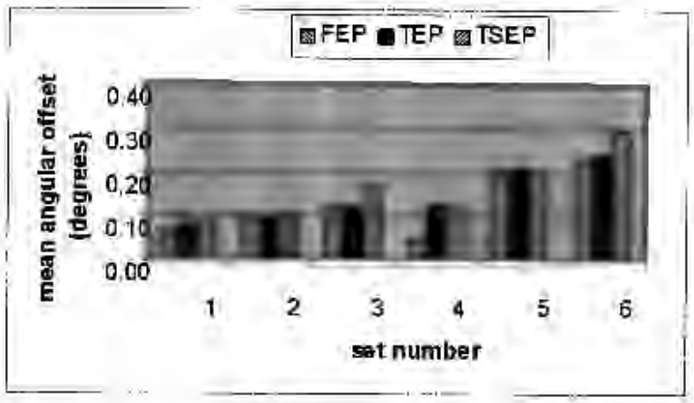

Figure 69 Comparison of the *mean* angular offset values obtained using each of the three methods

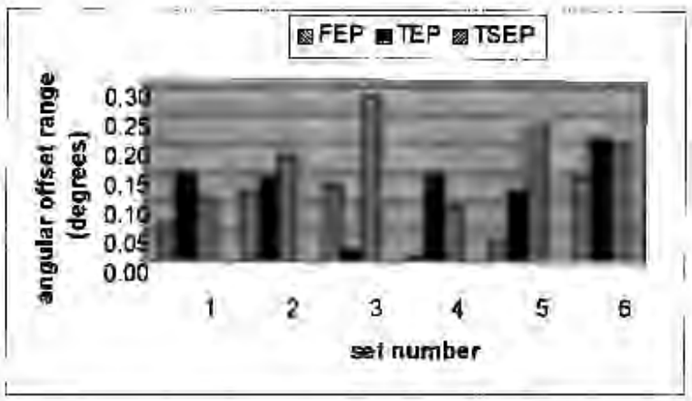

Figure 70 Comparison of the *range* of angular offset values obtained using each of the three methods

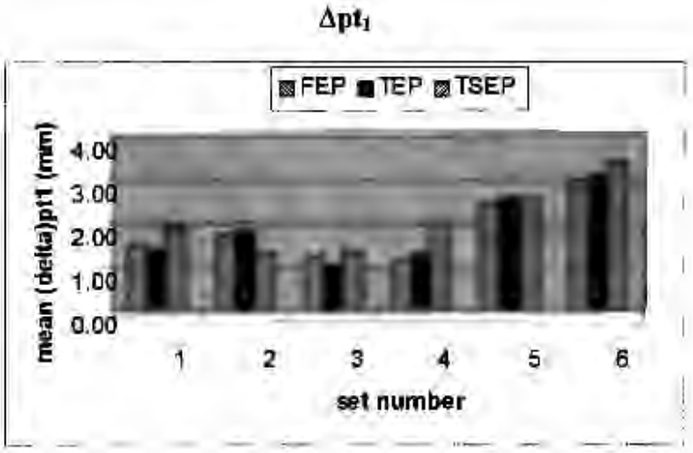

Figure 71 Comparison of the *mean* Δpt_1 values obtained using each of the three methods

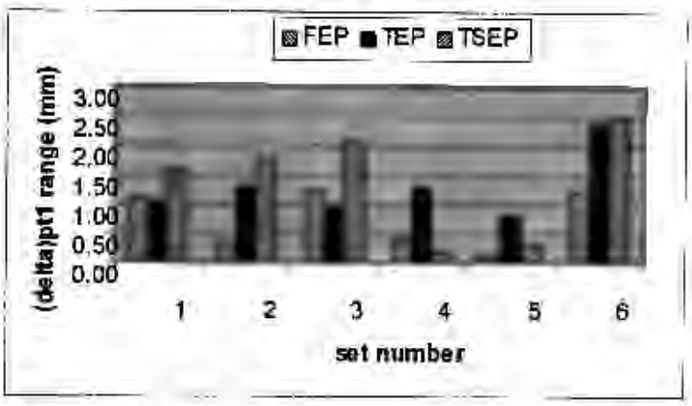

Figure 73 Comparison of the *range* of Δpt_1 values obtained using each of the three methods

Δpt_2

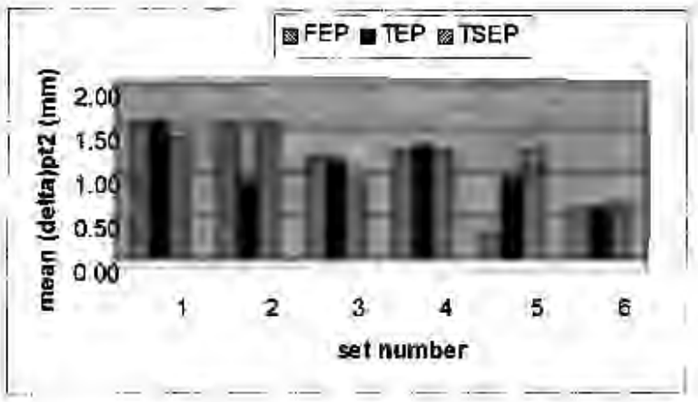

Figure 73 Comparison of the *mean* Δpt_2 values obtained using each of the three methods

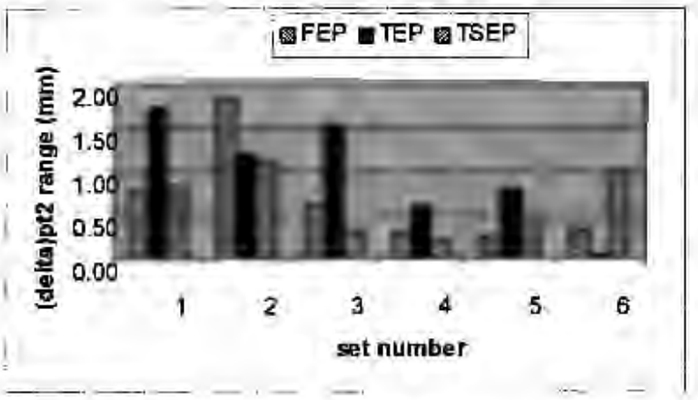

Figure 74 Comparison of the *range* of Δpt_2 values obtained using each of the three methods

Although it is not uniform, a steady decline in the accuracy of the radius, position and orientation of the cylinder can be seen by examining the *mean* and *range* values of the three methods. The FEP method produces the most accurate and consistent results whilst the TSEP method produces the least accurate and least consistent results. Furthermore, both these graphs and the results shown in the previous tables in this section, do not indicate that the pose of the cylinder has a *significant* effect on the accuracy of the results. There does, however, appear to be evidence that calculations resulting in very small intersection angles (<15°) between the defining edge bisector planes, produce less accurate results than those combinations of images resulting in larger angles. It can also be noted that the "pattern" formed by the choice of edge-planes used in the TSEP method has a significant effect on the results.

As was stated previously, these results imply that the techniques may not be suitable in their present form for digital photogrammetry requiring high (sub-millimetre) accuracy. However, the FEP and TEP methods produce results which can provide accuracies which are sufficient for measuring pipes in industrial plants. The TSEP method is also capable of producing acceptable results providing a "pattern B" combination of edge-planes is used. An improvement in the accuracy of the results of all three of the methods can be expected if images are used with a resolution greater than 1524x1012. However, this hypothesis has not been tested.

7.4 Examination of the Consistency with which the Relative Positions of Cylinders can be Calculated using the FEP Method

A test was performed in order to determine the consistency with which the position of cylinders could be calculated in relation to one another. This test differs from the tests in the previous sections in that the overall positional accuracy of each cylinder's parameters is not examined. Instead, the position of two cylinders relative to each other is examined by calculating the shortest distance between the two axes.

This test was motivated by the fact that although the absolute accuracy of pipes in a plant layout is important, their relative position is perhaps of greater importance. This is true because pipes in a plant are not single entities, but are instead interconnected in a functional network. The pipes must fit together in the final CAD model, even if this means the calculated positions of pipes must be manipulated slightly to ensure that this occurs. As a result of this requirement, PDS software packages are capable of manipulating the positions of pipes to ensure that pipes which are known to connect do in fact do so in the final model. The final positions of two pipes which are know to connect may be determined by calculating the best-fitting intersection of the two pipes, whilst at the same time ensuring that functional constraints specific to the pipe network are not violated. Consequently, it is useful to examine how consistently the silhouette technique for measuring pipe positions can determine the positions of pipes relative to one another.

Although the data presented in the previous two sections could be used to examine the relative positional accuracy between cylinders, it was more convenient to perform a test which explicitly examined this particular aspect. Only the FEP method is tested since the relative strengths and weaknesses of the three silhouette-edge methods have already been established in the previous sections (see especially Section 7.3.4).

The test was conducted in a similar manner to the tests in the previous sections. Two scenarios were created. In both cases the two tubes were placed in front of a control frame which was later used to orient the images. In the first scenario the tubes were positioned some distance apart and with poses such that, if they were real pipes, they would not be expected to intersect (see Figure 75). In the second scenario, the tubes were positioned in such a manner that they were touching and approximately orthogonal to one another. This was designed to simulate two intersecting pipes (Figure 76). It should be noted however, that no attempt was made to ensure that the axes of the two cylinders did in fact intersect precisely and it is likely that whilst the two tubes did physically touch, their axes did not lie in the same plane.

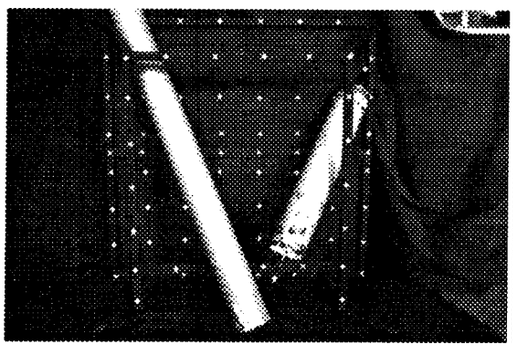

Figure 75 Arrangement of "pipes" passing close to one another

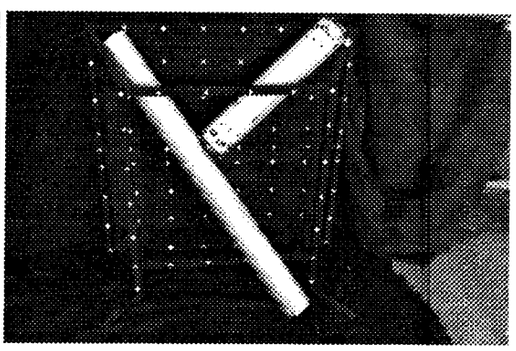

Figure 76 Arrangement of "pipes" intersecting one another at approximately 90°

For each scenario, six images were captured from various camera positions. The images were each provisionally oriented by measuring the image co-ordinates of control points and applying a DLT to the results. The final exterior orientation of each image was determined by applying a bundle adjustment to all six images simultaneously. The parameters of the edge lines of each tube in each image were then extracted. Finally, various combinations of images and their edge lines were used to calculate the position of the tubes. For each combination of images, the shortest distance between the resultant axes of the two tubes were determined. This distance was used as a measure of the relative position of the two tubes. By examining how this value differs between combinations of images, some conclusions can be drawn regarding the consistency with which the method determines the relative position of cylinders.

Two tables, one for each scenario, are presented below. Table 6 presents results relating to the scenario shown in Figure 75, and the Table 7 relates to the scenario depicted in Figure 76. Each row in a table presents the results obtained using the silhouette edge data available within two images. Results from various combinations of pairs of the six images within each scenario are presented.

The first two columns in the tables display the intersection angles (in degrees) between the edge-plane bisectors defining each of the two tube's axes (tube "*A*" and

tube "*B*"). The third column displays the distance (in mm) calculated between the two tube's axes for that combination of images. The *range* value is the difference between the largest and smallest value in each data set. As has already been determined from previous tests, combinations of edge-planes resulting in low intersection angles (<15°) between the defining edge bisector planes may produce less reliable results. This factor is again present in the results of this test, as can be seen in Table 6 below. However, as in previous tests, the results of these combinations have been shown in *italics* and are not included in the statistics presented in the two tables.

Intersection angle (degrees) (Tube A)	**Intersection angle (degrees) (Tube B)**	**Shortest distance between axis A and axis B (mm)**
3	*5*	*16.11*
4	*4*	*21.62*
6	*2*	*18.91*
29	33	19.05
36	35	18.83
37	41	17.31
37	41	17.64
37	42	18.37
40	37	17.11
70	71	18.17
76	73	18.07
80	77	18.28
	mean	18.09
	std. deviation	0.65
	range	1.94

Table 6 Comparison of the distance between two axes calculated from various combinations of images (based on the arrangement of cylinders shown in *Figure 75*). The values shown in *italics* are not included in the calculations of the mean and range values.

Intersection angle (degrees) (Tube A)	**Intersection angle (degrees) (Tube B)**	**Shortest distance between axis A and axis B (mm)**
1	*6*	*8.61*
8	*15*	*8.20*
9	*4*	*1.17*
17	56	9.39
24	41	9.47
25	60	9.17
33	44	8.77
46	53	10.25
47	47	10.29
53	38	10.31
54	32	10.45
71	86	10.07
72	88	10.10
80	82	9.63
81	88	9.58
	mean	9.79
	std. deviation	0.53
	range	1.67

Table 7 Comparison of the distance between two axes calculated from various combinations of images (based on the arrangement of cylinders shown in *Figure 76*). The values shown in *italics* are not included in the calculations of the mean and range values.

Similar conclusions can be drawn from each of the two sets of data in the tables above. In both cases the *standard deviation* is less than 0.65mm. This implies that, at least for these two tests, in the majority of cases the distance between the calculated axes of the two cylinders is likely to lie within 0.65mm of the most probable true distance between the two cylinders. This consistency in determining the cylinders positions with respect to one another, is well within the limits required by a PDS when measuring pipes in industrial plants.

One other important feature which can be seen by examining the results presented in Table 6 and Table 7, are the relatively lower *standard deviation* and *range* values of

the results presented in Table 7. The most likely explanation for these improved results is that better lighting was used when capturing the second set of images. The lighting was directed specifically so as to attempt to ensure that the silhouette edges on the resultant images would be as distinct as possible. This in turn ensured that the edge lines which were extracted from the images were as truly representative of the silhouette edges of the tubes as possible. Although the difference between the two sets of results is not great, the improvement in the second set of results does show the importance that the role of lighting plays in the silhouette techniques. Obviously, unless the edges of the cylinder are defined well, inaccurate results may be calculated. In particular, when lighting conditions cause silhouette edges to fall in areas of shadow, care must be taken to ensure that the edge line extracted is that of the silhouette edge itself and not instead of the line defining the transition between light and shadow. Problems associated with poorly defined edges are one of the most likely causes of error associated with the silhouette edge techniques. This problem almost certainly accounts for some of the minor (1-2mm) discrepancies shown in the previous tests.

7.5 Calculation of the Parameters of a Medium Bore Cylinder

The tests in Sections 7.2-0 were conducted using a cylinder with a diameter similar to that of a small bore pipe. The test in this section evaluates the silhouette-edge methods' abilities to measure a cylinder representing a pipe with a bore greater than that used in the previous tests. A cylindrical concrete pillar, wrapped in a layer of metal sheeting, with a radius of 190±2mm was selected as representative of a pipe with a medium bore.

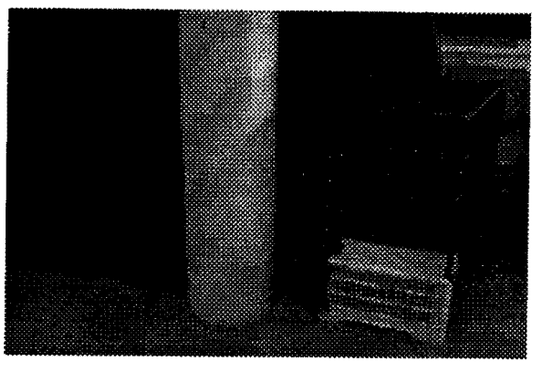

Figure 77 The concrete pillar used to represent a pipe with a radius of 190mm

In order to allow a comparison with the axis parameters determined using the silhouette-edge methods, it was necessary to establish the parameters of the cylinder using a method independent of those being tested. A conventional surveying technique using theodolites was chosen to provide an independent measurement of the cylinder.

Three permanent laboratory theodolite stations were chosen situated around the cylinder. The object co-ordinates of these stations were known from previous measurements. The objective was to define the position and direction of the cylinder by the co-ordinates of two points on its longitudinal axis. Two circumference lines were visible on the cylinder. At each set-up position, horizontal and vertical angles were measured to either side of the cylinder on each circumference line. At each set-up, the mean of the horizontal angles to the left and right side of the cylinder along a circumference line was calculated. This results in an observation ray which passes through the longitudinal axis of the cylinder. In this way, two observation rays passing through the axis of the cylinder can be determined from each set-up. This process was repeated at each of the three theodolite set-up positions, resulting in three observation rays to each of two points lying on the cylinder axis. Simple intersection calculations determine the object co-ordinates of these two points which then define the "true" axis of the cylinder. The two points lay approximately 1.2m apart. It should be noted however, that the calculated "true" axis co-ordinates of the cylinder may differ from the actual true axis position for a variety of reasons, including:

- lack of true circularity of the cylinder
- deviation of the assumed circumference lines from the true circumference
- observational inaccuracies.

Thus, it is unlikely that the "true" axis co-ordinates were defined to an accuracy of greater than a few millimetres.

As was the case in previous tests, a control frame was used to provide the information required to orient the captured images. In order to make any meaningful comparison between the cylinder parameters determined using the silhouette methods and the parameters determined using theodolite observations, it was necessary to ensure that the control frame and the "true" co-ordinates defining the axis were in the same co-ordinate system. At each theodolite station, observations were made to four circular control points on the control frame. Horizontal and vertical observations to the centre of each target were determined by taking the mean of observations to either side and the top and bottom of the target. This eliminated to problem of attempting to judge the centre of the target. The object co-ordinates of these four points were determined via intersection from the three sets of theodolite observations. Using a three dimensional transformation and the four points common to both co-ordinate systems, the "true" axis co-ordinates of the pillar were transformed into the same co-ordinate system as that of the targets on the control frame.

In total, six images of the pillar were captured from various camera positions. The images were captured in two strips, each of three images. The camera/pillar configuration is shown in Figure 78. The camera positions were approximately 2m from the pillar. There was an approximately 85° angle between the pillar, the first and the last image in each strip. The difference in height of the two strips was approximately 0.5m.

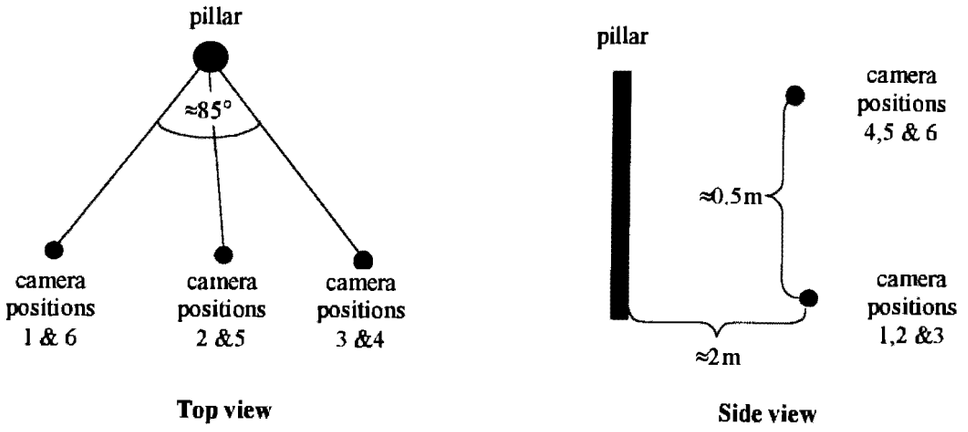

Figure 78 Camera positions for the test involving a medium bore cylinder

As was the case in previous test, each image was individually provisionally oriented using observations to the targets on the control frame which were visible in the image. The observations and provisional orientation of all six images were then input into a bundle adjustment and the final orientations of the images determined simultaneously.

Combinations of silhouette edge-planes in various images were used to determine the parameters of the cylinder using each of the three silhouette-edge methods. The results of the calculations are presented in Table 8-Table 10 below. The layout of these tables is the same as those presented in previous sections. The *intersection angle* is the angle (in degrees) formed between the two edge bisector planes which define the longitudinal axis of the cylinder. Δpt_1 and Δpt_2 are the shortest distances (in mm) from the two points defining the "true" axis of the cylinder and the axis as determined using the silhouette-edge methods. The *angular offset* is the difference (in degrees) between the direction of the "true" axis and the calculated axis. The *range* value is the difference between the largest and smallest value in a data set. Once again, those results presented in *italics* have not been included in the calculation of the *mean* and *range* values.

7.5.1 The FEP Method

The first three results shown in *italics* in Table 8 are the results of combinations of images resulting in very small intersection angles. These results arise from the combination of images from camera positions 1 & 6, 2 & 5 and 3 & 4 respectively (see Figure 78). Since each pair of camera positions is separated mainly in the vertical axis, and since the pillar's axis is also predominantly vertical, it is not surprising that these combinations of images give poor results. However, whereas their Δpt_1 and Δpt_2 values are poor, their radii are acceptable.

An examination of the radii of the rest of the results in the table, shows that all lie well within the expected range (±2mm) of the true radius. The Δpt_1 and Δpt_2 values are acceptable and lie within the range with which the "true" axis co-ordinates could have been expected to be measured. The *angular offset* is also acceptable for all values.

Intersection angle (degrees)	**Radius (mm)**	**Δpt1 (mm)**	**Δpt2 (mm)**	**Angular offset (degrees)**
0.20	*191.20*	*27.58*	*2.71*	*1.16*
0.50	*190.76*	*43.89*	*33.56*	*3.62*
5	*188.71*	*9.73*	*11.42*	*0.09*
30	190.54	1.53	2.05	0.03
30	190.56	1.65	2.05	0.02
30	190.59	0.82	2.61	0.09
30	190.62	0.90	2.61	0.08
51	189.71	0.54	0.93	0.04
51	189.73	0.43	0.93	0.04
57	189.93	1.01	0.41	0.03
81	190.12	1.15	1.41	0.04
82	190.17	0.76	1.68	0.05
86	190.38	1.48	1.22	0.03
87	190.44	1.23	1.51	0.04
mean	190.25	1.05	1.58	0.05
range	0.90	1.22	2.20	0.07

Table 8 Summary of results using the FEP method: Medium bore cylinder test. The values shown in *italics* are not included in the calculations of the mean and range values.

7.5.2 The TEP Method

The results shown in *italics* in Table 9, are the results of combinations of images resulting in small intersection angles (<15°). While these combinations produce Δpt_1 and Δpt_2 values which are poorer than those of the other results in this data set, their radii are once again acceptable.

The majority of the rest of the image combinations shown in the table produce acceptable results in all categories measured. The 0.14° *angular offset* determined for the last two combinations presented, is disproportionate to the other results in the data set. However, no apparent reason for this could be determined.

Intersection angle (degrees)	**Radius (mm)**	**Δpt1 (mm)**	**Δpt2 (mm)**	**Angular offset (degrees)**
14	*190.31*	*4.33*	*2.47*	*0.09*
15	*191.16*	*2.88*	*3.59*	*0.04*
26	189.44	1.12	1.90	0.05
28	190.01	1.06	0.21	0.04
41	189.52	2.36	2.97	0.04
43	190.81	1.23	1.17	0.02
45	189.28	0.93	0.61	0.06
51	190.80	2.10	1.75	0.06
60	189.27	0.38	0.78	0.04
67	189.95	0.87	0.59	0.02
70	190.08	1.57	1.51	0.14
80	190.78	2.20	1.70	0.14
mean	189.99	1.38	1.32	0.06
range	1.54	1.97	2.76	0.13

Table 9 Summary of results using the TEP method: Medium bore cylinder test. The values shown in *italics* are not included in the calculations of the mean and range values.

7.5.3 The TSEP Method

The values shown in *italics* in Table 10 are as a result of combinations of images whose silhouette edges result in edge-planes which form "pattern A". The two possible "patterns", "pattern A" and "pattern B", formed by three edge-planes directed

to the same cylinder, are described previously in Section 7.3.3 and shown in Figure 66. The remaining results displayed here were calculated from a combination of silhouette edges forming "pattern B".

Intersection angle between the defining edge bisector planes as well as the intersection angles formed between edge-planes which create the "virtual" camera positions (degrees)			Radius (mm)	Δpt1 (mm)	Δpt2 (mm)	Angular offset (degrees)
15	*81*	*51*	*189.35*	*1.98*	*2.21*	*0.19*
15	*81*	*52*	*189.71*	*2.80*	*2.07*	*0.23*
28	*86*	*29*	*188.97*	*1.97*	*2.56*	*0.21*
42	57	39	189.72	0.99	0.88	0.03
42	14	81	190.13	0.93	0.97	0.07
43	*57*	*30*	*194.77*	*6.73*	*3.49*	*0.15*
52	56	20	191.14	2.52	1.48	0.05
53	42	30	188.39	4.08	4.62	0.03
57	87	20	190.72	1.62	0.98	0.04
67	86	40	189.84	1.05	0.58	0.05
70	84	57	189.72	0.99	0.88	0.03
79	72	51	191.13	1.80	1.51	0.02
79	81	60	190.55	1.83	2.71	0.05
mean			190.15	1.76	1.62	0.04
range			2.75	3.15	4.04	0.05

Table 10 Summary of results using the TSEP method: Medium bore cylinder test. The values shown in *italics* are not included in the calculations of the mean and range values.

As was the case in tests in the previous sections, the results of "pattern A" combinations of edge-planes are poorer in every category than those obtained using "pattern B" combinations of edge-planes.

Results of "pattern B" combinations produce radii and *angular offset* values which all fall within the acceptable range of values. The majority of Δpt_1 and Δpt_2 values are also acceptable.

The combination of images which produce the 53° intersection angle, results in Δpt_1 and Δpt_2 values which are somewhat greater than the others in the data set. However, since the *angular offset* of this particular combination is acceptable, and since the radius is smaller than the others in the data set, it appears likely that this comparatively poor combination is as a result of a slight misidentification of the silhouette edges in the images rather than a fundamental problem with the technique.

7.5.4 Conclusions

It is noticeable that the results of the three different silhouette-edge methods exhibit a similar trend to that seen in the tests in Section 7.3. Once again the majority of *range* values, which are an indication of the consistency of results in a data set, increases from the FEP method which has the lowest *range* values, to the TSEP method which has the highest *range* values.

There is however, far less difference in the accuracy of results obtained between the three different silhouette-edge methods in this set of tests than was evident in the tests in Section 7.3. The most likely explanation for this improvement in accuracy is that the silhouette edges in the images used in this test were more clearly defined than in previous tests. This once again emphasises the importance of suitably lighting the cylinder, allowing the edge detection and line extraction processes to produce edge lines in the images which accurately represent the silhouette edges of the cylinder.

This test confirmed that the silhouette edge techniques are able to determine the defining parameters of the axis of a medium bore cylinder with at least the same degree of accuracy as that of a cylinder with a smaller radius. Furthermore, both the absolute and relative accuracies with which the three methods could determine the parameters of pipes in an industrial plant, would be sufficient for input into a PDS.

8 THEORETICAL ERROR ANALYSIS OF THE FOUR-EDGE-PLANES METHOD

The previous chapter presented test cases in which the silhouette-edge methods were used to determine the position of a cylinder axis. The results presented in that chapter indicate that the silhouette-edge methods are capable of repeatedly measuring the radius, position and orientation of the cylinder to an accuracy which would be acceptable for measuring pipes in industrial plants. However, it is necessary to attempt to confirm this conclusion by carrying out an error analysis of the methods. The FEP method was chosen as the method to analyse since it is the simplest of the methods to analyse.

There were two objectives to calculating the standard deviations of the unknowns of this method:

- to determine the absolute accuracy to which the unknown parameters can be measured
- to determine whether the cylinder's position relative to the cameras has a significant effect on the absolute accuracy of the method

The final output of the FEP method are the parameters of two planes (A_1, B_1, C_1, D_1, A_2, B_2, C_2, D_2). However, the magnitude of these parameters differs greatly depending on the orientation of the planes they define. This makes comparison of standard deviations between different planes difficult and nearly meaningless. It is far more meaningful to compare the standard deviations of object co-ordinates. For this reason, the co-ordinates of points on the cylinder axis defined by these plane parameters were determined and the standard deviations of these points evaluated. Three points were determined on the axis. The first point was calculated by holding a chosen X ordinate fixed and solving for the Y and Z ordinates. The second and third points were

similarly calculated using fixed, chosen Y and Z ordinates respectively. The equations used to determine these three points are given by:

$$\begin{vmatrix} Y \\ Z \end{vmatrix} = \begin{vmatrix} B_1 & C_1 \\ B_2 & C_2 \end{vmatrix}^{-1} \begin{vmatrix} -D_1 - A_1 X \\ -D_2 - A_2 X \end{vmatrix}$$

$$\begin{vmatrix} X \\ Z \end{vmatrix} = \begin{vmatrix} A_1 & C_1 \\ A_2 & C_2 \end{vmatrix}^{-1} \begin{vmatrix} -D_1 - B_1 Y \\ -D_2 - B_2 Y \end{vmatrix}$$

$$\begin{vmatrix} X \\ Y \end{vmatrix} = \begin{vmatrix} A_1 & B_1 \\ A_2 & B_2 \end{vmatrix}^{-1} \begin{vmatrix} -D_1 - C_1 Z \\ -D_2 - C_2 Z \end{vmatrix}$$

Equation 76

where:

A_1, B_1, C_1, D_1 and A_2, B_2, C_2, D_2 are the parameters of the two edge-planes

It was desirable that the three points determined on the cylinder axis be within the approximate section of the cylinder visible in the images, since this would produce results more relevant to future possible calculations. The same images that were used in Section 7.3 were used for this test. From previous calculations, the position of a point within the field of view of the camera and known to lie approximately on the axis, was known. The ordinates of this point were used to determine the object co-ordinates of the three required points.

The FEP method uses no redundant observations; it determines a unique solution using the minimum number of observations required. Since the final result is not based on a best-fit of the observations used, it is not possible to calculate a value for the internal accuracy of the method. Only the absolute accuracy of the method, a measure of how accurately the final values have been determined in object space, can be calculated. The determination of the absolute accuracy must take into account the accuracy of the input data. The standard deviations of the co-ordinates of the final

points can be determined by examining how the effects of the standard deviations of the input data propagate through the method.

This can be achieved by applying the general law of error propagation for correlated observations in non-linear form, as stated below.

Given r number of functions

$$\begin{aligned} &F_1(l_1, l_2, \ldots, l_n) \\ &F_2(l_1, l_2, \ldots, l_n) \\ &\vdots \\ &F_r(l_1, l_2, \ldots, l_n) \end{aligned}$$

Equation 77

containing the set of observations (l_i)

$$l^T = (l_1, l_2, \ldots, l_n)$$

Equation 78

which have the variance-covariance matrix

$$\sum_{ll} = \begin{vmatrix} \sigma_1^2 & \sigma_{12} & \cdots & \sigma_{1n} \\ \sigma_{21} & \sigma_2^2 & \cdots & \sigma_{2n} \\ \vdots & \vdots & \vdots & \vdots \\ \sigma_{n1} & \sigma_{n2} & \cdots & \sigma_n^2 \end{vmatrix}$$

Equation 79

, the variance-covariance matrix $\sum_F$ can be determined.

In order to determine $\sum_F$, the functions F_r are linearized by means of a Taylor series expansion, in a form where higher order terms are ignored, resulting in:

$$\begin{aligned} F_1 &= f_{10} + f_{11}l_1 + f_{12}l_2 + \ldots + f_{1n}l_n \\ F_2 &= f_{20} + f_{21}l_1 + f_{22}l_2 + \ldots + f_{2n}l_n \\ &\vdots \\ F_r &= f_{r0} + f_{r1}l_1 + f_{r2}l_2 + \ldots + f_{rn}l_n \end{aligned}$$

Equation 80

in which

$$f_{ri} = \frac{\partial F_r}{\partial l_i}$$

Equation 81

Extracting only partial differentials from Equation 80 leads to:

$$F = \begin{vmatrix} f_{11} & f_{12} & \cdots & f_{1n} \\ f_{21} & f_{22} & \cdots & f_{2n} \\ \vdots & \vdots & \vdots & \vdots \\ f_{r1} & f_{r2} & \cdots & f_{rn} \end{vmatrix}$$

Equation 82

Finally, this leads to the variance-covariance matrix $\sum_F$ with dimensions $r \times r$, where r is the number of functions in Equation 77. The variance of the unknowns can be read from the diagonal terms of $\sum_F$ and from this the standard deviations can be determined. The off-diagonal terms indicate co-variances.

$$\sum_F = F \sum_{ll} F^T$$

Equation 83

which is equivalent to:

$$\sum_F = \begin{vmatrix} \sigma_1^2 & & & \\ & \sigma_2^2 & & \\ & & \ddots & \\ & & & \sigma_r^2 \end{vmatrix}$$

Equation 84

The law of error propagation can be applied at each step in the cylinder measurement method. In theory, the errors associated with determining the parameters of the edge line on the image which represents the cylinder's silhouette edge, as well as the two subsequent image points calculated on the edge line, should be determined. However, while these errors can be calculated, the accuracy with which the edge detector can detect the silhouette edge is of far greater significance.

Certain edge detectors are capable of detecting an edge to sub-pixel accuracy. However, this accuracy is of little use unless the silhouette edge itself is clearly defined in the image. How clearly an edge is defined in an image differs between images and is dependent on, amongst other factors, the lighting conditions. The theory of error propagation cannot be used to determine how well a silhouette edge is defined in an image. As a result, a decision was taken to assume that the parameters of the best-fit edge line and therefore the image co-ordinates of the two points calculated on the line, were error free. Only the effect that the standard deviations of the interior and exterior orientations have on the final results is evaluated.

The calculation of the propagation of errors through the FEP method can be sub-divided into four consecutive steps. The steps determine:

1. The object space co-ordinates of each of the two image points on the edge line.

2. The parameters of the edge-plane through three points in object space (the two points calculated in the previous step and the PC of the camera).

3. The parameters of the edge bisector plane from each of the two camera positions.

4. The object co-ordinates of three points on the cylinder axis defined by the intersection of the two edge bisector planes.

As a practical example of the application of the law of error propagation, the process is described using step 1 of the list above.

The observations required for this step are

$$l^T = \left(X_C, Y_C, Z_C, \omega, \phi, \kappa, x_p, y_p, c, x_i, y_i\right)$$

Equation 85

where:

X_C, Y_C, Z_C	are the co-ordinates of the perspective centre of the camera
ω, ϕ, κ	are the rotations of the camera about the X,Y and Z axis
x_p, y_p	are the image co-ordinates of principal point
c	is the principal distance of the camera
x_i, y_i	are the co-ordinates of the image point on the best-fit line

The pre-determined standard deviations of the observations form the variance-covariance matrix (Σ_{ll}) shown in Equation 86 below. These standard deviations can be obtained from the output of a bundle adjustment used to orient the images. The off-diagonal terms are the co-variances and can be used if known. However, in this case they were assumed to be zero. For reasons previously explained, the standard deviations of x_i and y_i were set to zero.

$$\sum_{ll} = \begin{bmatrix} \sigma^2_{X_C} & & & & & & & & & & \\ & \sigma^2_{Y_C} & & & & & & & \text{covariances} & & \\ & & \sigma^2_{Z_C} & & & & & & & & \\ & & & \sigma^2_{\omega} & & & & & & & \\ & & & & \sigma^2_{\phi} & & & & & & \\ & & & & & \sigma^2_{\kappa} & & & & & \\ & & & & & & \sigma^2_{x_p} & & & & \\ & & & & & & & \sigma^2_{y_p} & & & \\ & & & & & & & & \sigma^2_{c} & & \\ & & & & & & & & & \sigma^2_{x_i} & \\ & & & & & & & & & & \sigma^2_{y_i} \\ & & & & & & & & & & \end{bmatrix}$$

covariances

Equation 86

The functions relating to this step are:

$$F_1 = X_i = X_C + m_{11}(x_i - x_p) + m_{21}(y_i - y_p) + m_{31}c$$
$$F_2 = Y_i = Y_C + m_{12}(x_i - x_p) + m_{22}(y_i - y_p) + m_{32}c$$
$$F_3 = Z_i = Z_C + m_{13}(x_i - x_p) + m_{23}(y_i - y_p) + m_{33}c$$

Equation 87

where:

X_i, Y_i, Z_i	are the object co-ordinates of the unknown point i
m_{ij}	correspond to those given in Equation 50

The matrix of partial differentials, F, can now be determined. The partial differentials themselves are easily calculated by any of a number of mathematical software packages (for example Mathematica) and for this reason will not be presented here.

$$F = \begin{vmatrix} \frac{\partial F_1}{\partial X_C} & \frac{\partial F_1}{\partial Y_C} & \frac{\partial F_1}{\partial Z_C} & \frac{\partial F_1}{\partial \omega} & \frac{\partial F_1}{\partial \phi} & \frac{\partial F_1}{\partial \kappa} & \frac{\partial F_1}{\partial x_p} & \frac{\partial F_1}{\partial y_p} & \frac{\partial F_1}{\partial c} & \frac{\partial F_1}{\partial x_i} & \frac{\partial F_1}{\partial y_i} \\ \frac{\partial F_2}{\partial X_C} & \frac{\partial F_2}{\partial Y_C} & \frac{\partial F_2}{\partial Z_C} & \frac{\partial F_2}{\partial \omega} & \frac{\partial F_2}{\partial \phi} & \frac{\partial F_2}{\partial \kappa} & \frac{\partial F_2}{\partial x_p} & \frac{\partial F_2}{\partial y_p} & \frac{\partial F_2}{\partial c} & \frac{\partial F_2}{\partial x_i} & \frac{\partial F_2}{\partial y_i} \\ \frac{\partial F_3}{\partial X_C} & \frac{\partial F_3}{\partial Y_C} & \frac{\partial F_3}{\partial Z_C} & \frac{\partial F_3}{\partial \omega} & \frac{\partial F_3}{\partial \phi} & \frac{\partial F_3}{\partial \kappa} & \frac{\partial F_3}{\partial x_p} & \frac{\partial F_3}{\partial y_p} & \frac{\partial F_3}{\partial c} & \frac{\partial F_3}{\partial x_i} & \frac{\partial F_3}{\partial y_i} \end{vmatrix}$$

Equation 88

Using Equation 83, the variance-covariance matrix of the unknowns (X_i, Y_i, Z_i), given in Equation 89, can be calculated.

$$\sum_F = \begin{vmatrix} \sigma^2_{X_iX_i} & \sigma_{X_iY_i} & \sigma_{X_iZ_i} \\ \sigma_{Y_iX_i} & \sigma^2_{Y_iY_i} & \sigma_{Y_iZ_i} \\ \sigma_{Z_iX_i} & \sigma_{Z_iY_i} & \sigma^2_{Z_iZ_i} \end{vmatrix}$$

Equation 89

Both the unknowns (X_i, Y_i, Z_i) and the variance-covariance matrix $(\sum_F)$ calculated in this step of the method are used as input data to the next step. The law of error propagation is applied at each step in the method and on each occasion the variance-covariance matrix produced in the previous step is used as input to the new

calculations. This ensures that the standard deviations of the interior and exterior orientation parameters affects the standard deviations of the unknowns at each step of the method. Finally, the standard deviations of the ordinates of the three points calculated on the axis of the cylinder are determined.

Table 11 on the following page shows which observations are required as input into each step as well as how the input variance-covariance matrix is formed. It shows a reference to the equations which are required at each step, as well as which variables the resultant variance-covariance matrix of the step is composed with respect to.

What the step in the method calculates	**The observations required for the step**	**How the input variance-covariance matrix is formed**	**Functions used by the step**	**The elements of the resultant variance-covariance matrix are formed with respect to these variables**
Single object point	Image co-ordinates of the desired point and the interior and exterior orientation of the image	The standard deviations of interior and exterior orientation produced by a bundle adjustment	Equation 87	(X,Y,Z) of the object point
Edge-plane through 3 points	The co-ordinates defining three object points	Formed by combining the var-covar matrices from two object point calculations and the standard deviation of the PC determined from a bundle adjustment	Equation 53	(A,B,C,D) of an edge-plane
Edge bisector plane from two edge-planes	The parameters defining two edge-planes	Formed by combining the var-covar matrices from two edge-plane calculations	Equation 55	(A,B,C,D) of an edge bisector plane
The co-ordinates of a point on the cylinder axis; one ordinate is held fixed, the other two are solved for	The parameters defining two edge bisectors	Formed by combining the var-covar matrices from two edge bisector calculations	Equation 76	(X,Y) (Y,Z) or (X,Z) depending on which ordinate was held fixed

Table 11 Steps in the error propagation calculations for the FEP method

As was mentioned previously, the same images that were used in Section 7.3 were used for the error analysis. These images consist of six sets of images. Each set of images shows the cylinder in a different pose within the object co-ordinate system. It was hoped that this would determine whether the pose of the cylinder had any significant effect on the ability of the method to produce an accurate result.

Although the original intention when performing the error analysis of the method was to determine its absolute accuracy, it is also desirable to study the effect that varying the angle between the two edge bisector planes defining the axis has on the accuracy of the method. Each set of images contains a number of images which were used to determine the cylinder parameters. An attempt was made to capture these images so that equal angles were formed between the edge bisector planes originating from successive pairs of camera positions. Furthermore, an attempt was made to ensure that the angle formed between the bisector planes originating from the first and last camera positions approached 90°. Whilst it was not in fact possible to ensure that these conditions were met perfectly, the range of angles between the edge bisector planes originating from the images in each set is sufficient to draw conclusions.

For each image in a set, the parameters of the two silhouette edge lines on the image were determined. The image co-ordinates of two points on each line were then calculated. These provided the image co-ordinate input data required by the error propagation technique described earlier.

In theory, the standard deviations of the interior and exterior orientation parameters specific to each image, as determined from the results of a bundle adjustment, ought to be used as input into the error propagation technique. This would give a true reflection of the error of the final output associated with those specific images. However, as is expected, the standard deviations of the interior and exterior orientation parameters of the various images used to determine an axis position, vary from image to image. If the error propagation technique is used with these varying standard deviations, it is difficult to interpret the final results. In other words, it is

difficult to distinguish the influence that altering the intersection angles between the edge bisector planes had on the final result, from the influence that variations in the input standard deviations had on the final result. Furthermore, using standard deviations specific to individual images offers no advantage when attempting to make a *general* statement about the overall accuracy of the method.

As a result, a decision was taken to use the same interior and exterior orientation standard deviation values as input into the error propagation calculations for all the images. These values were representative of the standard deviation values associated with all 54 images captured of the cylinder for the preceding tests. Each representative standard deviation value was calculated as the approximate mean of that value determined for each of the images used. The representative values are given in Table 12.

PC	**orientation angles**	**interior orientation**
$\sigma_{X_c} = 0.15mm$	$\sigma_{\omega} = 0.017°$	$\sigma_{x_p} = 0.0045mm$
$\sigma_{Y_c} = 0.15mm$	$\sigma_{\phi} = 0.017°$	$\sigma_{y_p} = 0.0045mm$
$\sigma_{Z_c} = 0.25mm$	$\sigma_{\kappa} = 0.017°$	$\sigma_{c} = 0.0025mm$

Table 12 The representative values of the PC, orientation angles and the interior orientation parameters which were used as input into the error propagation calculations.

Table 13 shows standard deviations of the ordinates of object points calculated on the cylinder axis. Three object points are calculated using the parameters defining each axis by holding, in turn, the X, Y and Z ordinates fixed. The results from six sets of images are shown, each set capturing the cylinder in a different pose. A graphical representation of the orientation of the cylinder for each pose is shown in Figure 56-Figure 61.

Within each set, the parameters of the axis and the error analysis associated with them, was calculated for a number of combinations of images. The results are

displayed in Table 13 and are ordered within each set by the magnitude of the intersection angle between the two edge bisector planes defining the axis. The values shown in **bold** are the result of the calculation with the lowest standard deviations within each set.

Set	Intersection angle (degrees)	X fixed		Y fixed		Z fixed	
		σ_Y (mm)	σ_Z (mm)	σ_X (mm)	σ_Z (mm)	σ_X (mm)	σ_Y (mm)
1	16	21	21	616	44	548	39
	18	8	22	249	30	606	28
	21	13	14	384	28	409	26
	30	5	16	175	21	415	18
	37	4	11	125	13	289	11
	40	6	8	189	14	242	13
	46	5	7	167	13	202	11
	56	5	7	165	12	188	10
	58	**4**	**6**	136	9	169	8
2	25	36	29	76	22	301	112
	38	9	26	20	25	268	125
	63	**9**	**14**	20	13	146	68
3	42	32	28	10	25	55	161
	44	30	22	9	23	44	150
	86	49	17	**15**	**16**	33	101
4	14	51	54	27266	15664	94	51
	36	9	31	1669	959	53	9
	51	**9**	**17**	1672	959	30	9
5	25	34	30	28	48	39	75
	34	12	30	10	29	40	45
	60	14	20	**11**	**19**	26	30
6	30	293	226	16	51	14	57
	49	244	232	13	37	14	42
	79	277	241	**15**	**25**	14	28

Table 13 Summary of the standard deviations obtained using the FEP method: Test B

Although additional tests are not shown here, the data in the table above is representative of data obtained from repeated similar tests. Table 15 in Appendix 11.3 shows data from another similar test.

It is immediately apparent that the standard deviations in Table 13 appear greater than expected. These results appear to conflict with the results of the tests in the previous chapter which indicated that the position of the axis calculated using the silhouette-edge methods compared favourably with other methods used to determine its position. However, on closer investigation, a number of factors appear to account for the magnitude of these standard deviations, namely:

(a) The choice of which ordinate was held fixed when determining the point on the axis.

(b) The magnitude of the standard deviations of the interior and exterior orientation parameters.

(c) The selection of the two original image co-ordinates.

(d) The lack of redundancy in the method.

These factors are further discussed below.

(a) The effect on the results of the choice of ordinate held fixed when calculating the points on the axis for a particular pose, can be seen in Table 13. Clearly, the discrepancy between the standard deviations obtained when holding X, Y or Z fixed are directly related to the orientation of the cylinder in the co-ordinate system. It is obvious that, for example, a small variation in the fixed X ordinate when determining a point on a cylinder axis which is horizontal and has little alteration in depth away from the camera, will result in negligible variations in the Y or Z ordinates of the point being calculated. On the other hand, a small variation in the fixed Y or Z ordinates when determining a point on the same axis, will result in a large variation in the X ordinate of the point being calculated. The effect this

has on the standard deviations calculated when holding X, Y and Z fixed respectively, can be clearly seen in set 1 in Table 13.

Table 13 also show that as the orientation of the cylinder is shifted in the co-ordinate system towards being at 45° to each axis, the disparity between the standard deviations obtained from holding each ordinate fixed decreases. This is demonstrated in the results of set 5 in this table.

(b) An obvious factor which has an effect on the final standard deviations is the magnitude of the initial standard deviations which are input into the error analysis. Needless to say, if the images can be oriented with greater certainty and therefore lower representative standard deviation values input into the calculations, the standard deviations of the final output will be decreased.

(c) A factor not immediately apparent is that the position on the image of the two initial image co-ordinates selected affects the final standard deviations. It should be recalled that these two image points are determined from the parameters of the edge line on the image. Their co-ordinates in object space are later determined and together with the co-ordinates of the PC, are used to determine the parameters of a silhouette edge-plane in object space.

The geometry of the three points in object space used to determine the plane directly affects the standard deviation of the parameters of the plane. As the distances between the three points increase, the standard deviations of the plane's parameters decrease dramatically. This can be achieved by selecting the required edge line points on the image plane outside the physical dimensions of the image.

These image points were only calculated outside the physical dimensions of the image for the purpose of the error analysis calculations. However, it should be emphasised that whereas increasing the distances between the two resulting points

in object space and the PC affects standard deviations within the error analysis, it has *absolutely no* effect on the eventual parameters of the planes which define the cylinder axis, only on their standard deviations.

There is a further factor which needs to be taken into consideration. As the two image points on the edge line are moved further apart, the geometry of the three points in object space (the co-ordinates in object space of the two image points and the camera PC) through which the edge-plane is fitted, improves. At the same time however, the standard deviation of the image points co-ordinates in object space increases. This increase occurs because the calculation of the object space co-ordinates of the two points is affected by the standard deviations of the interior and exterior orientation of the image. As a result, when the two image points are a certain distance apart, the beneficial affect on the standard deviations of the final error analysis results, caused by improving the geometry between the three object points, is offset by the affect of the increasing standard deviations of the object co-ordinates of the points used. At this stage the standard deviations of the plane's parameters begins to increase the further apart the three points are positioned.

It was initially assumed that an ideal distance between the two image points existed and that finding this would remove one of the sources of difference between different error analysis calculations. However, despite repeated testing the author was unable to verify this. Instead, it was found that it was necessary to heuristically determine for each image individually a best approximate relative position between these two points and the PC. It is unlikely however, that the exact ideal distance was determined for each image and therefore that some of the differences between results, as well as the magnitude of the results themselves, can be attributed to this factor.

(d) Another factor affecting the magnitude of the resultant standard deviations is the lack of any redundant observations in the calculations. Photogrammetric calculations typically achieve low standard deviations through the use of

redundant observations (assuming that the observations are uniform and do not contain gross errors).

The use of a greater number of images than the minimum required to define the axis of a cylinder results in the formation of redundant edge bisector planes. If a best-fit axis line defined by the intersection of these planes was calculated, as suggested in Section 5.4.4, it would be expected that the standard deviations of the parameters defining the axis would decrease relative to the results presented in Table 13.

For the four reasons given above, it is difficult to draw any conclusions regarding the absolute accuracy of the method beyond those already presented in the previous chapter. Furthermore, for the reasons given under (a), it is difficult to make any comparisons between different poses of the cylinder. Although certain poses do have better standard deviations than others, it appears that this is as much a function of the statistical method used to determine the standard deviations as anything else.

However, the standard deviations calculated can be used to evaluated the effect of the size of the intersection angle between the two defining edge bisector planes. The standard deviations clearly decrease as the intersection angle increases. The standard deviations decrease rapidly as the angle tends towards 30°. Between 30° and 45° the rate of at which the standard deviations decrease appears to become more gradual. Although the standard deviations are smallest at the largest angles in each set, the difference in comparison with standard deviations at angles around 45° is generally not substantial. A study of the error analysis results leads to the conclusion that, at least with respect to the calculation of standard deviations, attempts should be made to ensure that the intersection angle between the edge bisector planes from the two images is greater than 30° and preferably 45° or greater.

It can be concluded from the error analysis results that provided edge lines of similar length are visible on the images and that a sufficiently large angle exists between the edge bisectors defining the cylinder axis, the orientation of the cylinder with respect to either the co-ordinate system or the camera has little effect on the final results. However, in practice it is difficult to ensure a reasonable intersection angle between the defining planes for certain orientations of the cylinder. This in turn can cause certain orientations to lead to results with lower confidence levels.

9 CONCLUSIONS AND RECOMMENDATIONS

The objective of this thesis was to develop a digital photogrammetric pipe measurement technique which could supplement those digital photogrammetric methods currently being used. This objective has been achieved.

It was pointed out in the thesis that photogrammetric methods currently used to determine cylinder parameters rely on point-based photogrammetry. Point-based photogrammetry has limitations, some of which line-based photogrammetry can overcome. The new method for determining the parameters of pipes presented in this thesis is based on line photogrammetry and utilises the silhouette edges of a cylinder which are visible in an image. Three sub-methods of the technique were investigated; the four-edge-planes method, the three-edge-planes method and the three-separate-edge-planes method. The basis of a technique which uses multiple silhouette edges from multiple images was also presented.

Tests were carried out to determine the accuracy and consistency of the three sub-methods using objects representing small and medium bore pipes. The effect of the camera positions with respect to one another as well as the cylinder was investigated, as was the effect of the pose of the cylinder with respect to the camera and object co-ordinate systems.

It was found that consistently accurate results could only be expected if the camera positions, together with the position and orientation of the cylinder, resulted in an angle of greater than 15° between the two edge bisector planes which define the cylinder's position and orientation. The pose of the cylinder was found to have no significant effect on the results.

The four-edge-planes (FEP) and three-edge-planes (TEP) methods were found to be capable of consistently defining the pipe's axis to within 2-3mm of the likely "true" axis parameters, and its direction to within 0.1°. These accuracies were similar to those with which the position and orientation of the cylinders used in the test could be measured using different point-based digital photogrammetric techniques, as well as standard survey techniques. The radii calculated by these two methods in all of the tests were to within 1mm of the "true" value and often significantly better.

The three-separate-edge-planes (TSEP) method produced less accurate and less consistent results. It was explained that three edge-planes of a cylinder would form one of two "patterns". Combinations of edge-planes, called in this thesis "pattern A", produced results which were almost always less accurate that those of the "pattern B". Results from "pattern A" combinations differed often as much as 2-5cm (and at times even more) from the "true" positional values of the cylinder axis. "Pattern B" combinations however, produced results which were typically 1-4mm and less than 0.3° from the "true" positional values of the axis. In fact "pattern B" combinations usually produced similar results to the FEP and TEP methods. However, there was less consistency in the results obtained using this method than when using the two other silhouette-edge methods.

An error analysis of the FEP method was performed. For the reasons presented in Chapter 9, it was found to be difficult to interpret the individual standard deviations produced by the error analysis of the FEP method. However, it was shown that the standard deviations of the results of the FEP method improved as the angle between the two edge bisector planes defining the cylinder's position and orientation increased.

It proved difficult to accurately establish the true positional parameters of the cylinder's axis in order to make a comparison with those parameters determined using the silhouette-edge methods. Furthermore, although the absolute accuracy of pipes in a plant layout is important, their relative position is perhaps of greater importance. For

these reasons, a test was carried out to investigate the consistency with which the positions of two cylinders with respect to one another could be determined. This test showed that the shortest distance between the two cylinders could be measured to a level of consistency of approximately 1mm. This is quite sufficient to determine whether two pipes intersected in reality.

The various tests showed that the way in which the cylinder was illuminated had an important influence on the accuracy of the final results. The silhouette-edge methods assume that the edge-planes created from the images used to determine the parameters of a cylinder are truly tangential to the cylinder. This can only be achieved if the silhouette edge lines extracted from the images represent true silhouette edges of the cylinder. This in turn is reliant on the edge detector and line following methods' ability to correctly and accurately identify and link edge pixels in the images which represent the true silhouette edges of the cylinder. For this reason, it is important that the silhouette edges are well defined visibly in the images. Particular attention must be given to ensure that the silhouette edges of a cylinder do not fall into shadow areas which might make the edges indistinct to edge detectors. It seems likely that in many of the tests this factor accounts for the 1-2mm deviation of the calculated cylinder values from the true values.

In general, the FEP method produced the most accurate and consistent results in the tests and the TSEP method the least accurate and least consistent. The tests led to the conclusion that none of the silhouette-edge methods were suitable, in their current form, for measurements requiring sub-millimetre accuracy. However, the methods are suitably accurate for situations where accuracies of only a few millimetres are acceptable. The accuracy of the silhouette-edge methods meets the requirements for measuring pipes in industrial plants. Photogrammetric applications which are required to determine the parameters of a cylinder to accuracies greater than the three methods can achieve, may benefit from the method proposed in this thesis which utilises multiple silhouette edges from multiple images. However, any improvement in accuracy will be at the expense of greater computational complexity.

A secondary objective of this thesis was to present a basis for future local programming efforts towards producing a digital photogrammetric pipe measurement module which could be integrated with companies PDSs. The use of PDSs by industry has shown that digital storage of data in a three dimensional form is currently the most efficient method for managing an industrial plant's pipe network. Due to its digital nature, digital photogrammetry is perhaps the most efficient method by which the capture and measurement of data can be linked to a PDS. Digital photogrammetry complements PDSs by providing the user with a similar high level of automation and the same convenient digital storage medium as a PDS. Ideally, the digital photogrammetric pipe measurement module should be built into the PDS as an extension to the PDS's existing capabilities. This would give the module access to all the knowledge in the PDS data base. Information such as the standard radii of pipes in a specific plant and the expected layout of the pipe network would be available to the measurement module. The PDS would also be capable of manipulating the position and orientation of pipes measured by the module to ensure realistic positions of the measured pipes within the existing network.

Such a tight integration of digital photogrammetric software with a PDS requires considerable understanding of the PDS as well as good programming skills in general. These skills are most likely to be possessed by individuals with a computer science programming background, rather than those with only a digital photogrammetric background. With this in mind, the basis of the digital photogrammetry knowledge which might be required, as well as the pipe measurement techniques themselves, have been presented in this thesis. A section has also been included in the Appendix which describes the author's approach to some of the programming aspects of the thesis. It is hoped that should a computer programmer wish to write a digital photogrammetric measurement module, the information contained in this thesis will be of assistance.

This thesis presented a digital photogrammetric measurement technique based on linear features visible in images, which is equally or more efficient and accurate than alternative point based techniques. It is the author's opinion that the current research

trend of developing measurement techniques which utilise known geometric attributes of the objects being measured, will result in more efficient and accurate techniques.

10 BIBLIOGRAPHY AND REFERENCES

Adamos, C., & Faig, W., 1992. **Hough Transform in Digital Photogrammetry**, ISPRS Commission III, Washington, pp 250-254.

Abdel-Aziz, Y. I., & Karara, H. M., 1971. **Direct Linear Transformation from Comparator Co-ordinates into Object Space Co-ordinates in Close Range Photogrammetry**, Proceedings of ASP/UI Symposium on Close Range Photogrammetry, Urbana, Illinois, USA, pp 1-8.

Baker, H., 1984. **Surface from Mono and Stereo Images**, Photogrammetria, Vol. 39, pp 217-237.

Ballard, D. H., 1981. **Generalising the Hough Transform to Detect Arbitrary Shapes**, Pattern Recognition, Vol. 13, pp 111-122.

Beliveau, Y. J., Jayaram, S., & Johnson, S. D., 1990. **Reversed Engineering of a Product Model**, SPIE Close Range Photogrammetry meets Machine Vision, Vol. 1395, pp 894-899.

Beyer, H. A., 1991. **Automated Dimensional Inspection of Cars in Crash Tests with Digital Photogrammetry**, SPIE, Industrial Vision Metrology, Vol. 1526.

Beyer, H. A., 1992. **Geometric and Radiometric Analysis of a CCD-Camera Based Photogrammetric Close-Range System**, Dissertation No. 9701, ETH-Zurich.

Beyer, H. A., 1994. **IMETRICS TP200 - A System for High Accuracy 3D Image Metrology**, Paper presented at the Symposium on Optics for Productivity in Manufacturing, Frankfurt, 20 - 24 June 1994.

Beyer, H. A., Streilein, A., 1991. **Data Generation for CAAD with Digital Photogrammetry**, Proceedings of International Conference for Computer Aided Architecture Design, CAAD futures, Zurich, 1 – 3 July 1987.

Brown, D. C., 1958. **A Solution to the General Problem of Multiple Station Analytical Stereotriangulation**, RCA Data Reduction Technical Report No. 43, Patrick Air Force Base, Florida, USA.

Bruhn, H., & Schneider, C. T., 1990. **Optical Measurement of Vehicle Body-Shapes in the Wind Tunnel**, SPIE Vol. 1395, Close Range Photogrammetry meets Machine Vision, pp 900-907.

Calitz, M. F.,1995. **Image Understanding and Feature Extraction for Applications in Industry and Mapping**, Ph.D. Dissertation, University of Cape Town.

Cammidge, M., 1996. **The Design of a Digital Photogrammetric Metrology System for the Semi-Automatic Surveying and Recording of Pipe Dimensions in Industrial Plants**, M.Sc. Dissertation, University of Cape Town.

Canny, J., 1986. **A Computational Approach to Edge Detection, Transactions on Pattern Analysis and Machine Intelligence**, IEEE Transactions on Pattern Analysis and Machine Intelligence, Vol. PAMI-8, No. 6, pp 679-698.

Chandler, J. H., Cooper, M. A. R., 1991. **Determining Cylindrical Parameters – an Alternative Approach**, CS Monthly, Land and Hydrographic Survey, 5-7 September.

Chapman, D., Deacon, A., & Hamid, A., 1992. **CAD Modelling of Radioactive Plant: The Role of Digital Photogrammetry in Hazardous Nuclear Environments**, International Archives of Photogrammetry and Remote Sensing, Part B5 XXIX, pp 741-753.

Deren, I. L., & Guoqing, Z., 1994. **CAD-Based Line Photogrammetry for Automatic Measurement and Reconstruction of Industrial Objects**, ISPRS Commission V, pp 231-240.

Dermanis, A., 1994. **Free Network Solutions with the DLT Method**, ISPRS Journal of Remote Sensing, Vol. 49, No. 2, pp 2-12.

Förstner, W., & Gülch, E., 1987. **A Fast Operator for Detection and Precise Location of Distinct Points, Corners and Centres of Circular Features**, Proceedings of the Inter-commission Conference on Fast Processing of Photogrammetric Data, Interlaken, Switzerland, 2 - 4 June 1987, pp 281-305.

Fraser, C. S., 1995. **Deformation Measurement of a Large Coal Dredger by Digital Photogrammetry**, International FIG Symposium Proceedings, Commission 6, Cape Town, pp 67-75.

Fraser, C. S., & Shortis, M. R., 1994. **Vision Metrology in Industrial Inspection: a Practical Evaluation**, International Archives of Photogrammetry and Remote Sensing, Vol. 30, No. 5, pp 87-91.

Fraser, C. S., & Shortis, M. R., 1995. **Metric Exploitation of Still Video Imagery**, Photogrammetric Record, Vol. 15, No. 85, pp 107-122.

Fraser, C. S., 1997. **Innovations in Automation for Vision Metrology Systems**, Photogrammetric Record, Vol. 15, No. 90, pp 901-911.

Gruen, A. W., & Baltsavias, E. P.. 1988. **Geometrically Constrained Multi-Photo Matching**, Photogrammetric Engineering and Remote Sensing, Vol. 54, No. 5, pp 633-641.

Gruen, A. W., & Hailong L., 1994. **Semi-Automatic Road Extraction by Dynamic Programming**, ISPRS Commission III, Working Group 2, pp 324-332.

Gruen, A. W., 1985. **Adaptive Least Squares Matching - A Powerful Image Matching Technique**, Paper presented to the ACSM-ASP Convention, Washington DC, March 1985.

Hâdem, I., 1990. **Estimating Approximate Values Before Bundle Adjustment in Close-Range Photogrammetry – A Review**, SPIE Vol. 1395 Close-Range Photogrammetry Meets Machine Vision, pp 1016-1027.

Hamit, F., 1995. **As-Built Industrial Visualisation CAD meets Digital Photo and Document**, Advanced Imaging, November 1995, pp 75-77.

Haralick, R. & Shapiro, L., 1992. **Computer and Robot Vision**, Vol. 1-2, Addison Wesley.

Heipke, C., Englisch A., Speer, T., Stier, S., & Kutka, R., 1994. **Semi-Automatic Extraction of Roads from Aerial Images**, ISPRS Commission III, Working Group III/2, Vol. 30, pp 353-360.

Hill, J., Rüther, H., & Mason, S., 1997. **Line Photogrammetry for 3D Object Reconstruction**, Proceedings of iKusasa, CONSAS 97, Durban.

Hoffa, P. G. J., 1996. **The Mensuration of Textured Surfaces using Close-Range Digital Photogrammetry for Applications in Industry**, M.Sc. Dissertation, University of Cape Town.

Karara, H. M., 1989. **Non-Topographic Photogrammetry**, American Society for Photogrammetry and Remote Sensing.

Kindle, J. H., 1950. **Theory and Problems of Plane and Solid Analytical Geometry**, Schaum Publishing Co., New York.

Krämer, J., & Schöler, H., 1980. **Photogrammetric Measurement of Piping Systems**, Presented Paper, 14th International Congress of ISP, Commission V, Working Group, Hamburg, 1980.

Littleworth, R. M., Stirling, D. M., & Chandler, J. H., 1992. **Three-Dimensional Mapping and As-built Computer Modelling by Analytical Photogrammetry**, International Archives of Photogrammetry and Remote Sensing, Part B5 XXIX, pp 754-760.

Littleworth, R. M., & Chandler, J. H., 1995. **Three Dimensional Computer Graphic Models by Analytical Photogrammetry**, Photogrammetric Record, Vol. 85, No. 15, pp 65-76.

Lloyd, G., 1995. **Industrial Survey Techniques For The Development Of Computer Models**, International FIG Symposium Proceedings, Commission 6, Cape Town, pp 174-184.

Matthews, M., 1994. **A Machine Vision Based Non-Contact Measuring Tool for Mensuration in Industry and Manufacturing**, M.Sc. Dissertation, University of Cape Town.

McGlone, J. C., 1989. **Analytical Data-Reduction Schemes in Non-Topographic Photogrammetry**, in **Non-Topographic Photogrammetry**, Karara, H. M. (Ed.), Second Edition, American Society for Photogrammetry and Remote Sensing, pp 37-57.

MCP, 1986. **Micro Computer-Aided Photogrammetry System**, ICI Photometrology operational manual.

Mikhail, E. 1993. **Linear Features for Photogrammetric Restitution and Object Completion**, SPIE Vol. 1944, pp 16-24.

Mulawa, D. C., & Mikhail, E. M., 1988. **Photogrammetric treatment of Linear Features**, ISPRS 16th Congress, Commission III, pp 383-393.

Petsa, E., & Patias, P., 1994a. **Relative Orientation of Image Triples using Straight Linear Features**, International Archives of Photogrammetry and Remote Sensing, Vol. 30, No. 3/2, pp 663-669.

Petsa, E., & Patias, P., 1994b. **Formulation and Assessment of Straight Line Based Algorithms for Digital Photogrammetry**, ISPRS Commission V, Working Group 1, pp 310-317.

Rubenstein, M., 1990. **Assessing Target Centering Algorithms for use in Near-Real-Time Photogrammetry**, M.Sc. Dissertation, University of Cape Town.

Rüther, H., 1993. **Course Notes - The Theory of Adjustment of Observations: SUR321F**, University of Cape Town.

Rüther, H., 1994. **Course Notes - Advanced Engineering Surveying: SUR409F**, University of Cape Town.

Ryan, R. A., 1982. **Close-Range Photogrammetry and Cultural Resource Management: Five Case Studies**, Technical Papers of the American Society of Photogrammetry, ASP-ACSM Convention, Denver, March 1982, pp 62-71.

Smit, J. L., 1997a. **Three Dimensional Measurement of Textured Surfaces using Digital Photogrammetric Techniques**, Ph.D. Dissertation, University of Cape Town.

Smit, J. L., Mason, S. O., Rüther, H., & Dingle, M. R., 1997b. **3D Reconstruction of an Automobile Exterior using Digital Photogrammetric Techniques**, Proceedings of iKusasa, CONSAS 97, Durban.

Szczechowski, B., 1980. **The Photogrammetric Measurements of Ship Deformations**, International Archives of Photogrammetry, Vol. 23, No. B5, Hamburg, pp 714-723.

Tabatabai, A. J., & Mitchell, O. R., 1984. **Edge Location to Sub-pixel Values in Digital Imagery**, Transactions on Pattern Analysis and Machine Intelligence, Vol. PAMI-6, No. 2, pp 188-201.

Van der Merwe, N., & Rüther, H, 1994. **Image Matching Through a Combination of Feature and Area Based Matching**, International Archives of Photogrammetry and Remote Sensing, Vol. 30, No. 5, pp 407-413.

Van der Merwe, N., 1995. **Development of an Image Matching Scheme using Feature and Area Based Matching Techniques**, Ph.D. Dissertation, University of Cape Town.

Van der Vlugt, G., & Rüther, H., 1994. **The Development of an Automated Surface Measurement System**, International Archives of Photogrammetry and Remote Sensing, Vol. 30, No. 5, pp 414-419.

Van der Vlugt, G., 1995. **Algorithms and Design Aspects of an Automated Vision Based 3-D Surface Measurement System**, Ph.D. Dissertation, University of Cape Town.

Wong, K. W., & Ho, W., 1986. **Close-Range Mapping with a Solid State Camera**, Photogrammetric Engineering and Remote Sensing, Vol. 52, No. 1, pp 67-74.

Zielinski, H., 1993. **Object Reconstruction with Digital Line Photogrammetry**, Ph.D. Dissertation, Department of Geodesy and Photogrammetry, KTH, Stockholm.

11 APPENDIX

11.1 Programming Aspects of the Thesis

This section has been included to describe some of the computer programming aspects of the thesis. It describes the software that was developed in order to carry out tests on the cylinder measurement techniques described earlier in Section 5. Specifically, this section presents the design philosophy behind the photogrammetric software library, named PHOtogrammetric OBjectS (PHOOBS), which is currently under development in the department of Geomatics at UCT. This section has two target audiences:

- present and future members of the department who may wish to use or build on the existing library
- skilled programmers who may wish to develop similar systems.

As was previously mentioned, whilst this thesis is intended to present an alternative cylinder measurement technique to the photogrammetric community, it also has a secondary objective. It is hoped that the information provided will provide sufficient background knowledge to enable a skilled computer programmer to become familiar with the concepts of photogrammetry, edge detection, line extraction and the various cylinder measurement techniques. It is hoped that with this knowledge, combined with such an individual's programming skills, a pipe measurement software module linked to a PDS may be developed which would provide similar functionality to that provided by more expensive imported solutions. While the author makes no claims of excellent programming skills, it is hoped that this section will provide a useful reference to a skilled programmer as to how a photogrammetric module of an overall package might be designed.

The photogrammetric software library (PHOOBS) as well as the cylinder measurement program that was developed using this library, were both designed to run on a Linux-x86 platform.

Linux was selected as the operating system in which to develop the program because of a number of advantages that it has over other operating systems. Linux is a Unix-like operating system and has most of the capabilities of other Unix variants as well as having a reputation for stability. Linux also has the advantage over many Unix systems in that it runs on an Intel x86 platform while still providing acceptable levels of performance compared to more expensive low to mid-range RISC processor based platforms. The comparatively low cost of personal computers as well as the fact that Linux is distributed free of cost, makes a Linux-x86 platform an ideal choice for research purposes.

All of the source code for the PHOOBS library, as well as the cylinder measurement program written using PHOOBS, was written in C++ and compiled with the GNU C++ compiler. C++ was chosen as the programming language primarily because of its object oriented approach.

The language provides a way to communicate interface specifications between various programmers working on a project and to enforce the correctness of those interfaces at compile time. Each class defined in the library contains its own data and interface methods of manipulating that data. In most instances the only way that a user (i.e. a programmer using the library) can access and manipulate that data is through the interface (i.e. the functions) which the creator of the class makes accessible to the user.

This seemingly restrictive approach is in fact one of the great advantages of the language. The creator of the class can be secure in the knowledge that only data that he expects to be altered, can be manipulated by the user. The user can be assured that input data, manipulated by the functions provided by the creator, will produce the expected output without the user needing to concern himself with *how* the output is calculated. Whilst a similar effect could be achieved using C or other programming languages, C++ lays down a structured framework which more easily ensures that this

approach is followed. As a result, a library based on C++ can easily be used by programmers other than those who created the library. When a user creates an object from a predefined class in the library, the user merely needs to know which interface functions are used to input data into the object and which are used to retrieve or manipulate data.

It may later become necessary to alter the techniques used to produce the output from the class, for instance to replace a slow algorithm with one which is faster. This can be done by simply rewriting the existing functions within the class to use the new technique, without altering the interface of the class presented to the user. The end user need never know that the technique by which the output data is calculated has changed, since the interface to the class has remained unaltered. This makes it easy to alter and improve the techniques used in the library without users being required to make changes to existing programs built using the library.

Another advantageous feature of C++ is inheritance. Inheritance is the means by which a class can be created which inherits the characteristics (both data and functionality) of another class and at the same time adds new data and functionality of its own to create a new more powerful class. Inheritance is of great use in building a library since it allows each class to perform only a few specialised functions. This makes testing, debugging and upgrading the code simpler. More powerful classes can then be created simply by creating a class which inherits from a number of simpler classes.

An additional feature of C++ is its ability to allow encapsulation. Classes are simply another form of data type, similar to simple integers or floating point variables. The ability to encapsulate data simply means that a class may have amongst other data types, variables which are themselves classes. This provides another method by which classes created in a library may be reused.

The graphical interface to the cylinder measurement program was written using the Qt graphical user interface (GUI) library. Qt is a GUI toolkit which allows the programmer to build an interface to his program using a variety of pre-built graphical objects. Qt runs on top of X windows which is the standard graphical server for Unix-based operating systems including Linux. Furthermore, Qt, while free of cost (under specific conditions of use) for the Linux operating system it is also available commercially for Microsoft Windows NT and Windows 95.

The primary intention in developing PHOOBS was to provide a programming library which would simplify future programming efforts for research purposes (such as the program written to test the techniques developed in this thesis). As such, the Linux-x86 platform was considered the primary platform. However, the fact that both Qt and GNU C++ are available on a range of platforms (both x86 and RISC processor based as well as Microsoft and Unix operating system based) gives the PHOOBS library the potential to be easily ported to other platforms.

The PHOOBS library was initiated in the department by P. Waker as part of a M.Sc. project. Whilst the library was developed in consultation with the author, most of the code which provides the basic functionality of the library was designed by P. Waker. The authors contribution to the library was in designing and implementing higher level functionality including edge detection and line extraction classes as well as code necessary to test the cylinder measurement technique. Although an overview of the PHOOBS library will be given below, it is of a conceptual nature and classes are not mentioned specifically. It is suggested that the reader refer to the documentation written by P. Waker for an understanding of the specific layout of the PHOOBS class structure. If the library is to be used for further programming then the reader should refer to the documentation provided with the library by P. Waker and the author.

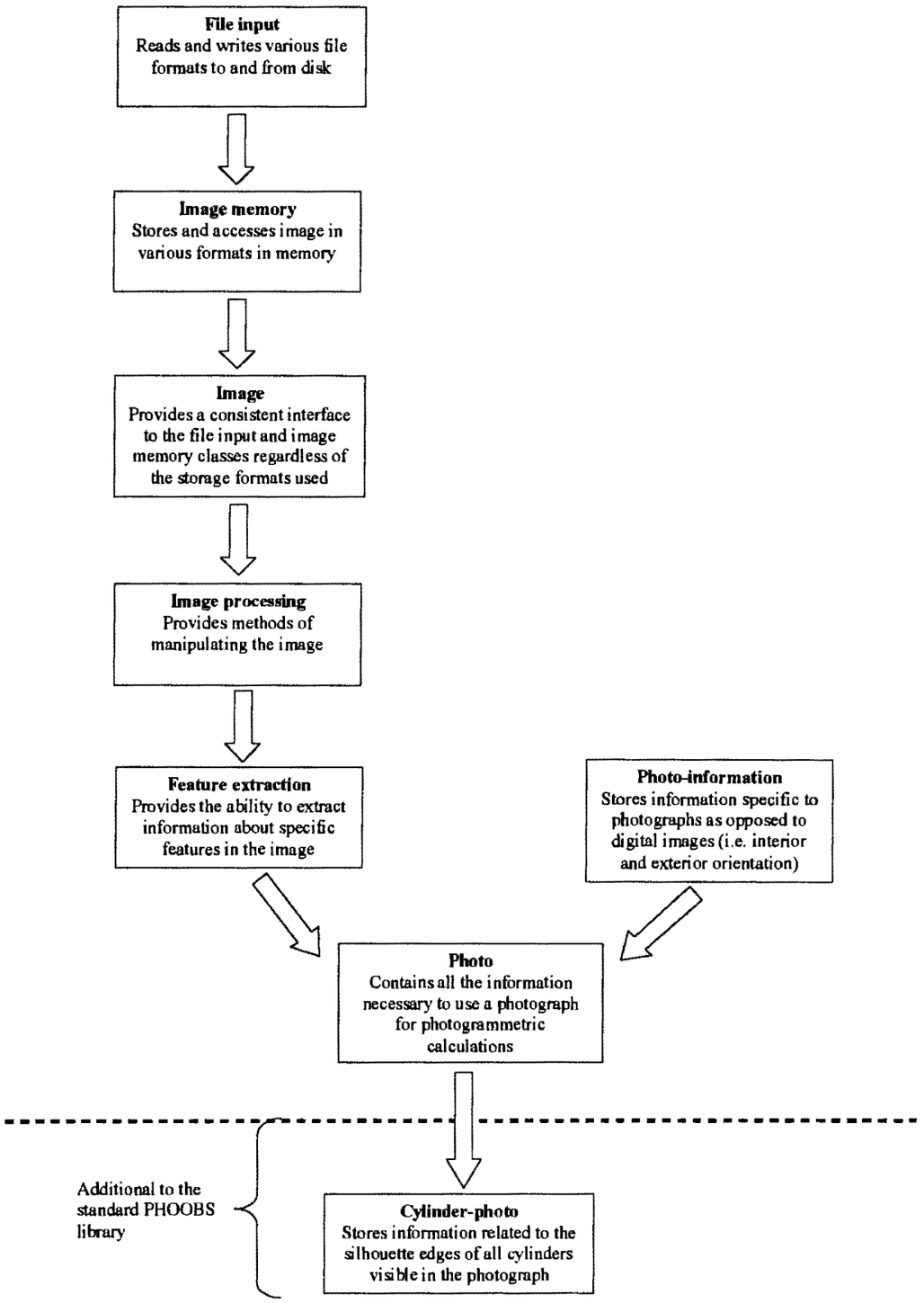

Figure 79 The conceptual layout of the class hierarchy of PHOOBS. In some cases a conceptual class may in reality consist of a number of classes.

Figure 79 shows a conceptual layout of the class hierarchy of PHOOBS. The *file input* class reads images stored in various formats from a file on a disk. The *file memory* class stores the image in memory in one of a number of formats. Both these two classes contain numerous data detailing features specific to the particular type of image being worked with; for instance, the number of tiles in a tiled TIF image, the number of levels in an image pyramid or the colour depth and image dimensions of a flat image. These are all stored in classes specific to the image type. The *image* class inherits from both the *file input* and *file memory* classes. However, no matter what format the image was stored in on disk, nor how it is stored in memory, the interface presented to the user by the *image* class is the same. The two inherited classes take care of the details of implementing requests for data for the various file formats. The user uses the same functions provided by the image class to load and save an image, regardless of the memory or disk storage format. Similarly, the user may request the colour value of a particular pixel in the image. Although, unlike in the case of a flat image, it may be necessary to perform certain functions on tiled or pyramid images before this value can be obtained, this is taken care of transparently by the *file input* and *file memory* classes. The function called by the user in the *image* class remains the same.

An object created from the *image* class provides the basic information about an image to the user as well as providing input-output capabilities. A further class is created which inherits from the image class. This class retains all the characteristics of the *image* class and adds functionality. The *image processing* class provides the functions and data storage necessary to perform image processing on the image. The image processing capabilities include edge detection and various colour map algorithms such as histogram stretching. A further class, a *feature extraction* class, inherits from the *image processing* class. This class uses the capabilities of the *image processing* class to allow it to extract features from an image. It is within this class that the line extraction techniques mentioned in Section 6.2 are implemented. This class also includes various data specifically created by the feature extraction process.

Photographs are seen in the context of the PHOOBS class hierarchy as images which have additional properties associated with them, such as camera rotations and PC object co-ordinates. Photogrammetric information relating to photographs is stored and manipulated in the *photo-information* classes. These contain information such as the interior and exterior orientation of a photograph. The *photo* class is created through inheritance from the *photo-information* and *image* classes. It has the properties of a standard digital image, as well as the properties specific to a photograph required for photogrammetric calculations.

The class in the PHOOBS library hierarchy which is ultimately derived from all other classes, is the *photo* class. An object created from this class may be used for further photogrammetric calculations. Any classes derived from the *photo* class are likely to be specific to the requirements of a particular user. The *photo* class forms the basis of the classes which were created for the program written to test the cylinder measurement technique described in this thesis. A new class, the *cylinder-photo* class, was created through inheritance from the *photo* class. This new class has access via the *feature extraction* class to the parameters of the lines defining the silhouette edges of all the cylinders visible in the photograph. Every photograph, from every camera station, was represented by its own *cylinder-photo* object.

A separate class hierarchy, shown in Figure 80, was designed to represent a network of cylinders in object space. Functions within the most derived class of this hierarchy calculate the parameters of a requested cylinder. These functions take *cylinder-photo* objects as their parameters. This gives the functions access to the parameters of the silhouette lines in all the photographs which are needed to determine the parameters of the cylinder of interest.

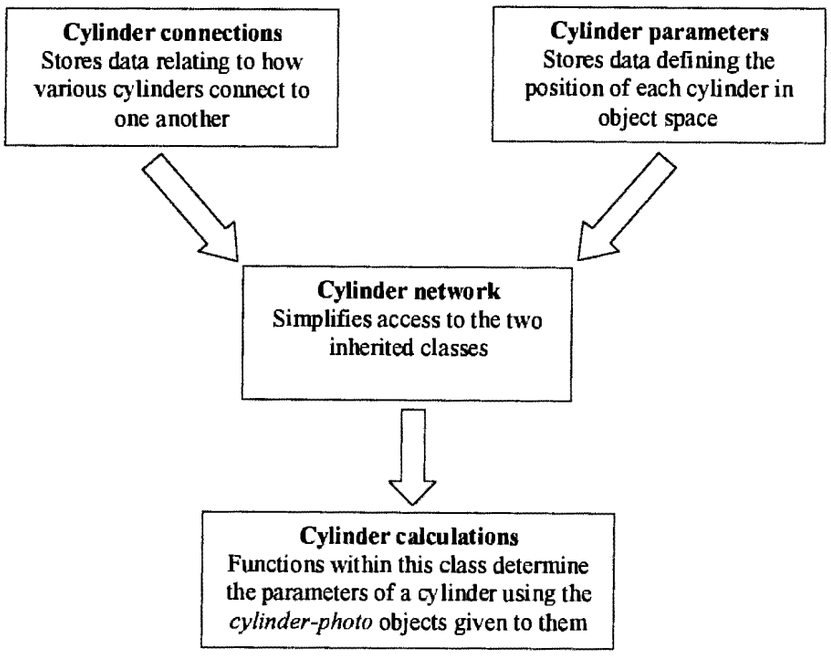

Figure 80 The conceptual layout of the class structure used to determine the parameters of a cylinder in object space

The author believes that it is possible, using a concept similar to that laid out in this section, to develop a robust system capable of being used in industry. While it was beyond the scope of this thesis to develop such a system, the author hopes that someone with suitable programming skills will be able to make use of the work described here to produce such a system.

11.2 Evaluation Sequences for the Search Masks 0° to 345° at 15° Intervals

Table 14 shows the evaluation sequence and positions for each search mask between 0° and 345°, at 15° intervals, used by the manual line following method explained in Section 6.2.2. Edge detection is performed on the image before line following occurs. The quantized search direction of the desired line is determined *a priori* and pixels, extending from an initially indicated position, are examined in the order of the search sequence.

Initially only the first three pixels in the sequence are examined. The pixel co-ordinates of any of these pixels which are found to be edge pixels are added to a list of pixel co-ordinates which define the line being extracted. If an edge pixel is found within the first three pixels of the sequence, a new search is begun, using the same search direction and centred on the last pixel added to the list. However, if no edge pixels are found, then pixels in the positions 4-7 of the sequence are examined in order. As soon as an edge pixel is found its pixel co-ordinates are added to the list and a new search is begun, centred on this pixel. Finally, if no pixels are found in these positions either, pixels in the positions indicated by the search sequence numbers 8 and 9 are examined. Once again, as soon as an edge pixel is found its pixel co-ordinates are added to the list and a new search is begun, centred on this pixel. If no edge pixels are found in any of the positions in the search sequence, the line following process is stopped. The line following process can be restarted by indicating a new initial pixel position.

quantized search direction	Seach sequence								
	1	2	3	4	5	6	7	8	9
	x and y positions relative to the pixel of interest								
15	1,0	2,1	3,1	3,0	2,0	1,1	0,1	4,1	5,2
30	1,1	2,1	3,2	3,1	2,2	2,9	1,0	4,2	5,3
45	1,1	2,2	3,3	1,2	2,1	0,1	1,0	4,4	5,5
60	1,1	1,2	2,3	1,3	2,2	0,2	0,1	2,4	3,5
75	0,1	0,2	1,3	1,2	0,3	1,1	-1,2	1,4	1,5
90	0,1	0,2	0,3	-1,2	1,2	-1,1	1,1	0,4	0,5
105	0,1	0,2	-1,3	-1,2	0,3	-1,1	1,1	-1,4	-1,5
120	-1,1	-1,2	-2,3	-1,3	-2,2	0,2	0,1	-2,4	-3,5
135	-1,1	-2,2	-3,3	-2,1	-1,2	-1,0	0,1	-4,4	-5,5
150	-1,1	-2,1	-3,2	-3,1	-2,2	-1,0	0,1	-4,2	-5,3
165	-1,0	-2,1	-3,1	-3,0	-2,0	-1,1	0,1	-2,1	-4,2
180	-1,0	-2,0	-3,0	-2,-1	-2,1	-1,-1	-1,1	-4,0	-5,0
195	-1,0	-2,0	-3,-1	-2,-1	-3,0	-1,-1	0,-1	-4,-1	-5,-1
210	-1,-1	-2,-1	-3,-2	-3,-1	-2,-2	-2,0	-1,0	-4,-2	-5,-3
225	-1,-1	-2,-2	-3,-3	-2,-1	-1,-2	-1,0	0,-1	-4,-4	-5,-5
240	-1,-1	-1,-2	-2,-3	-2,-2	-1,-3	0,-2	0,-1	-2,-4	-3,-5
255	0,-1	-1,-2	-1,-3	0,-3	0,-2	-1,-1	-1,0	-1,-4	-1,-5
270	0,-1	0,-2	0,-3	1,-2	-1,-2	1,-1	-1,-1	0,-4	0,-5
285	0,-1	1,-2	1,-3	0,-3	0,-2	1,-1	1,0	1,-4	1,-5
300	1,-1	1,-2	2,-3	1,-3	2,-2	0,-2	0,-1	2,-4	3,-5
315	1,-1	2,-2	3,-3	1,-2	2,-1	0,-1	1,0	4,-4	5,-5
330	1,-1	2,-1	3,-2	3,-1	2,-2	2,0	1,0	4,-2	5,-3
345	1,0	2,0	3,-1	2,-1	3,0	1,-1	0,-1	4,-1	5,-1

Table 14 The sequence in which the search masks 0° to 345° are evaluated

11.3 Additional Error Analysis Tables

Table 15 shows an additional set of standard deviation results to those shown in Chapter 8. The angle and the best standard deviations within each set are highlighted. The standard deviations are given in millimetres and the angles in degrees. The approximate orientation of the cylinder with respect to the co-ordinate system is the same as the sets shown in Sections 7.2 and 7.3 (refer to Figure 56-Figure 61).

Set	Intersection angle (degrees)	X fixed		Y fixed		Z fixed	
		σ_Y (mm)	σ_Z (mm)	σ_X (mm)	σ_Z (mm)	σ_X (mm)	σ_Y (mm)
1	32	4	15	1442	17	7315	26
	40	8	9	2108	10	22649	98
	49	5	10	1685	12	7104	26
	71	6	6	1996	8	7054	25
2	37	7	12	15	16	345	503
	38	13	10	8	10	259	389
	75	9	6	6	6	164	243
3	39	61597	702	39	58	42	5517
	74	2123	19	7	10	11	1740
4	17	16	18	8947	4357	37	17
	28	7	17	3713	1814	35	7
	45	6	9	3319	1616	18	6
5	29	7	18	6	20	24	30
	42	15	12	13	19	17	30
	71	9	12	8	12	17	19
6	47	296	200	35	59	49	123
	74	42	22	5	8	6	16

Table 15 Summary of the standard deviations obtained using the four-edge-planes method: Test A